The Abdus Salam International Centre for Theoretical Physics

2267-15

Joint ITER-IAEA-ICTP Advanced Workshop on Fusion and Plasma Physics

3 - 14 October 2011

Whistlers and the Associated Velocity Space Particle Diffusion in Magnetized Plasmas

KRASNOSELSKIKH Vladimir
Universite' D'Orleans
Laboratory of Physics and Chemistry of the Earth Atmosphere and Space Environment , LPC2E
National Centre for Scientific Reearch, CNRS
3A, Avenue de la Recherche Scientifique, 45071 Orleans cedex 2
FRANCE

Statistical Characteristics of Whistler Waves in the Inner Magnetosphere and their Influence on Dynamics of the Earth's Radiation Belts

Vladimir Krasnoselskikh

with the assistance of

R. Horne, D. Shklyar, O. Agapitov, Yu. Zalizniak, H. Breuillard, Yu. Khotyaintsev, A. Volokitin, T. Dudok de Wit, and G. Rolland

ICTP Workshop on Fusion and Plasma Physics

Plan.

- Radiation Belts
- Some basics on Whistler Waves
- Motivation: problem of particle diffusion
- Cluster project and data
- Cluster data and statistical properties of whistler waves
- K-vector distribution dependence upon magnetic latitudes
- Modelling of statistical properties making use of the ray tracing
- Conclusions

Why to study magnetospheric boundaries and internal magnetosphere?

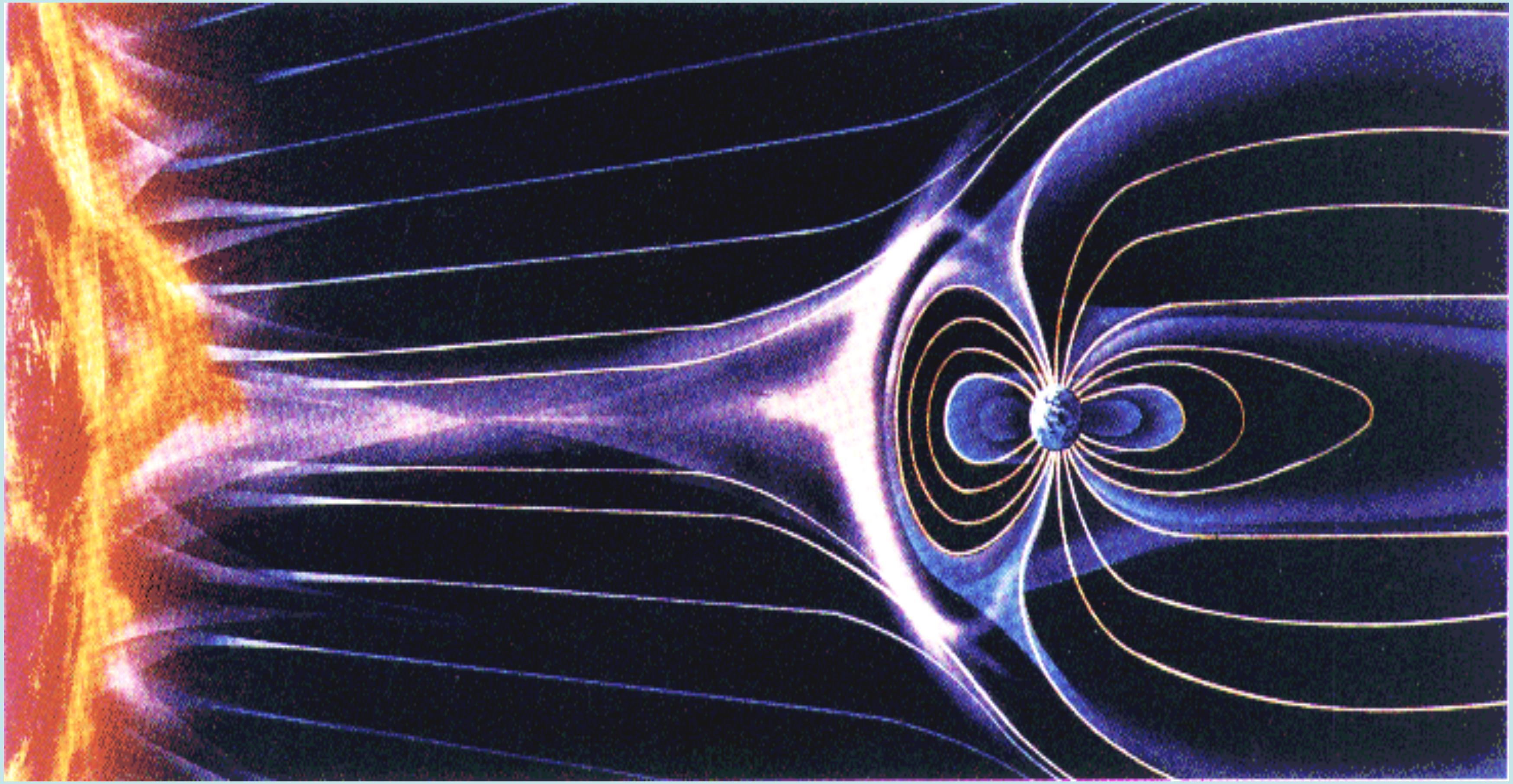

Introduction

- Solar Energetic Particles (SEPs) are accelerated at solar flares and CME (coronal mass ejection) shocks.

- At times these particles dominate the energetic particle population of the magnetosphere.

- The goal of this study is to quantitatively predict the population of the magnetosphere by these particles.

- The focus of interest is trapping in the inner magnetosphere.

From R.L. Richard et al.

November 24, 2001 SEPs

- The magnetic storm of November 24, 2001 was accompanied by a large increase in upstream Solar Energetic Particles (SEP) that were observed by ACE.
- SEP fluxes are enhanced between roughly 0430 UT and 1700 UT.
- Heightened fluxes of energetic particles were observed by geosynchronous GOES and LANL spacecraft during the period of heightened proton fluxes.

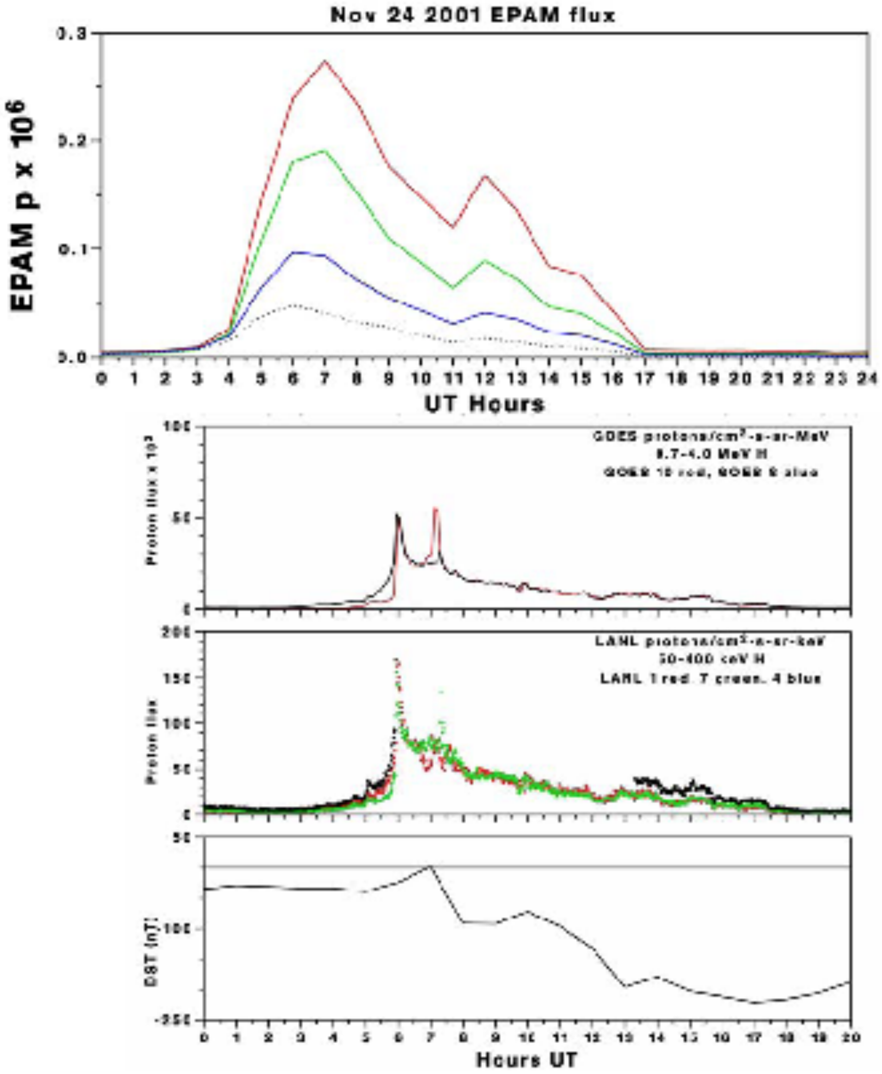

From R.L. Richard et al.

Solar Wind, IMF and DST

WIND was located near x = 18 RE, y = -80 RE, z = 7 RE at 0500 UT; ACE was near x = 242 RE.
After 0700 UT DST began to decline, reaching about -200 nT.

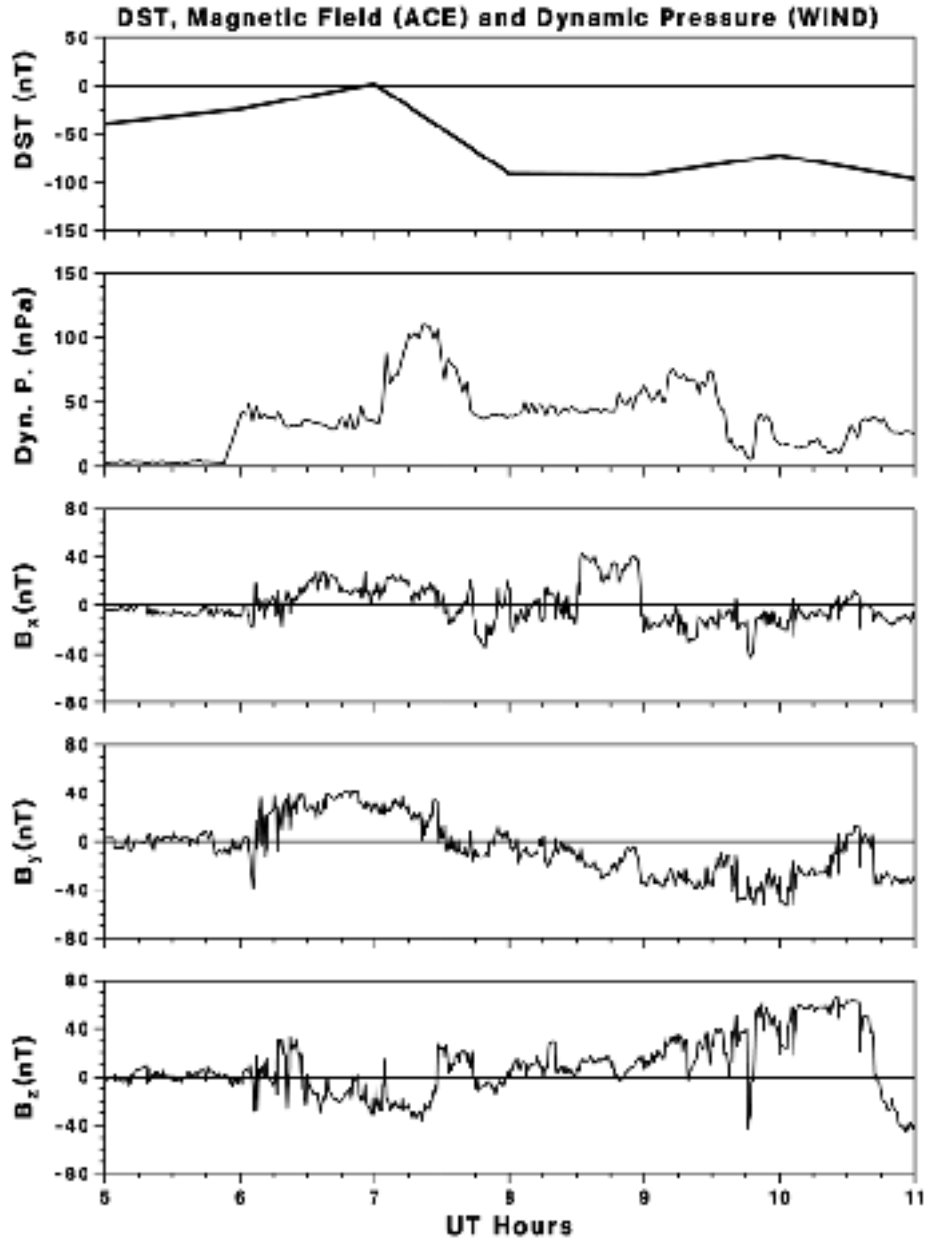

From R.L. Richard et al.

An SEP proton's trajectory is calculated in MHD electric and magnetic fields.
The plane shows the plasma beta in the (GSE) equatorial plane.

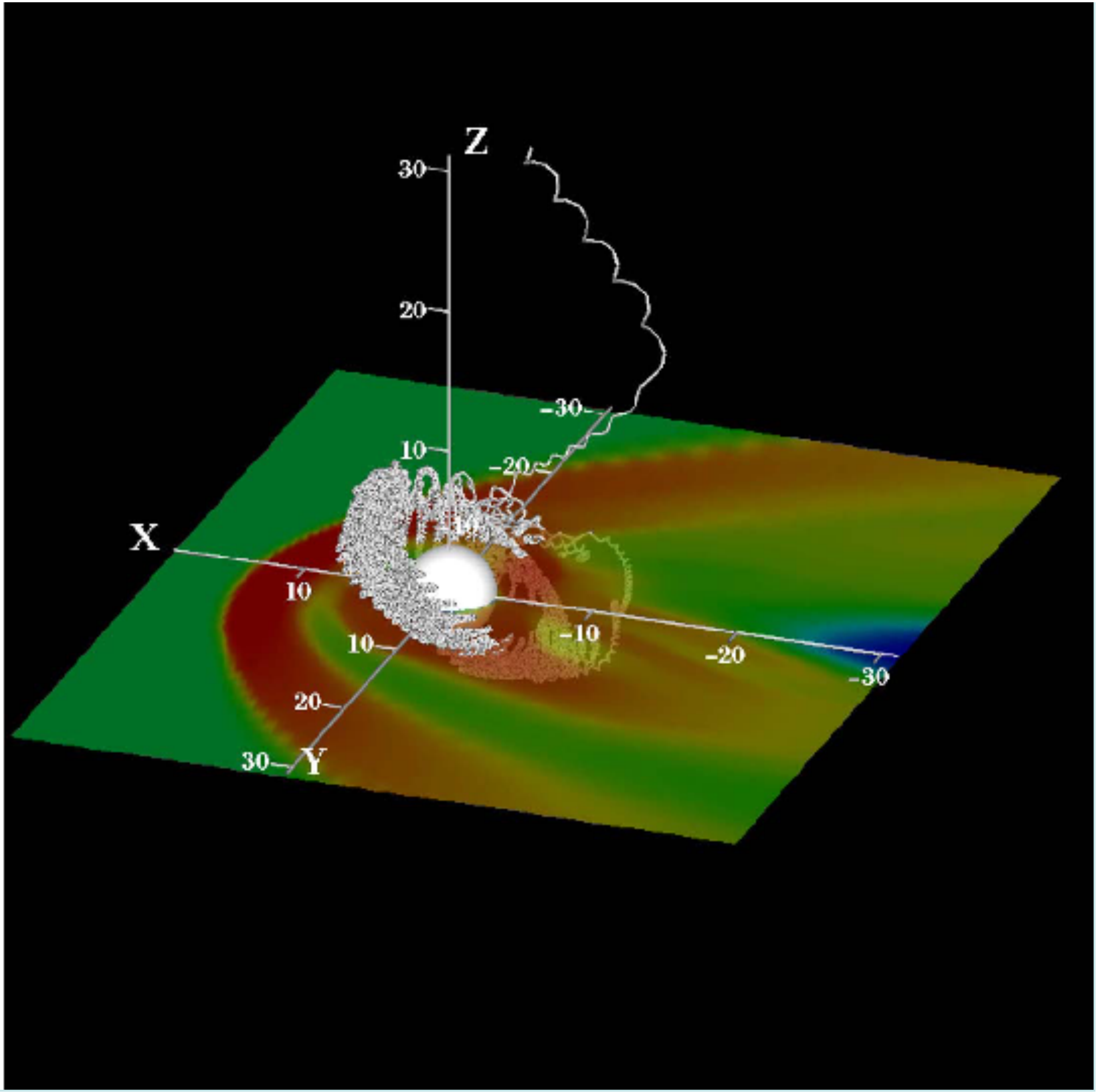

From R.L. Richard et al.

Radiation belts in the Earth' magnetosphere

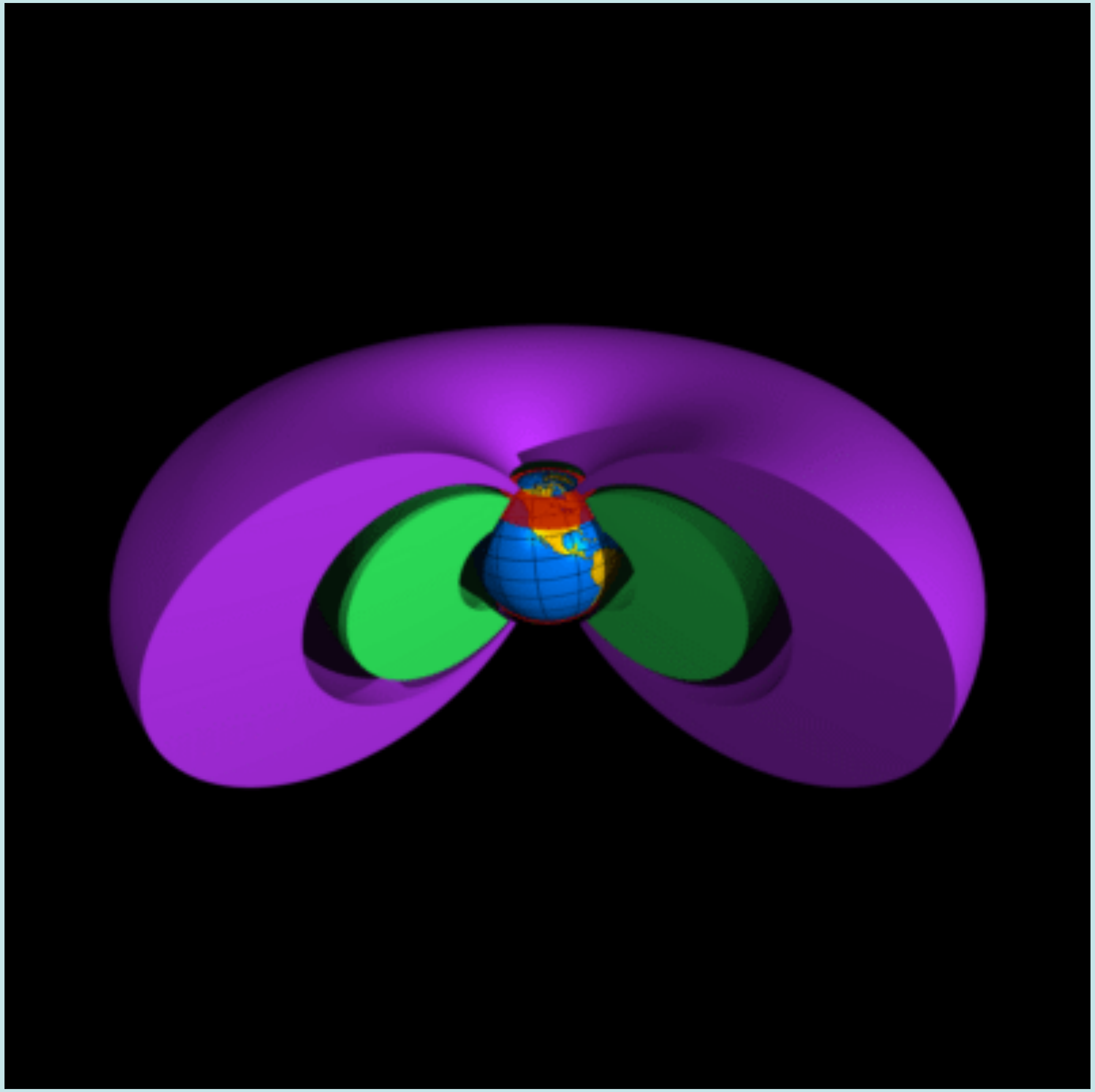

Outer and Inner Radiation Belts

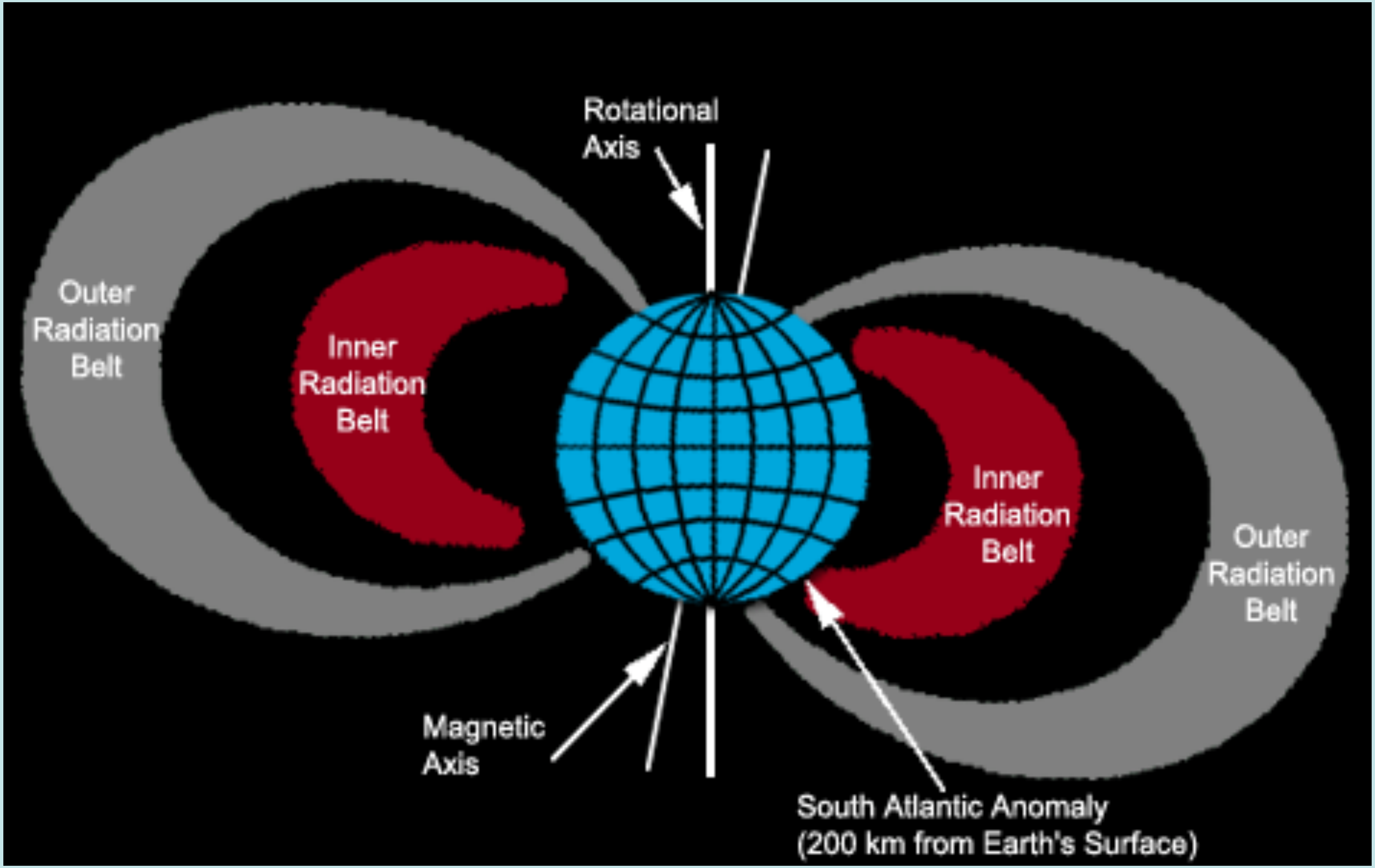

Trapping of energetic particles

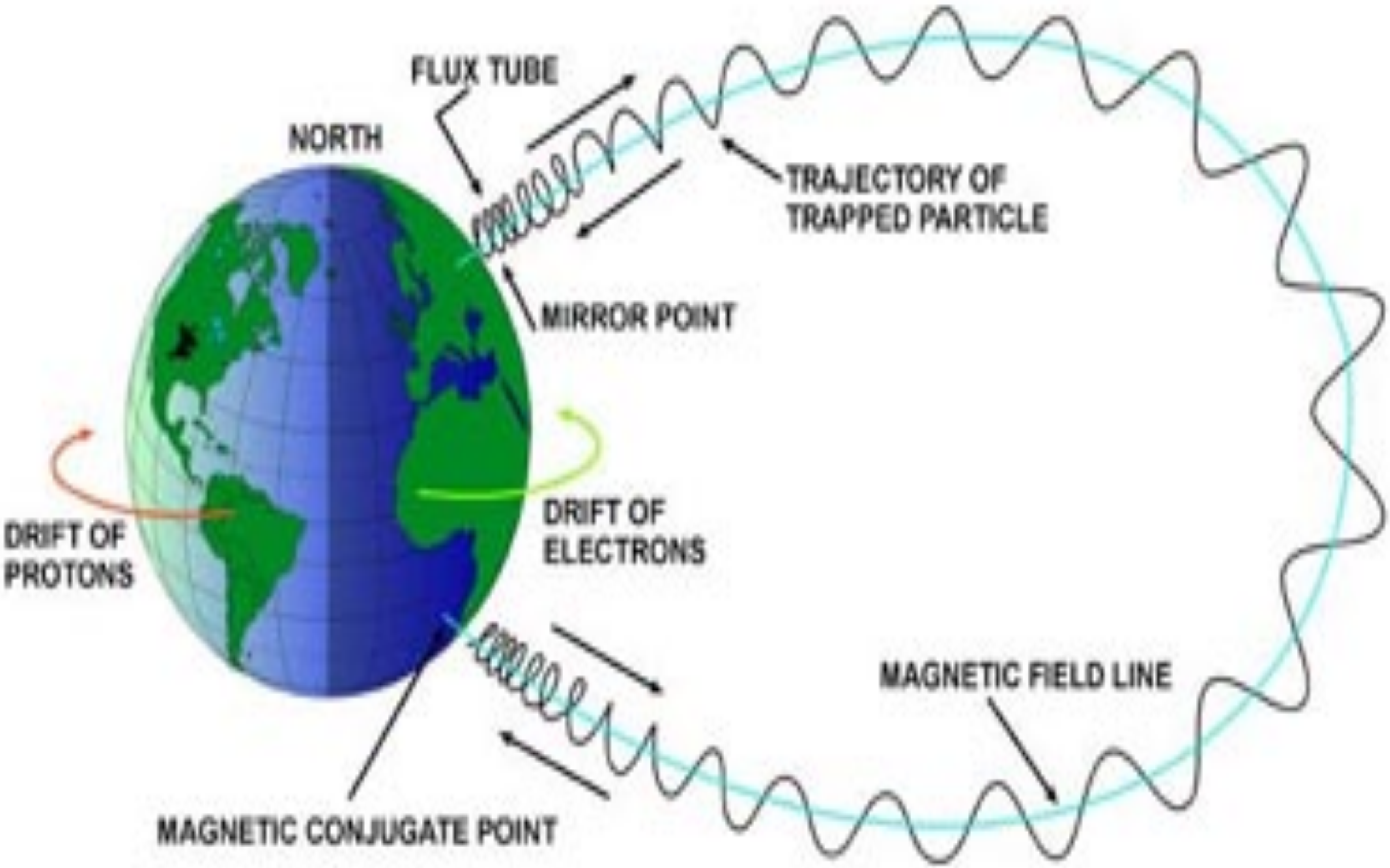

Space Weather and Radiation Belts

- Damage to telecommunication satellites and GPS: degradation of electronics and memory upsets
- Problem of radio-communications in high latitudes

Importance

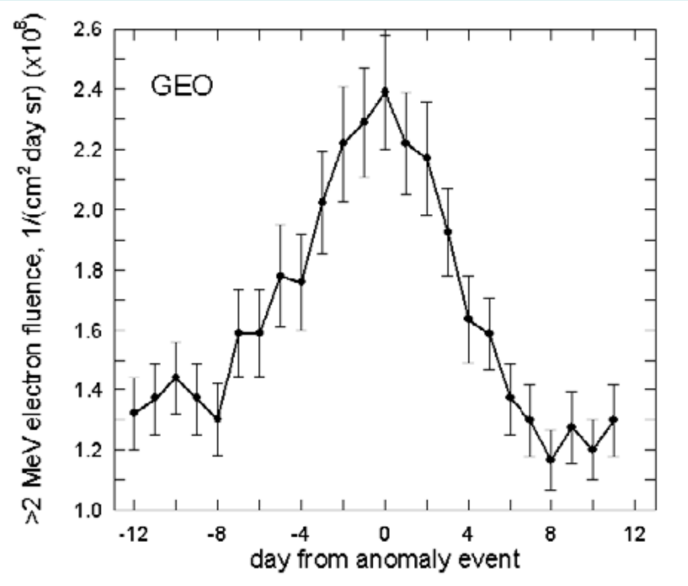

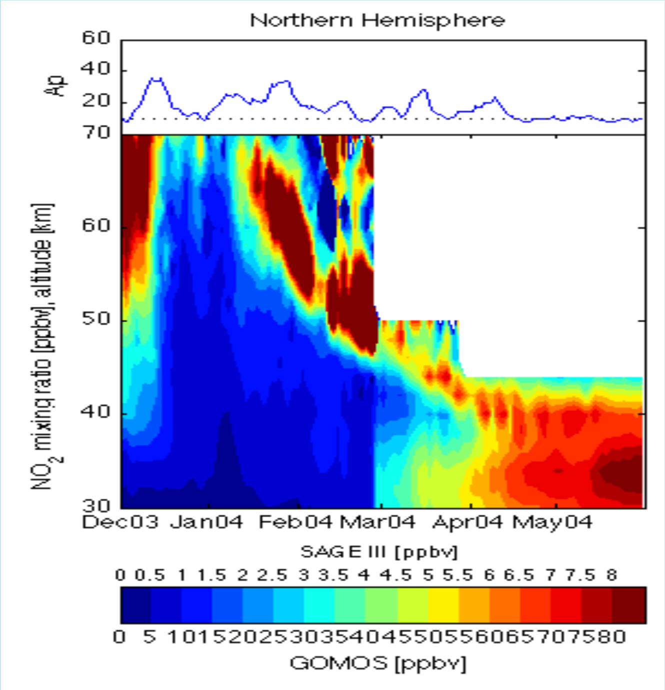

- MeV electrons cause satellite anomalies
- Iucci et al. [2005]

- Precipitation affects atmospheric chemistry (NOx), depletes ozone

Rozanov et al., GRL, [2005]
Clilverd et al., GRL, [2007]

- Solar activity may

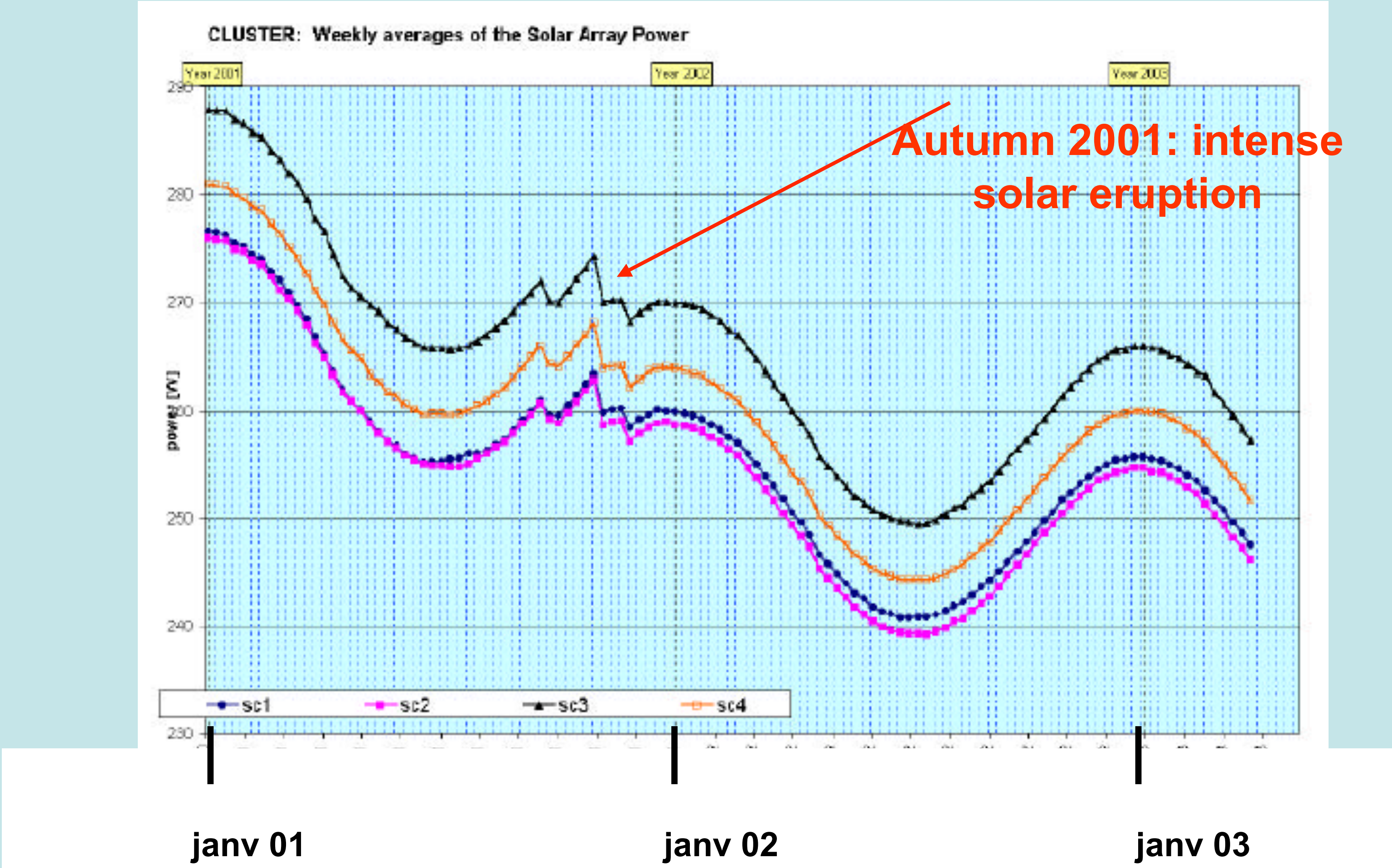

Inspite the dégradation of solar panels during the period of strong solar activity, the power rest is still suffisient

Earth's Radiation Belts

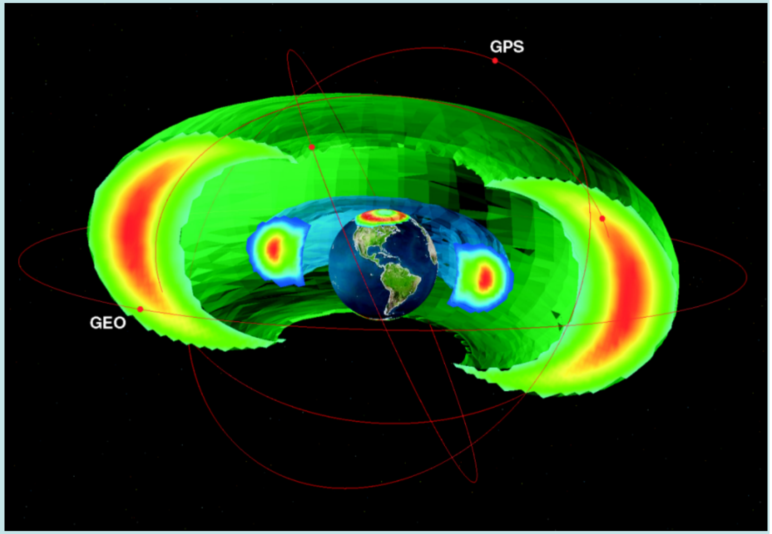

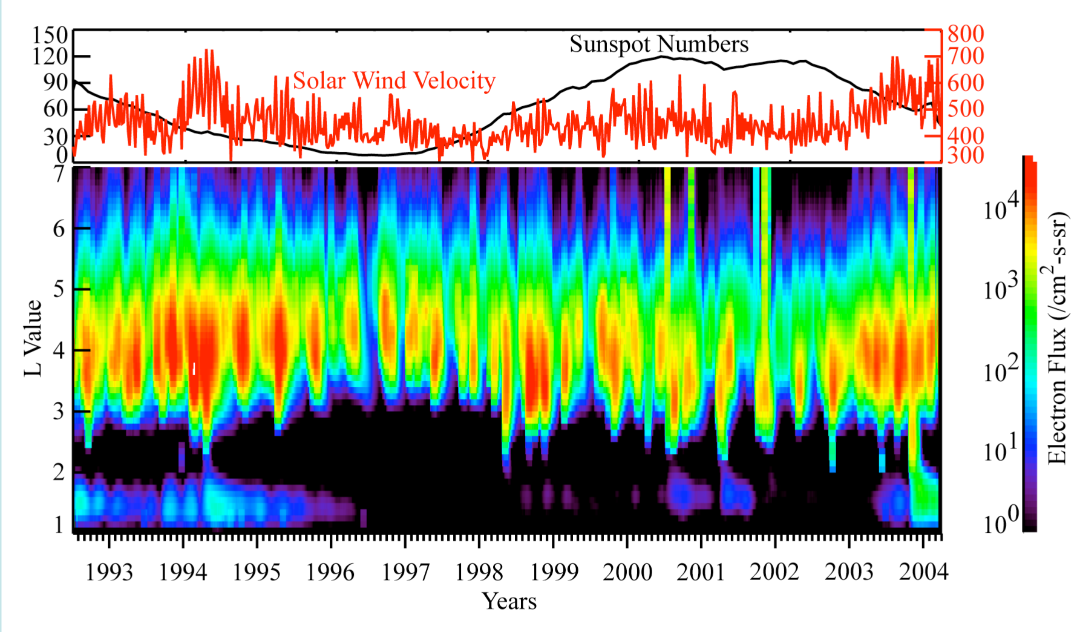

Baker and Kanekal, JASTP, 2007

- One proton belt
- Two electron belts
  - Energies > 1 MeV
  - Peaks near L=1.6 and 4.5

- How do you produce >1 MeV electrons?
- How do we explain the variability?

Radiation Belt Formation – Original Idea

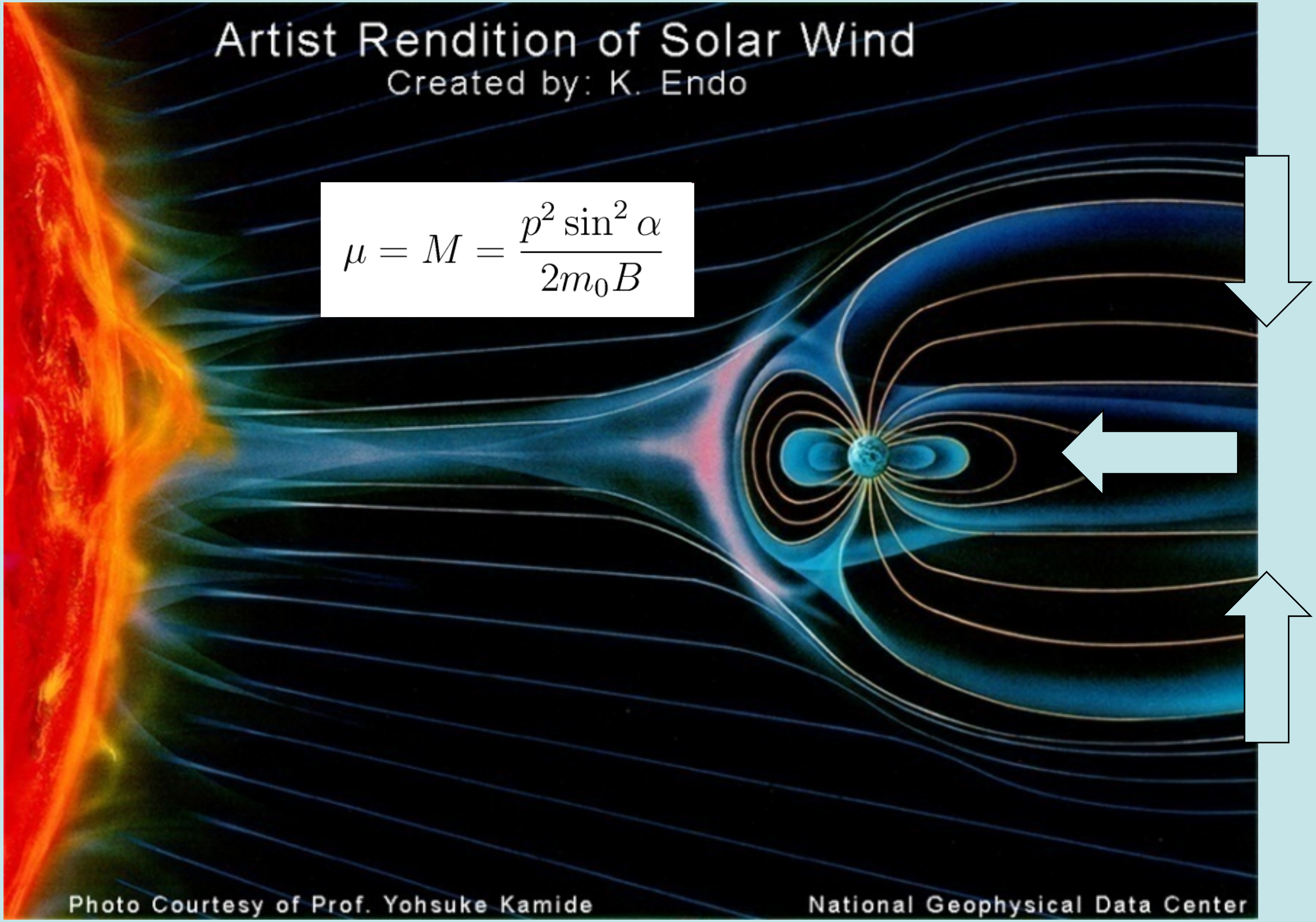

$$\mu = M = \frac{p^2 \sin^2 \alpha}{2m_0 B}$$

ULF Enhanced Radial Diffusion

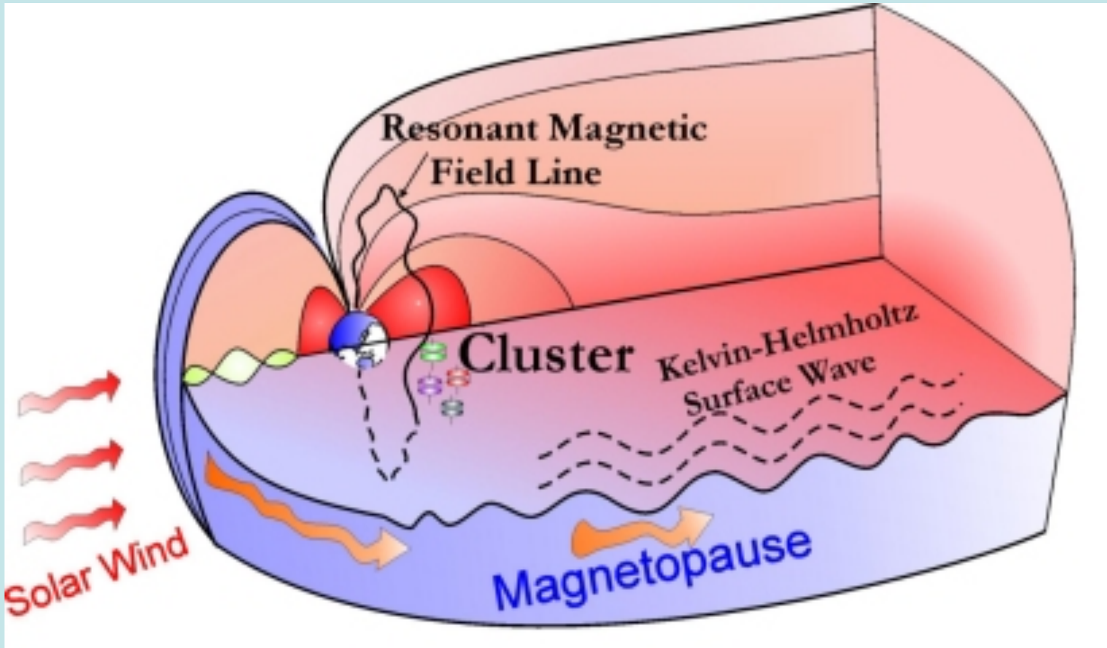

Horne et al., 2010

- Fast solar wind drives ULF waves inside magnetosphere
- ULF wave frequency ~ electron drift frequency
  - diffuse electrons towards the Earth
- Conservation of 1st invariant results in electron acceleration

The Original Idea is not Right

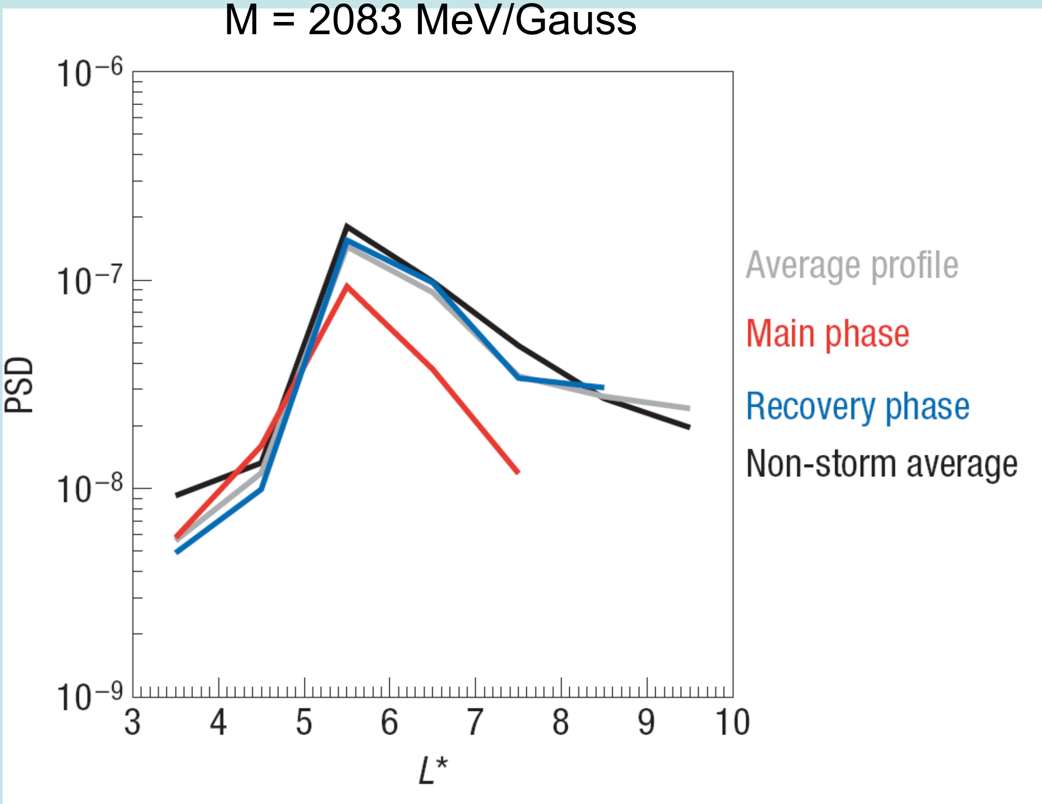

- **Peak in electron phase space density is near L=5.5**
- **Does not support radial diffusion from a source in the outer magnetosphere**
- **Suggests a new "local" acceleration mechanism**
- **Radial diffusion is still a major transport process**

Chen et al., Nature Physics, [2007]

From Horne et al., 2010

Development and validation of models of the radiation belts for solar cycle time scales. Example: Salammbo, AE8, AP8…

- The Salammbô code solves the three-dimensional phase-space diffusion equation for the electron radiation belts

- simple injection model to describe the dynamic behavior for relativistic electrons in the outer belt.
- The particles in the range 100 keV–500 keV are diffused throughout the belt.
- Particles with higher energies are ‘‘created’’ by acceleration of slower particles near the plasmapause location.

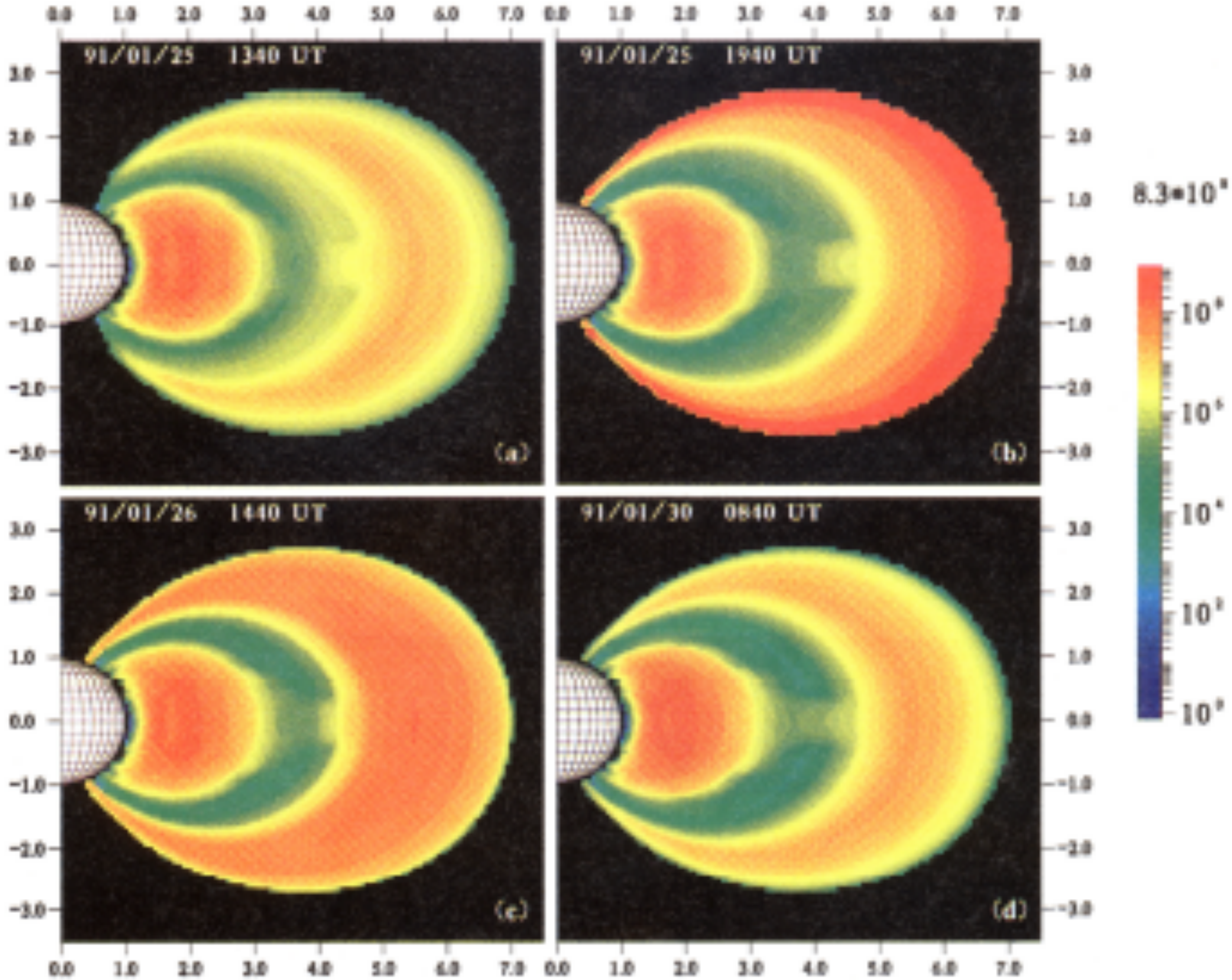

Plate 2. Omnidirectional differential flux maps (MeV^{-1} cm^{-2} s^{-1}) in L units for four times, one before and three after an injection of 1-hour in $L = 7$, for electrons with 200-keV kinetic energy.

Modeling and prediction

- **Physical phenomena to be taken into account**

1. **Radial diffusion due to electromagnetic perturbations**
2. **Friction due to Coulomb collisions with cold plasmaspheric electrons**
3. **Pitch angle diffusion by Coulomb interactions with atoms and molecules of the high atmosphere**
4. **Pitch angle diffusion by wave-particle interactions**

Dynamic Radiation Belt Models

- Simple physical
  - 1d radial diffusion

- Complex physical
  - MHD/field model + gyro-kinetic
  - Diffusion – 2d, 3d and 4d
    - Radial diffusion
    - Pitch angle diffusion
    - Energy diffusion

- Data assimilation
  - Needs physical model

Modelling Approach

Observations — **Transform to a dipole field (L*)** — **Diffusion Calculations**

Observations — **Use realistic magnetic field model** — **Gyro-kinetic Calculations**

- Both need good magnetic field models
- Diffusion - complexity in transformations
- Gyro-kinetic - complexity in wave diffusion

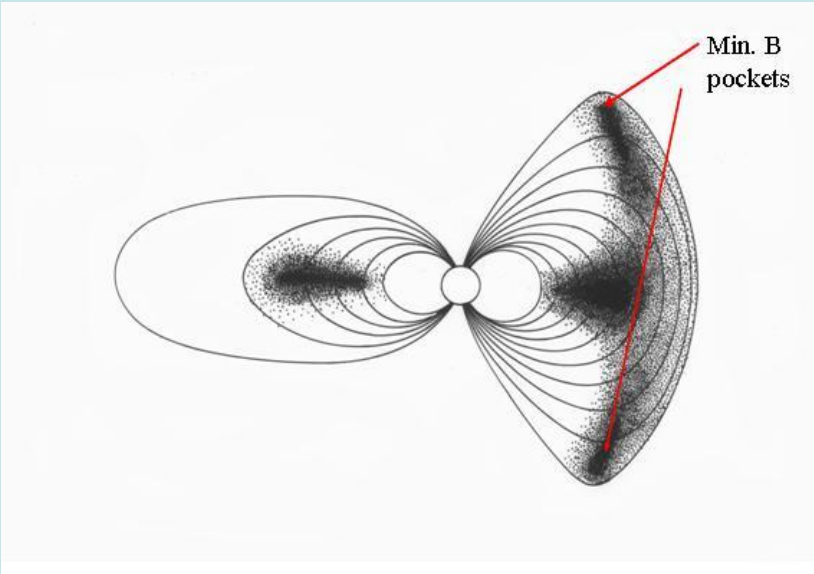

3d Global Modelling: Basic Equations

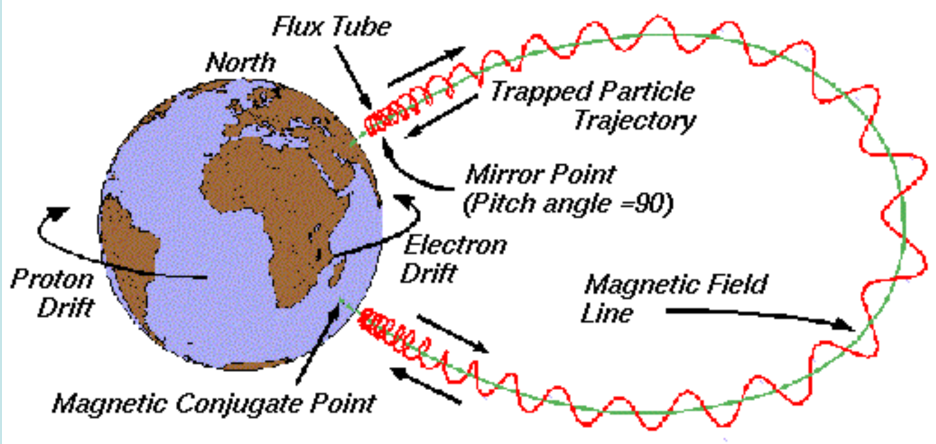

- Electron motion has 3 components
  - drift, bounce, gyration
- Each motion has an associated adiabatic invariant
- Use this fact to describe radiation belt variations by a diffusion equation
- f is the phase space density
- J_i are the 3 adiabatic invariants
- D_{JJ} are diffusion coefficients

$$\frac{\partial f}{\partial t} = \sum_{i,j=1}^{3} \frac{\partial}{\partial J_i} D_{J_i J_j} \frac{\partial f}{\partial J_j}$$

- Difficult to specify boundary conditions in terms of J_i
- Electron flux is usually measured in energy, pitch angle, position
- Diffusion coefficients are calculated in terms of energy, pitch angle, not J_i and therefore must be transformed

3d Global Modelling

- Transform from invariants (J_1, J_2, J_3) to (α , E, L*) or (y, p, L*)

$$
\begin{aligned}
\frac{\partial f}{\partial t} &= L^2 \frac{\partial}{\partial L}\left(D_{LL} L^{-2} \frac{\partial f}{\partial L}\right) \\
&+ \frac{1}{p^2}\frac{\partial}{\partial p}\left(p^2 \langle D_{pp}\rangle \frac{\partial f}{\partial p} + p^2 \langle D_{py}\rangle \frac{\partial f}{\partial y}\right) \\
&+ \frac{1}{T(y)y}\frac{\partial}{\partial y}\left(T(y)y\langle D_{yy}\rangle \frac{\partial f}{\partial y} + T(y)y\langle D_{yp}\rangle \frac{\partial f}{\partial p}\right) - \frac{f}{\tau}
\end{aligned}
$$

- but now we must include cross diffusion terms – added complexity
- Radial diffusion is for constant J_1 and J_2, - OK on a (J_1,J_2,L*) grid
- However
  - Momentum diffusion is for constant (L*,y)
  - Pitch angle diffusion (y) is for constant (L*,p)
  - Requires complex differential operators
- Solution - use 2 grids – and transform between them

Diffusion Coefficients

- D_{LL}
- Driven by ULF waves
- Drives radial diffusion (transport) across the magnetic field
- Function of magnetic activity (Kp), pitch-angle, energy and L shell
- From [Brautigam & Albert, JGR ,2000]

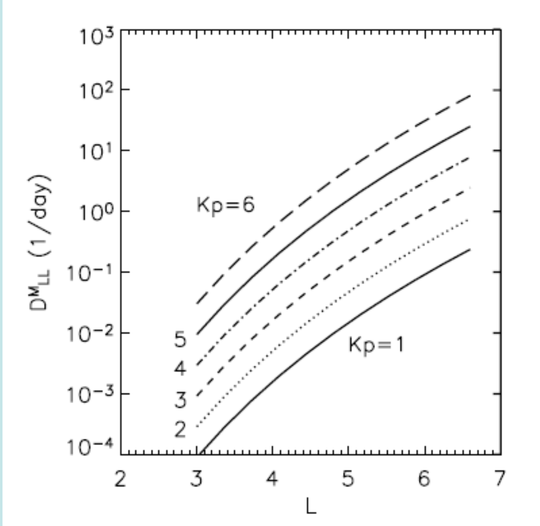

- $D_{\alpha\alpha}$ and D_{EE}
- Driven by wave-particle interactions
- Drive acceleration and loss
- Function of wave power pitch-angle, energy and L shell
- Chorus and hiss wave power scaled to AE (or Kp)
- Typically the wave distribution is supposed to be Gaussian in frequency after Lyons, 1973

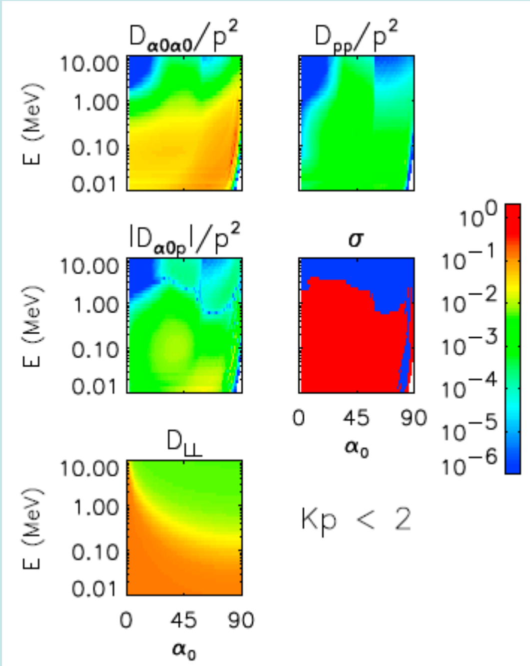

Salammbo Model

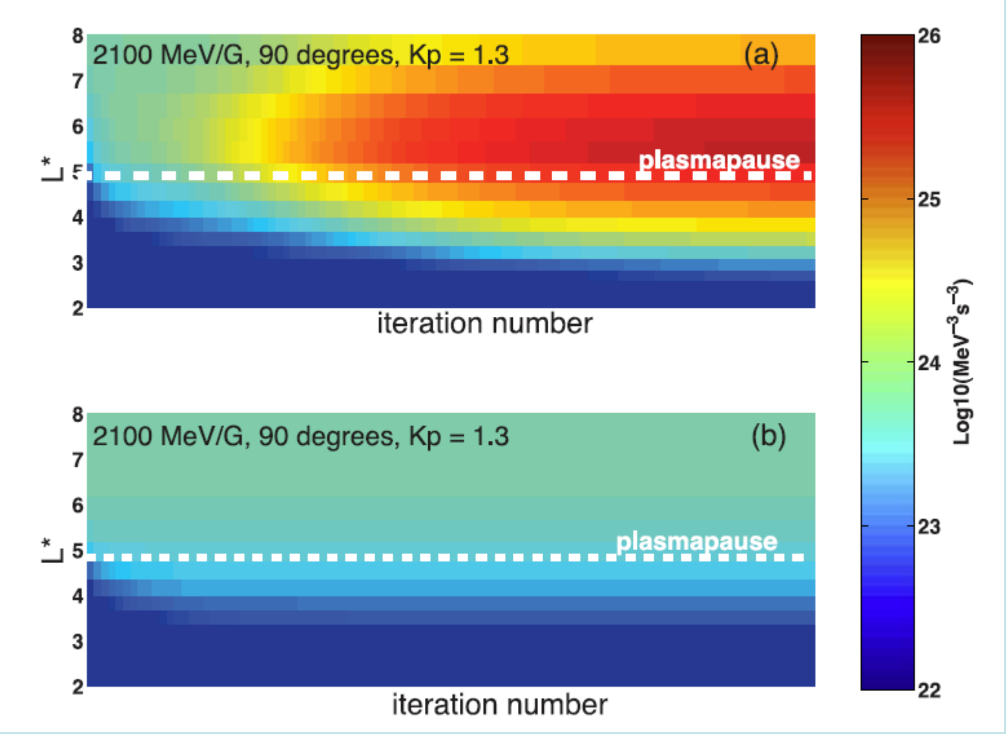

- **[Varotsou et al. 2005, 2008; Horne et al., 2006]**
- **Radial diffusion + wpi due to chorus – steady state**
- **No cross terms**
- **Significant increase in electron flux due to chorus acceleration**

$$\frac{\partial f}{\partial t} = L^2 \frac{\partial}{\partial L}\left(\frac{D_{LL}}{L^2}\frac{\partial f}{\partial L}\right) + \frac{1}{yT}\frac{\partial}{\partial y}\left(yTD_{yy}\frac{\partial f}{\partial y}\right) + \frac{1}{a}\frac{\partial}{\partial E}\left(aD_{ee}\frac{\partial f}{\partial E}\right) - \frac{1}{a}\frac{\partial}{\partial E}\left(a\frac{dE}{dt}f\right) \quad (1)$$

Radiation Belt Environment Model

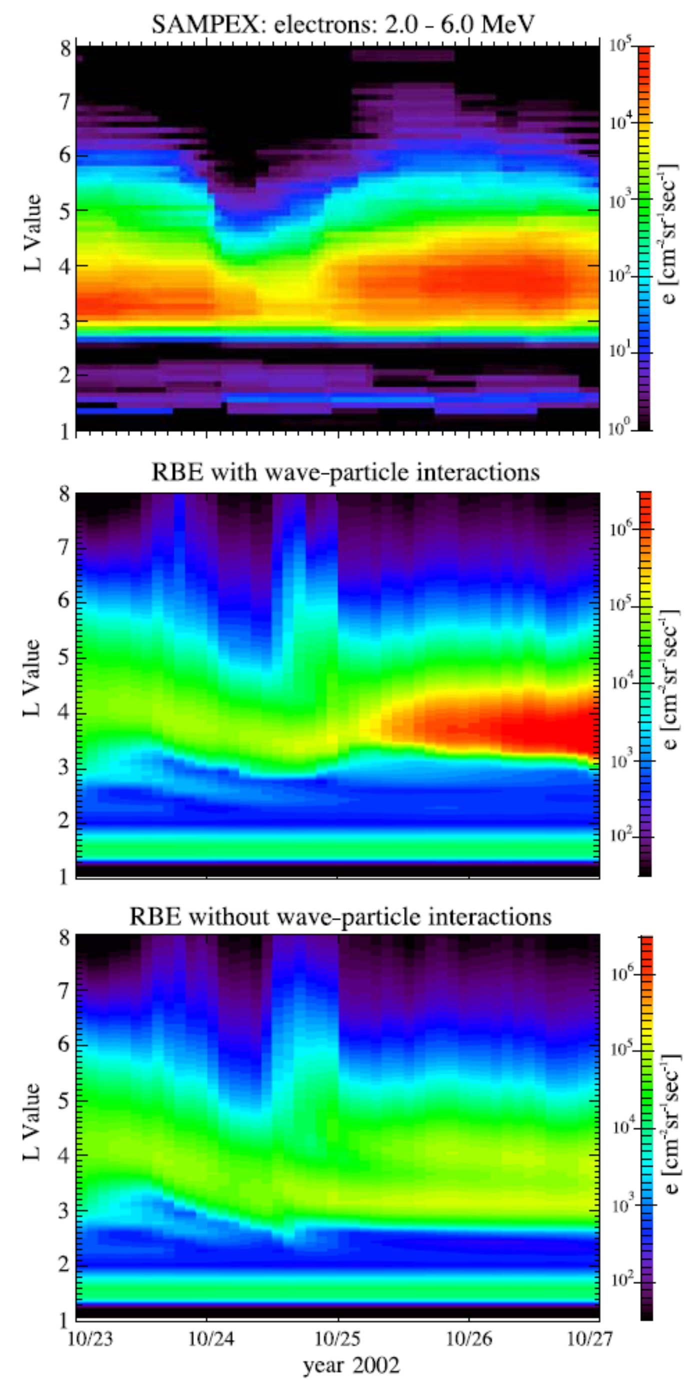

- **SAMPEX data**
- **2-6 MeV electrons**

- Fok et al., [2008]
- Radial displacement + chorus
- No cross terms

- Model
- Transport and pi due to chorus

- Model
- Transport only

- Chorus waves are essential to explain dynamics

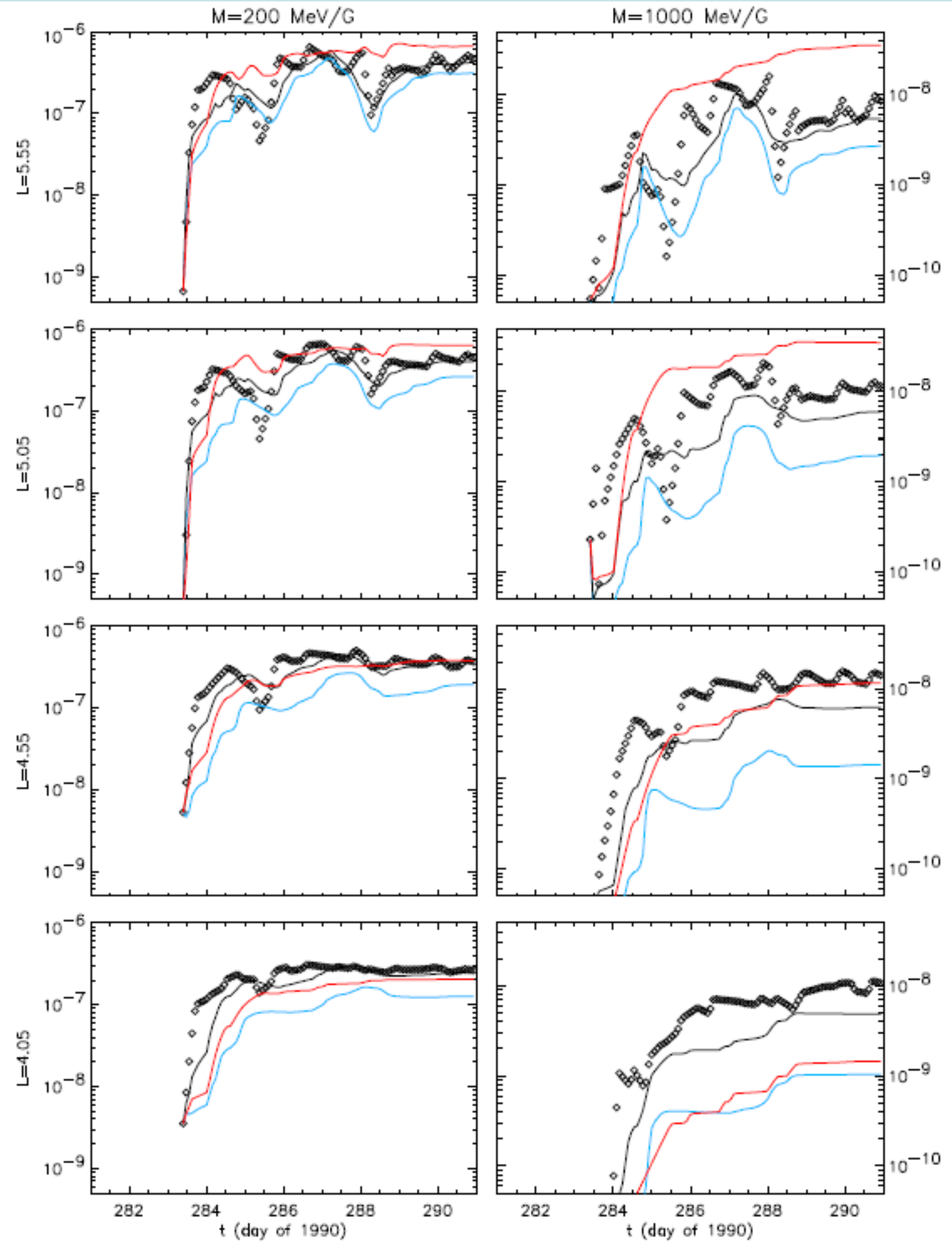

Albert et al. [2009]

- Radial diffusion+ chorus
- Includes cross terms
- 2 grids – coordinates of the second grid are chosen so the cross terms vanish

- Data – diamonds
- Radial diffusion - blue
- Chorus- red
- RD + chorus – black

- Radial diffusion + chorus give best agreement with data

- Cross terms reduce chorus acceleration

VERB Code

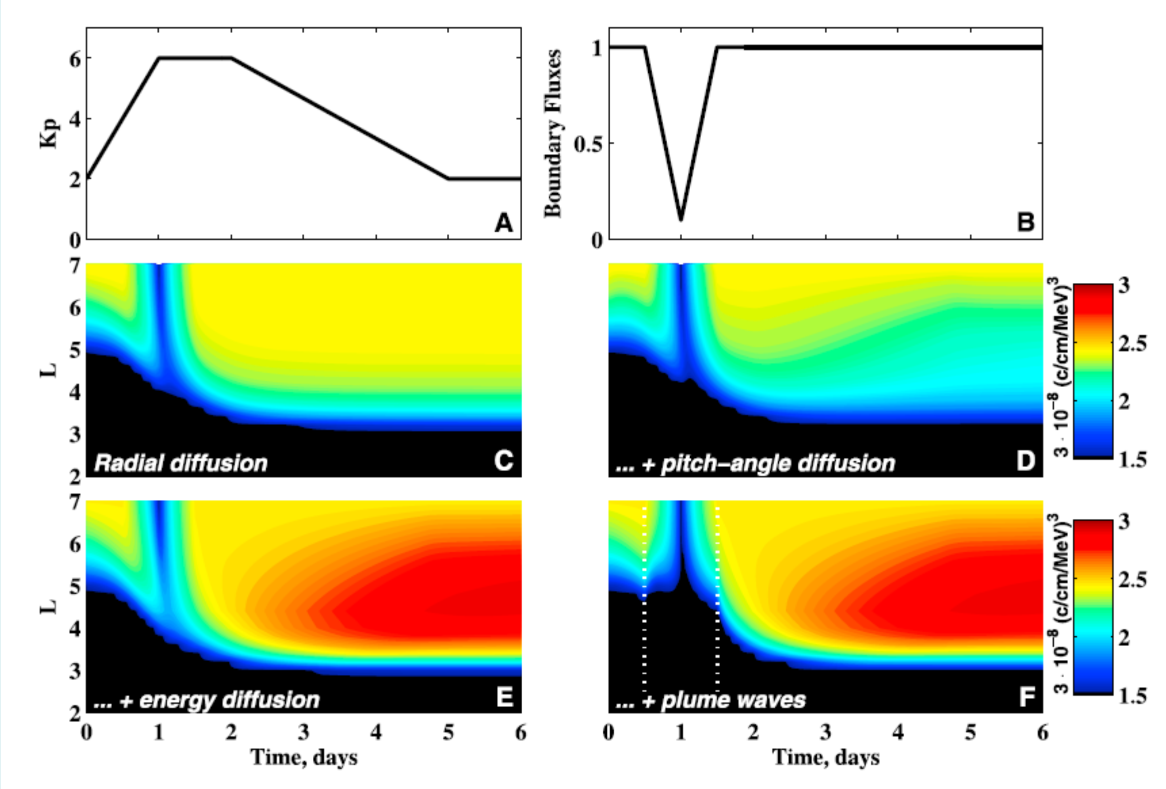

- Subbotin and Shprits [2009], Shprits et al., 2009]
- Radial diffusion + chorus, hiss, EMIC
- 2 grids, no cross terms
- Chorus acceleration essential
- Flux drop-out – by outward radial diffusion
- EMIC waves – important for > 2 MeV electrons

BAS code – Effects of Hiss Wave Normal Angle

Data **BAS Model**

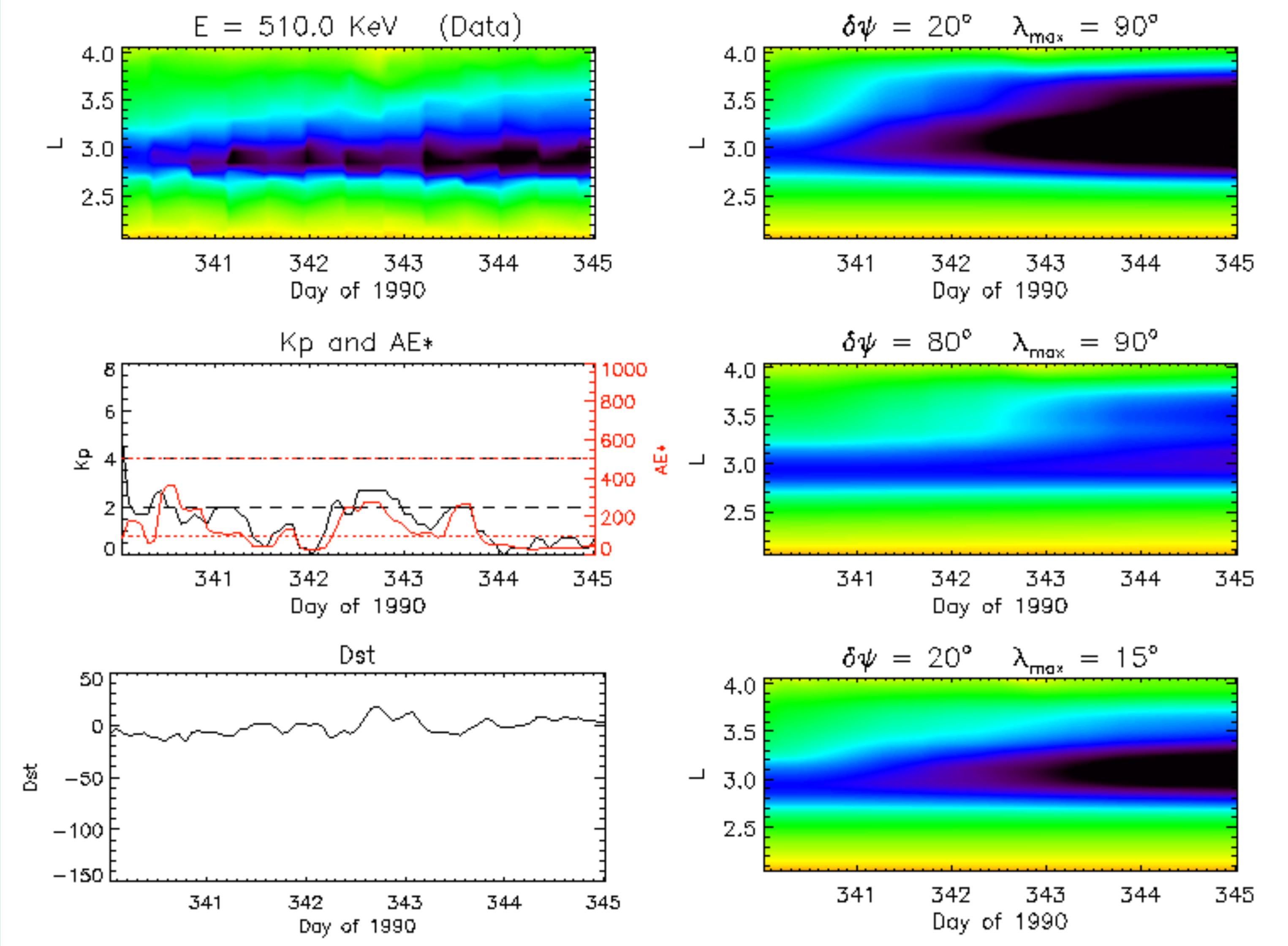

Radiation Belt Storm Probes Mission to be launched in 2012 (NASA)

- **To understand the acceleration, global distribution, and variability of energetic electrons and ions in the inner magnetosphere.**
- **Prioritized specific objectives:**
- **1) *the acceleration and transport of radiation particles*;**
- **2) the *precipitation and loss of radiation particles*;**
- **3) understanding *the creation and decay of new radiation belts*;**

Radiation Belt Storm Probes Mission (NASA)

- 4) quantifying the relative contribution of adiabatic and nonadiabatic processes on energetic particles;
- 5) understanding the role of "seed" or source populations for relativistic particle events;
- 6) understanding the effects of the ring current and other storm phenomena on radiation electrons and ions;
- 7) understanding how and why the ring current and associated phenomena vary during storms; and
- 8) developing and validating specification models of the radiation belts for solar cycle time scales.

Radiation Belt Storm Probes Mission (NASA)

- **Set of measurements, as recommended by the LWS Geospace Mission Definition Team, that have been identified as being of highest priority:**

- **Radiation belt electrons**
- **Vector magnetic field**
- **Ring current particles**
- **AC magnetic fields (search coil)**
- **DC/AC electric fields**

Adiabatic Invariants

$$\mu = M = \frac{p^2 \sin^2 \alpha}{2m_0 B}$$

$$\mathbf{J}_2 = 2 \oint_{m1}^{m2} p_{\parallel} dl$$

$$\mathbf{J}_3 = q \int \mathbf{B}.d\mathbf{s} = q\Phi$$

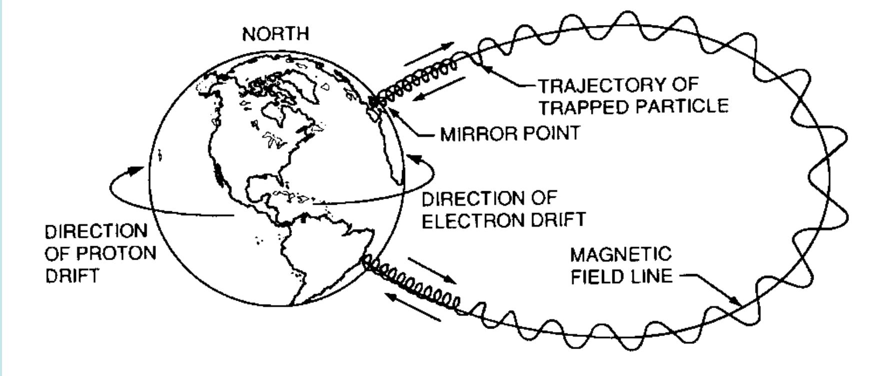

- **Cyclic motion**
  - **3 adiabatic invariants**
- **If conserved**
  - **no net acceleration or loss**
- **Acceleration requires breaking 1 or more invariant**
- **Requires E, B fields at frequencies**
  - **drift ~ 0.1-10 mHz**
  - **bounce ~ Hz**
  - **gyration ~ kHz**

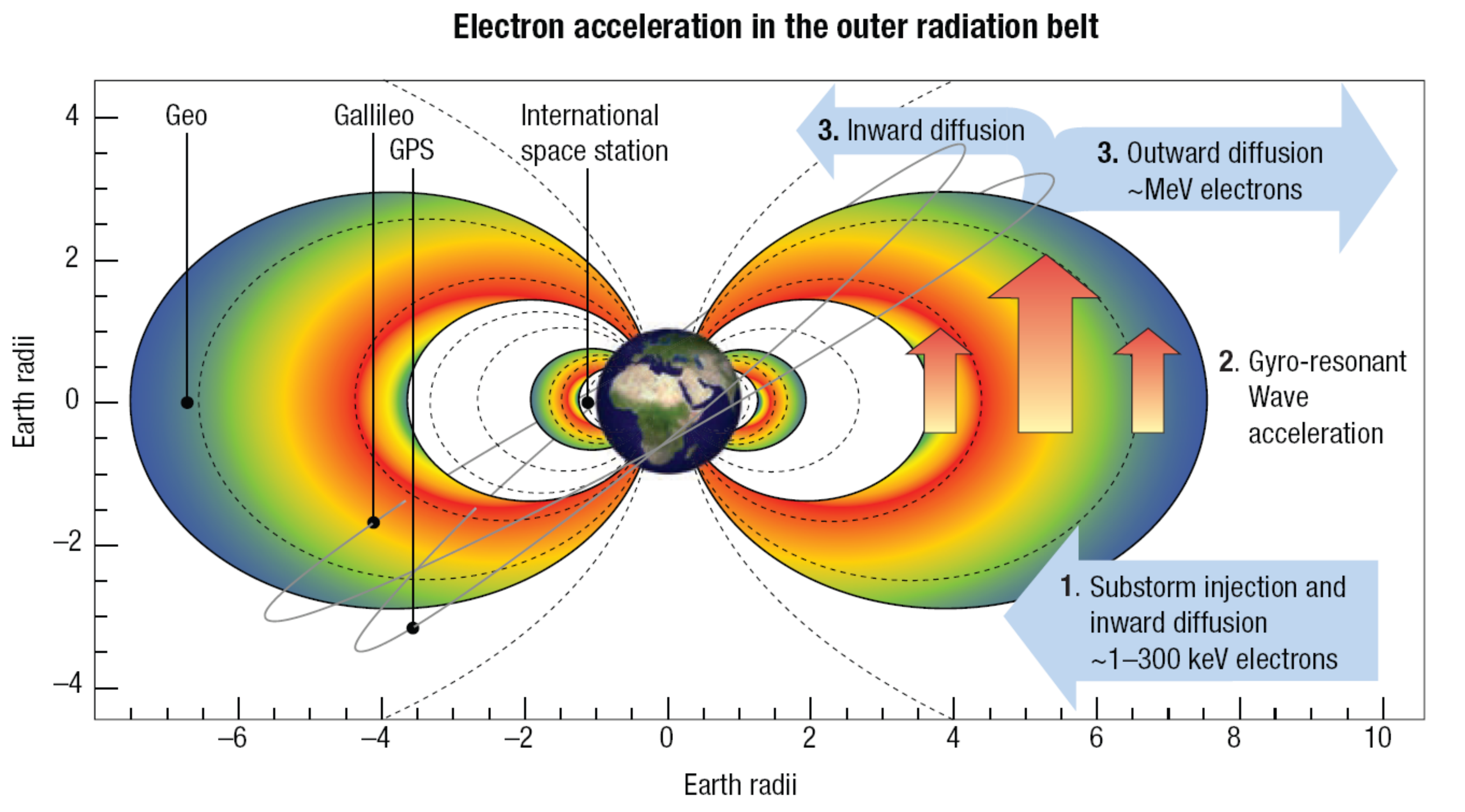

Horne, *Nature Physics* [2007]

- **Wave particle interaction**

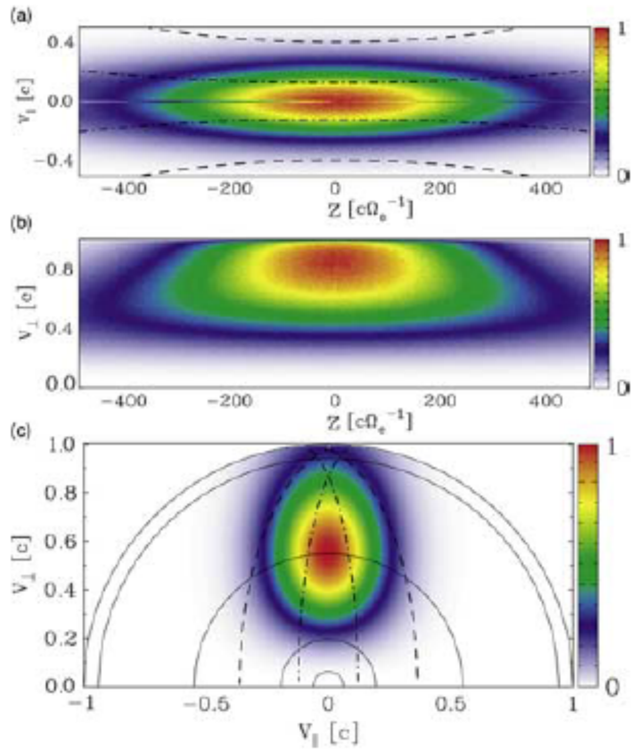

Figure 1. (a, b) Initial distribution functions of energetic electrons in ($v_\parallel$, z) and ($v_\perp$, z), respectively. Dashed and dash-dotted lines in Figure 1a denote resonance velocities, $v_r = \pm(\omega - eB_z/m_e)/k$, for frequencies $\omega = 0.2$ and 0.5 Ω_e, respectively. (c) Initial velocity distribution function in ($v_\parallel$, $v_\perp$) at the magnetic equator. Dashed and dash-dotted lines represent resonance ellipses of $\omega = 0.2$ and 0.5 Ω_e, respectively. Five solid semicircles denote constant energy contours of 1, 10, 100 keV and 1 MeV, and the speed of light, respectively. The color scale in each plot is shown in an arbitrary unit.

Wave-particle interaction with the whistler wave

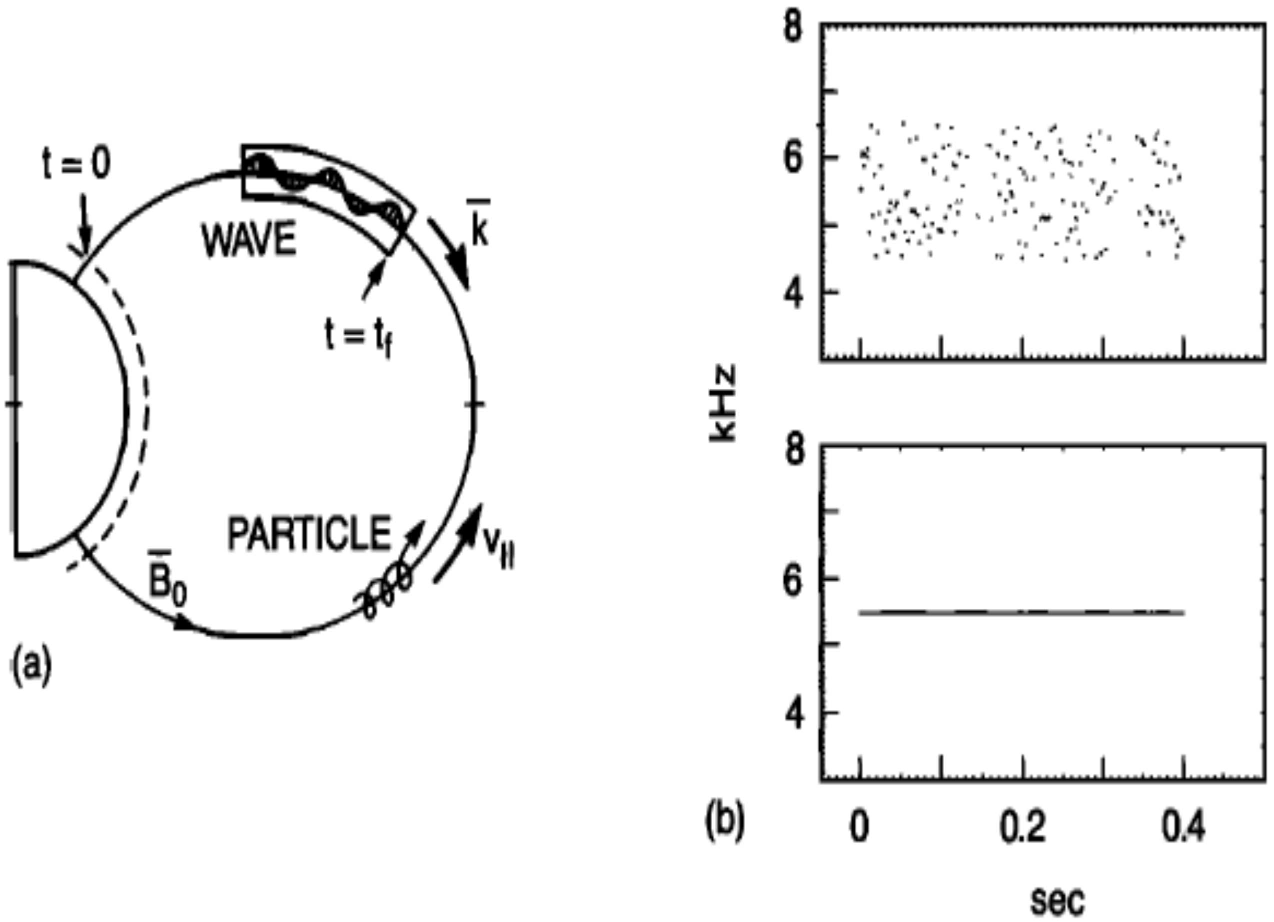

Fig. 1. (*a*) Schematic description of the wave–particle interaction phenomenology. (*b*) The frequency–time spectra of the incoherent and coherent wave packets used for comparison.

Particle angular scattering in case of single wave and wave spectrum

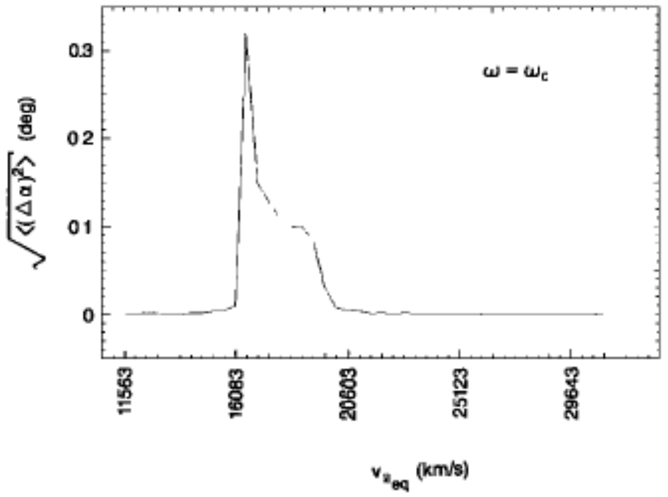

Fig. 8. Root mean square scattering induced by a coherent 400-ms-long wave packet at 5.5 kHz and having an equatorial wave magnetic field intensity of 1 pT, shown as a function of particle parallel velocity $v_{\parallel eq}$. All particles encounter the wave packet at the equator, and trajectories of 12 test particles at each $v_{\parallel eq}$ are computed to obtain the resultant root mean square scatter $\sqrt{\langle(\Delta\alpha)^2\rangle}$. The sharp peak at $v_{\parallel eq} \simeq 16,535$ km s^{-1} is due to the fact that these particles are very nearly resonant at the time they enter the wave packet and hence undergo large scattering.

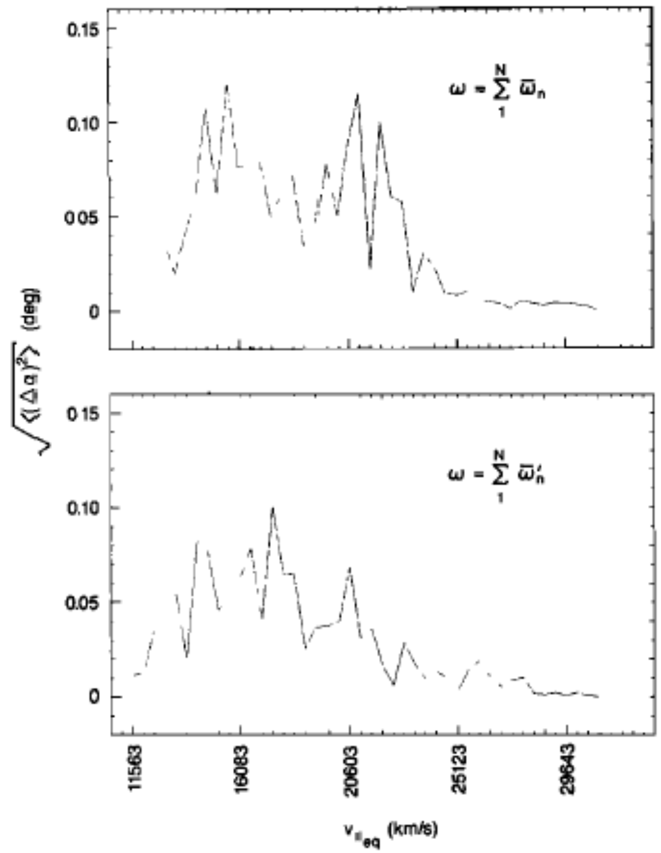

Fig. 9. Root mean square scattering induced by an incoherent wave packet, shown as a function of particle parallel velocity $v_{\parallel eq}$. All particles encounter the wave packet at the equator, and trajectories of 12 test particles at each $v_{\parallel eq}$ are computed to obtain the resultant root mean square scatter $\sqrt{\langle(\Delta\alpha)^2\rangle}$. The two panels show results for two different random frequency sequences $\bar{\omega}_n$.

Wave particle interaction in case of coherent wave and wave spectrum (from Inan, 1987)

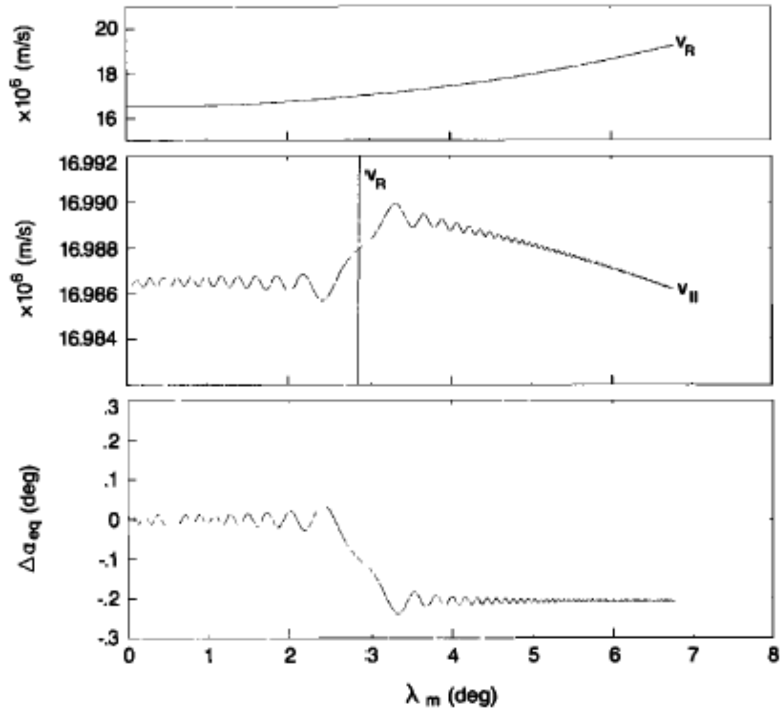

Fig. 2. The trajectory of a test particle in a coherent wave packet of 400 ms duration. All quantities are shown as a function of geomagnetic latitude λ_m. The particle encounters the wave front at the equator ($\lambda_m = 0°$). The top panel shows the resonance velocity v_R, the center panel the local particle parallel velocity $v_\parallel$ on an expanded scale, together with the v_R, and the lower panel the equatorial pitch angle change $\Delta\alpha_{eq}$. The initial equatorial pitch angle for the particle is $\alpha_{eq} = 5.5°$ and the initial Larmor phase is $\phi_0 = -90°$.

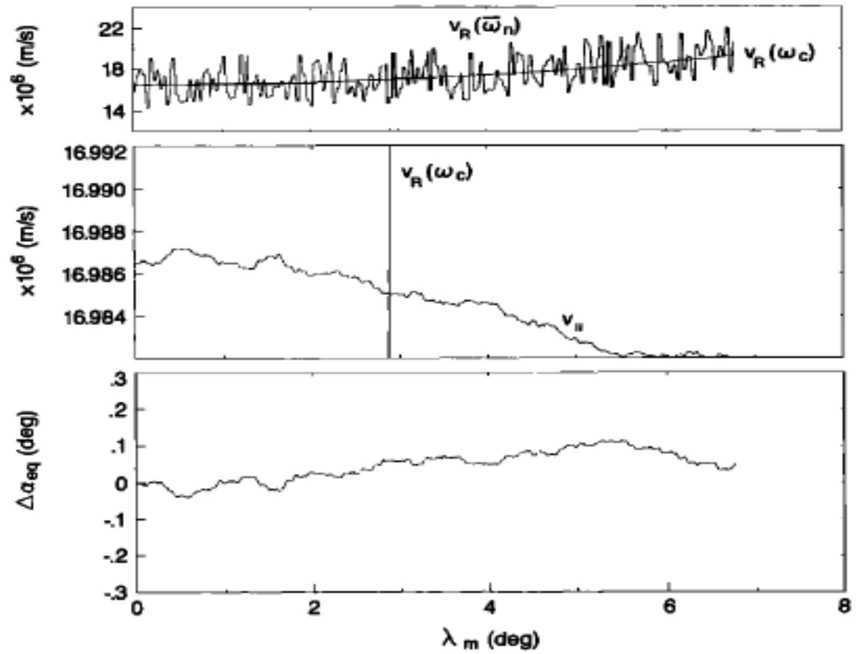

Fig. 4. The trajectory of a test particle in an incoherent wave packet of 400 ms duration. All quantities are shown as a function of geomagnetic latitude λ_m. The particle is assumed to encounter the wave front at the equator ($\lambda_m = 0°$). The top panel shows the resonance velocity $v_R(\bar{\omega}_n)$ corresponding to the random frequency sequence $\bar{\omega}_n$, and for reference the $v_R(\omega_c)$ corresponding to the band center frequency. The center panel shows the particle parallel velocity $v_\parallel$ together with the $v_R(\omega_c)$ on a significantly expanded scale, and the lower panel shows the equatorial pitch angle change $\Delta\alpha_{eq}$. The initial particle parameters are the same as those in Figure 2.

Quasilinear Diffusion

$$\frac{\partial f_0}{\partial t} = \nabla.(\mathbf{D}.\nabla f_0) = \frac{1}{p \sin\alpha}\frac{\partial}{\partial\alpha}\sin\alpha\left(D_{\alpha\alpha}\frac{1}{p}\frac{\partial f_0}{\partial\alpha} + D_{\alpha p}\frac{\partial f_0}{\partial p}\right) + \frac{1}{p^2}\frac{\partial}{\partial p}p^2\left(D_{p\alpha}\frac{1}{p}\frac{\partial f_0}{\partial\alpha} + D_{pp}\frac{\partial f_0}{\partial p}\right), \tag{1}$$

$$D_{\alpha\alpha} = \frac{p^2}{2}\left\langle\frac{(\Delta\alpha)^2}{\Delta t}\right\rangle \tag{2}$$

$$D_{\alpha p} = \frac{p}{2}\left\langle\frac{\Delta\alpha\Delta p}{\Delta t}\right\rangle \tag{3}$$

$$D_{pp} = \frac{1}{2}\left\langle\frac{(\Delta p)^2}{\Delta t}\right\rangle, \tag{4}$$

PADIE code

$$B^2(\omega) = \begin{cases} A^2 \exp\left(-\left(\frac{\omega - \omega_m}{\delta\omega}\right)^2\right) & \omega_{lc} \leq \omega \leq \omega_{uc} \\ 0 & \text{otherwise,} \end{cases} \quad (5)$$

$$g(X) = \begin{cases} \exp\left(-\left(\frac{X - X_m}{X_w}\right)^2\right) & X_{\min} \leq X \leq X_{\max} \\ 0 & \text{otherwise,} \end{cases} \quad (7)$$

where $X = \tan(\psi)$, X_w is the angular width and X_m is the peak. Using these definitions, the diffusion coefficients (derived in Appendix A) are given by

PADIE code

$$D_{\alpha\alpha} = \sum_{n-n_l}^{n_h} \int_{X_{\min}}^{X_{\max}} XdXD_{\alpha\alpha}^{nX} \quad (8)$$

$$D_{\alpha p} = D_{p\alpha} = \sum_{n-n_l}^{n_h} \int_{X_{\min}}^{X_{\max}} XdXD_{\alpha p}^{nX} \quad (9)$$

$$D_{pp} = \sum_{n-n_l}^{n_h} \int_{X_{\min}}^{X_{\max}} XdXD_{pp}^{nX}, \quad (10)$$

$$B = \frac{M\left(1 + 3\sin^2\lambda\right)^{\frac{1}{2}}}{L^3 R_e^3 \cos^6\lambda}, \quad (16)$$

Lyons et al., 1972 averaging procedure

$$\langle D_{\alpha_{eq}\alpha_{eq}} \rangle = \frac{1}{\tau_B} \int_0^{\tau_B} D_{\alpha\alpha} \left(\frac{\partial \alpha_{eq}}{\partial \alpha} \right)^2 dt \tag{21}$$

$$\langle D_{\alpha_{eq}p} \rangle = \frac{1}{\tau_B} \int_0^{\tau_B} D_{\alpha p} \left(\frac{\partial \alpha_{eq}}{\partial \alpha} \right) dt \tag{22}$$

$$\langle D_{pp} \rangle = \frac{1}{\tau_B} \int_0^{\tau_B} D_{pp} dt, \tag{23}$$

Lyons et al., 1972 averaging procedure

$$\langle D_{\alpha_{eq}\alpha_{eq}} \rangle = \frac{1}{T}\int_0^{\lambda_m} D_{\alpha\alpha} \frac{\cos\alpha}{\cos^2\alpha_{eq}} \cos^7\lambda d\lambda \qquad (24)$$

$$\langle D_{\alpha_{eq}p} \rangle = \frac{1}{T}\int_0^{\lambda_m} D_{\alpha p} \frac{\cos^4\lambda\left(1+3\sin^2\lambda\right)^{1/4} d\lambda}{\cos\alpha} \qquad (25)$$

$$\langle D_{pp} \rangle = \frac{1}{T}\int_0^{\lambda_m} D_{pp} \frac{\cos\lambda\left(1+3\sin^3\lambda\right)^{1/2} d\lambda}{\cos\alpha}, \qquad (26)$$

$$\tau_B = 4 \int_0^{\lambda_M} \frac{dl}{V_\parallel} = 4 \int_0^{\lambda_M} \frac{dl}{d\lambda} \frac{d\lambda}{V_\parallel} = \frac{4r_0}{V} s(\alpha_0)$$

$$T(\alpha_{eq}) = 1.30 - 0.56 \sin \alpha_{eq}. \tag{27}$$

Large amplitude whistlers observed onboard Stereo

L01105 CATTELL ET AL.: LARGE AMPLITUDE WHISTLERS L01105

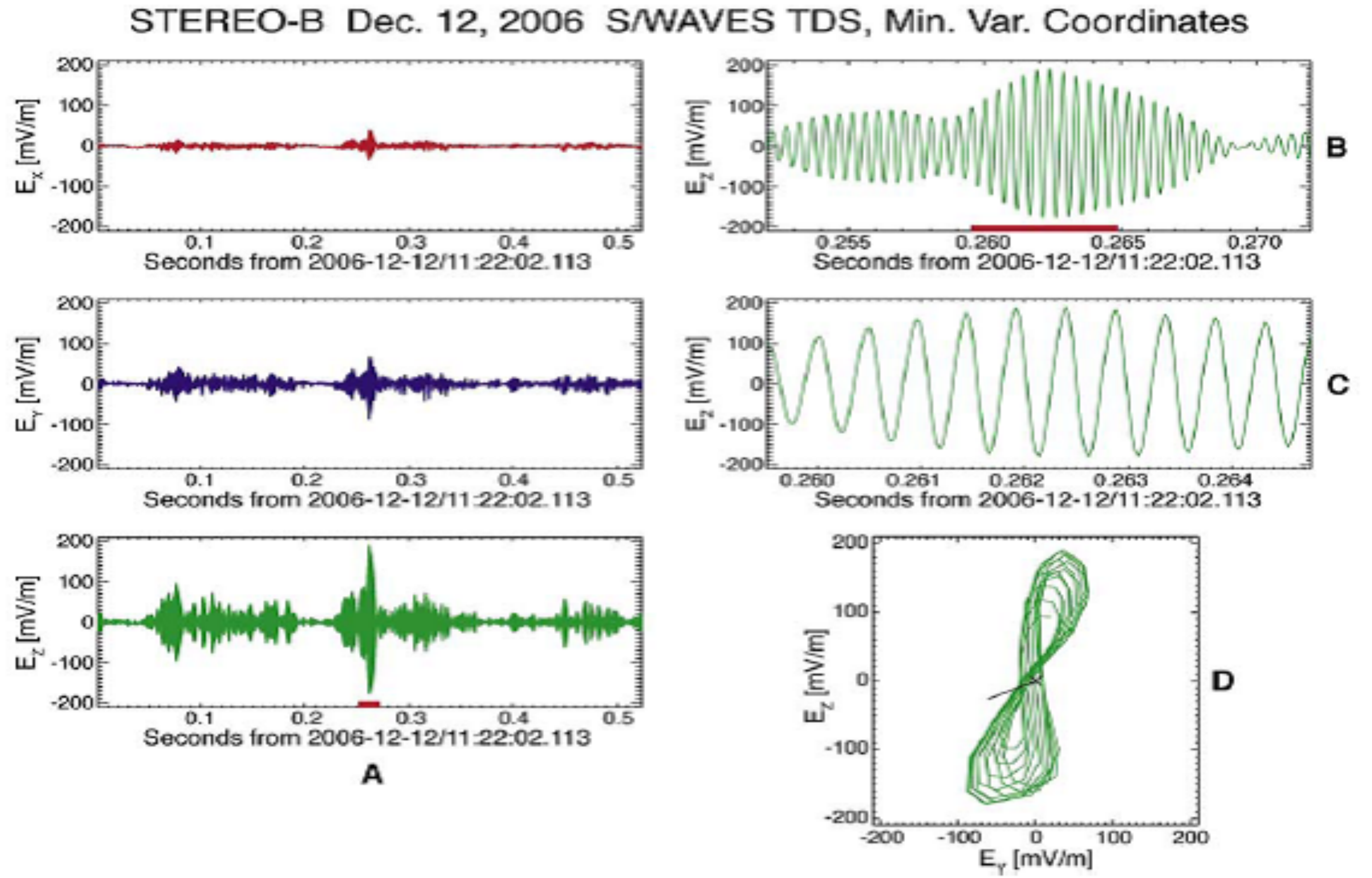

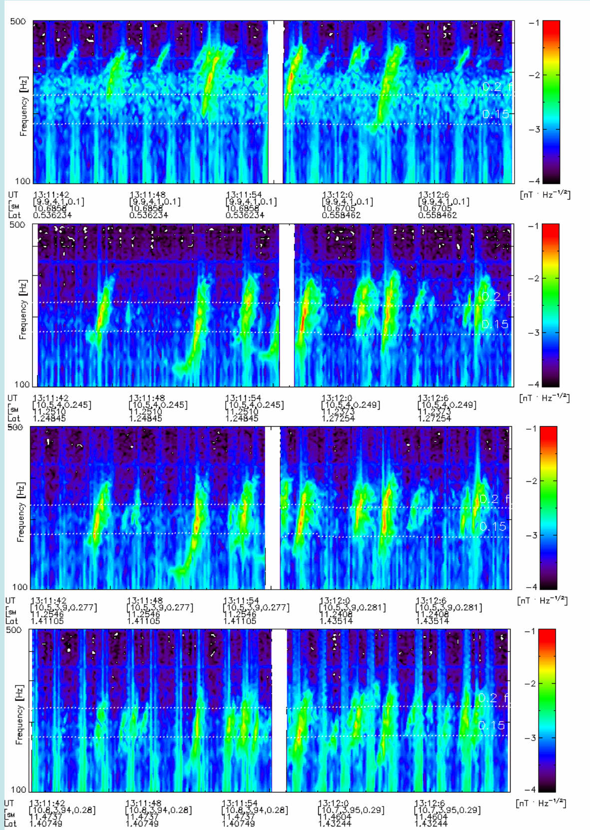

Time-frequency power spectrograms of magnetic and electric field fluctuations near the source region recorded by the search coil magnetometer (SCM**)** aboard the four THEMIS spacecraft on July 17, 2007. Panels show data from THB, THC, THD, and THE respectively (from Agapitov et al., 2010).

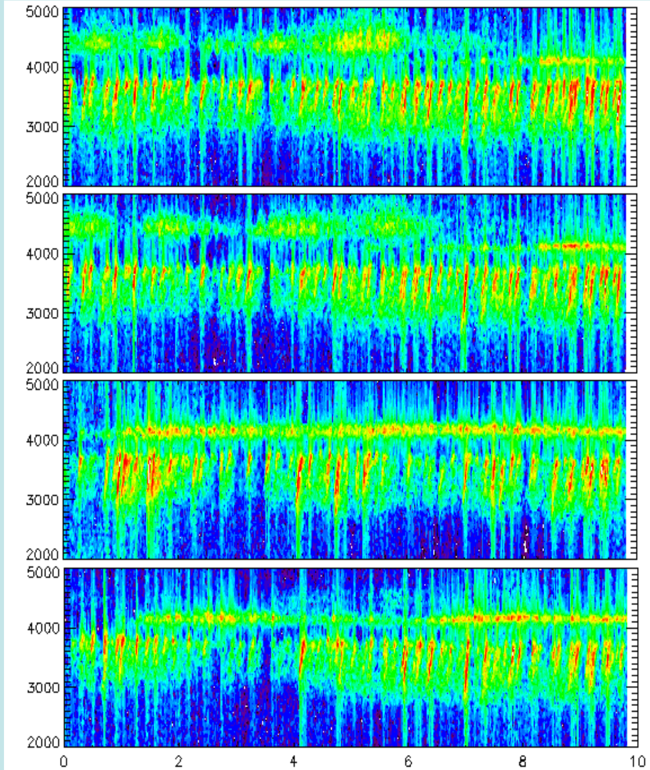

Time-frequency power spectrograms of electric field fluctuations captured by WBD instruments on board the four Cluster spacecraft on April 18, 2002. Panels from top to bottom show data from C1, C2, C3, and C4 respectively. The wave vector direction based on STAFF-SA spectral matrices data shows propagation along the background magnetic field (from Santolik and Gurnett, 2003 and Agapitov et al., 2011).

Types of emissions in ELF-VLF frequency range

Plasmaspheric hiss:

- incoherent whistler-mode (RH-polarized) waves;
- observed at frequencies ~100Hz - 3 kHz at all MLT values;
- maximum magnitudes in the post-noon/ evening sector.

Chorus:

- coherent whistler-mode waves;
- observed at frequencies 0.1 - 0.8 f_{e^-} (~ 2 - 6 kHz), often in two frequency bands below and above 0.5 f_{e^-};
- appear in dawn-midday sector near and outside plasmapause;
- often could not be distinguished from hiss emissions.

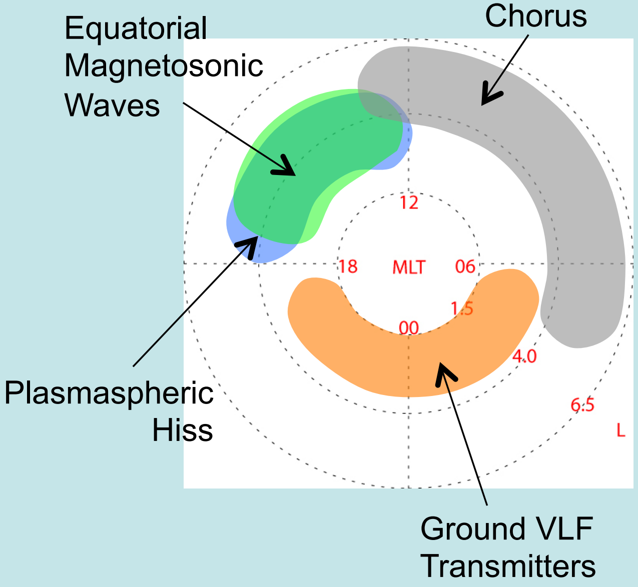

Schematic distribution of various types of electromagnetic emissions (based on DE-1 and Cluster datasets)

Acceleration and Loss by Wave-Particle Interactions

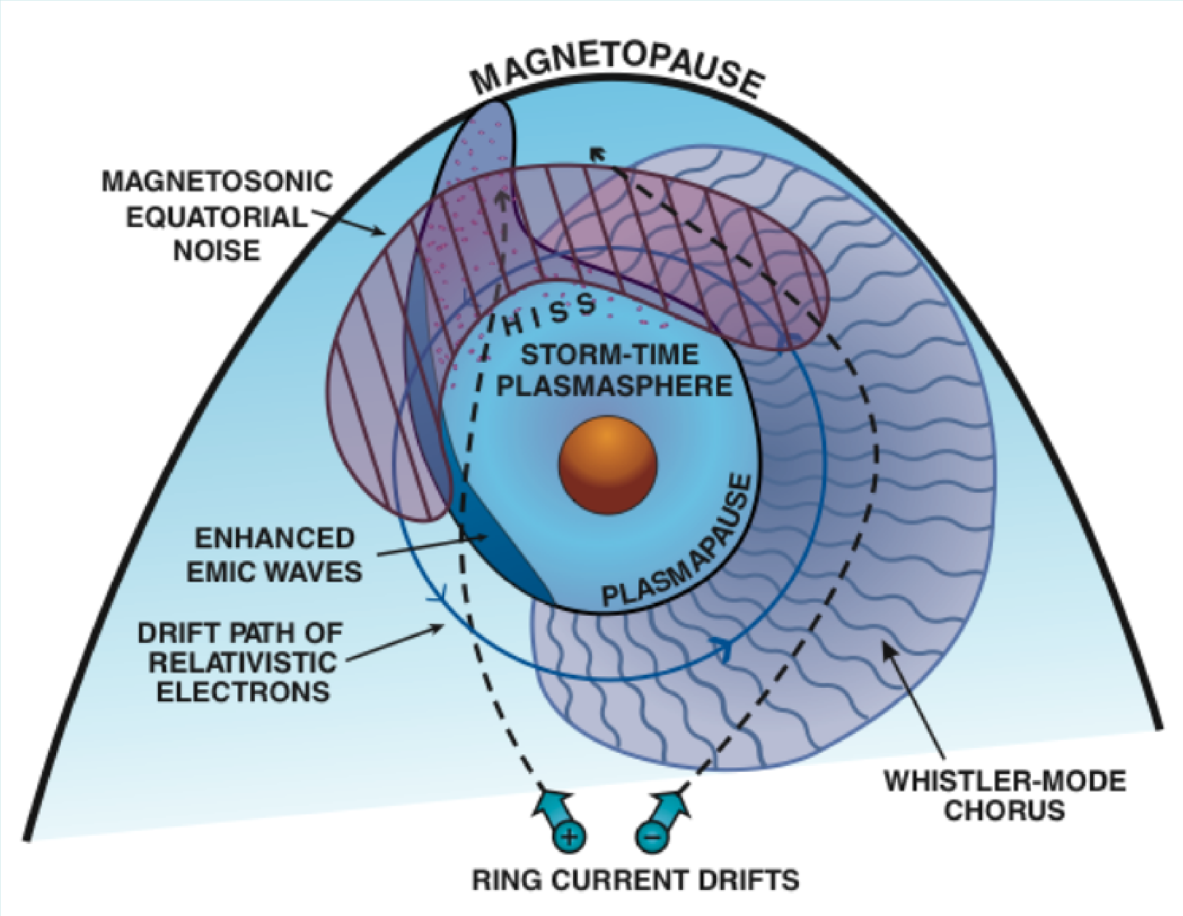

- **Particles encounter many types of waves:**

- **Chorus**
- **Hiss**
- **Lightning generated whistlers**
- **VLF transmitters**
- **EMIC**
- **Magnetosonic**
- **Z mode**
- **LO and RX modes**

Milestones in whistler study

Discovery of whistlers by *H. Barkhausen in 1919*

From Shklyar, 2010

Whistlers are very low-frequency electromagnetic waves produced by lightning that have a characteristic whistling sound when converted to audio. They propagate in the magnetosphere in, what is now called, whistler mode.

Dispersion relation for whistler-mode waves in dense ($\omega_p^2 \gg \omega_{\mathrm{H}}^2$) plasma for frequencies larger than the LHR frequency ($\omega^2 \gg \omega_{\mathrm{LH}}^2$), with θ being the wave normal angle:

$$\omega = \omega_{\mathrm{H}} |\cos\theta| \frac{k^2}{k^2 + q^2}\,; \quad q^2 = \frac{\omega_p^2}{c^2}\,, \tag{1}$$

which corresponds to the wave refractive index

$$N^2 \equiv \frac{k^2 c^2}{\omega^2} = \frac{\omega_p^2}{\omega(\omega_{\mathrm{H}}|\cos\theta| - \omega)}\,. \tag{2}$$

In this domain of parameters there exists a resonance cone determined by

$$|\cos\theta_r| = \omega/\omega_{\mathrm{H}} \tag{3}$$

at which the refractive index $N^2 \to \infty$.

From Shklyar, 2010

Milestones in whistler study

Relationship to lightning first suggested by *T.L. Eckersley in 1935*

The first comprehensive theory of whistler propagation developed by *R.L.O. Storey in 1953*: explanation of whistler "dispersion" and non-ducted guiding (*Storey's* theorem).

From Shklyar, 2010

For low frequency whistler mode waves, the group velocity increases with increasing frequency. In particular, for parallel propagation

$$v_g = 2\,\frac{\omega^{1/2}(\omega_{\mathrm{H}} - \omega)^{3/2}}{q\;\omega_{\mathrm{H}}}\,, \tag{5}$$

which, according to R.L.O. Storey, explains the "dispersion" of whistlers observed on spectrograms.

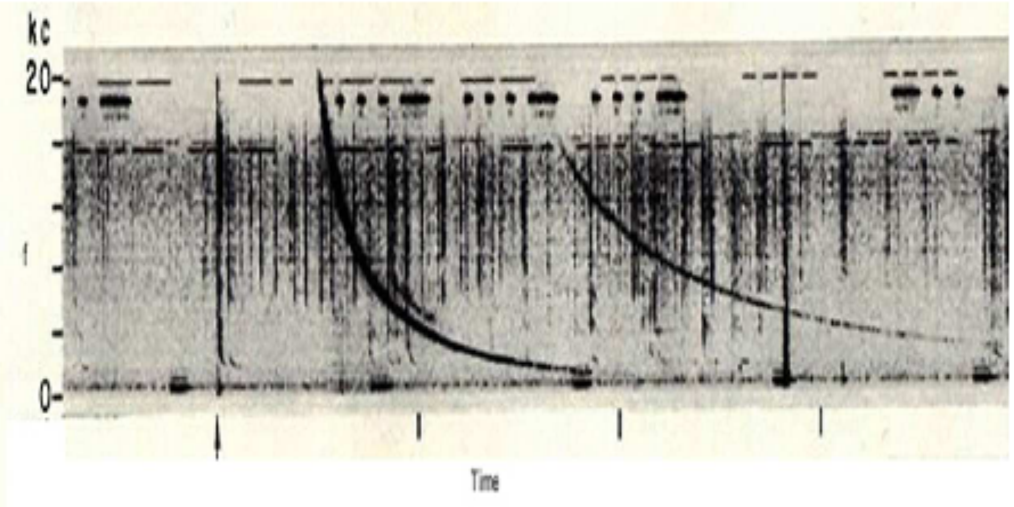

Early spectrogram representing whistlers.

From Shklyar, 2010

Storey's theorem (1953): *In the domain of parameters*

$$\omega_{LH} \ll \omega < \frac{\omega_H |\cos\theta|}{2}$$

the group velocity of whistlers does not deflect from the ambient magnetic field by an angle larger than $19,4712^o$.

Group velocity for whistler mode waves

$$v_{g\|} = \frac{\omega}{k}\cos\theta\left[\mathrm{tg}^2\,\theta + 2\left(1 - \frac{\omega}{\omega_H\cos\theta}\right)\right]\;;\; v_{g\perp} = \frac{\omega}{k}\sin\theta\left(1 - \frac{2\omega}{\omega_H\cos\theta}\right)\;,$$

which gives for the angle α between $\mathbf{v}_g$ and B_0

$$\mathrm{tg}\;\alpha \equiv \frac{v_{g\perp}}{v_{g\|}} = \mathrm{tg}\;\theta\frac{1 - \frac{2\omega}{\omega_H\cos\theta}}{\mathrm{tg}^2\,\theta + 2 - \frac{2\omega}{\omega_H\cos\theta}}\;. \qquad (4)$$

Maximum of this expression is reached for $\mathrm{tg}\;\theta = \sqrt{2}$ $\quad(\theta = 54,7356^o)$ and $\omega \to 0$, and is equal to $\sqrt{2}/4$, giving

$$\alpha_{max} = \mathrm{arctg}(\sqrt{2}/4) \equiv 19,4712^o\;.$$

From Shklyar, 2010

Milestones in whistler study

Discovery of anisotropic cyclotron instability for whistler mode waves: ***R.Z. Sagdeev, V.D. Shafranov, 1960***

From Shklyar, 2010

Kinetic growth rate for parallel propagating whistler mode waves: R.Z. Sagdeev and V.D. Shafranov (1960):

$$\gamma = \frac{2\pi^3 e^2 V_g}{mkc^2} \int_0^\infty dv_\perp v_\perp^3 \left(\frac{\partial f_0}{\partial v_\parallel} + \frac{\omega_c}{kv_\perp} \frac{\partial f_0}{\partial v_\perp} \right)_{v_\parallel = (\omega - \omega_c)/k} , \qquad (7)$$

where

$$V_g = \frac{2\omega}{k} \left(1 - \frac{\omega}{\omega_c} \right)$$

is the group velocity. For the energetic electron distribution typical of the magnetosphere, with a loss-cone and temperature anisotropy

$$f_0 = \left(\frac{m}{2\pi} \right)^{3/2} \frac{n_E}{T_\perp T_\parallel^{1/2} \Gamma(j+1)} \left(\frac{mv_\perp^2}{2T_\perp} \right)^j \cdot e^{-\frac{mv_\parallel^2}{2T_\parallel} - \frac{mv_\perp^2}{2T_\perp}} , \qquad (8)$$

where j is a positive number and $\Gamma(z)$ is Gamma-function, the unstable range is determined by

$$\frac{\omega}{\omega_c} < 1 - \frac{T_\parallel}{T_\perp (j+1)} . \qquad (9)$$

From Shklyar, 2010

Kinetic instability of the outer radiation belt:

A.A. Andronov and V.Yu. Trakhtengerts, 1964; C.F. Kennel and H.E. Petchek, 1966;

L.R. Lyons and D.J. Williams, 1975;

P.A. Bespalov and V.Yu. Trakhtengerts, 1980

Electron heating, pitch-angle diffusion, and precipitation described by quasi-linear theory: *R.M. Thorne and C.F. Kennel, 1971*

Invention of Alfven maser: *P.A. Bespalov and V.Yu. Trakhtengerts, 1986*

From Shklyar, 2010

Discovery of plasmapause: ***D.L. Carpenter, N. Brice, and M. Trimpi, 1960-1966***

The book by ***Helliwell, 1965.*** **The first most profound summary and a superlative contribution to whistler studies.**

From Shklyar, 2010

Role of ions in whistler propagation and prediction of magnetospheric reflection: *I. Kimura, 1966*

From Shklyar, 2010

Effects of ions on whistler wave propagation: I. Kimura (1966).
Dispersion relation with the account of ions:

$$\omega^2 = \frac{\omega_{\mathrm{LH}}^2}{1 + q^2/k^2} + \frac{\omega_H^2 \cos^2\theta}{(1 + q^2/k^2)^2} \,. \qquad (6)$$

From (6) it follows that for $\omega < \omega_{\mathrm{LH}}$ the wave normal angle θ may reach $\pi/2$ ensuring wave reflection from the region where $\omega \lesssim \omega_{\mathrm{LH}}$.

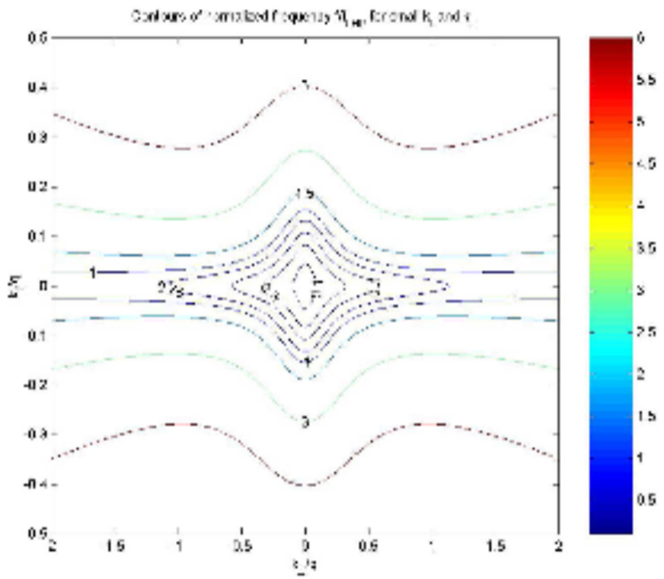

Surface of refractive index for $\omega \sim \omega_{\mathrm{LH}}$.

From Shklyar, 2010

Mission CLUSTER2 : Orbits

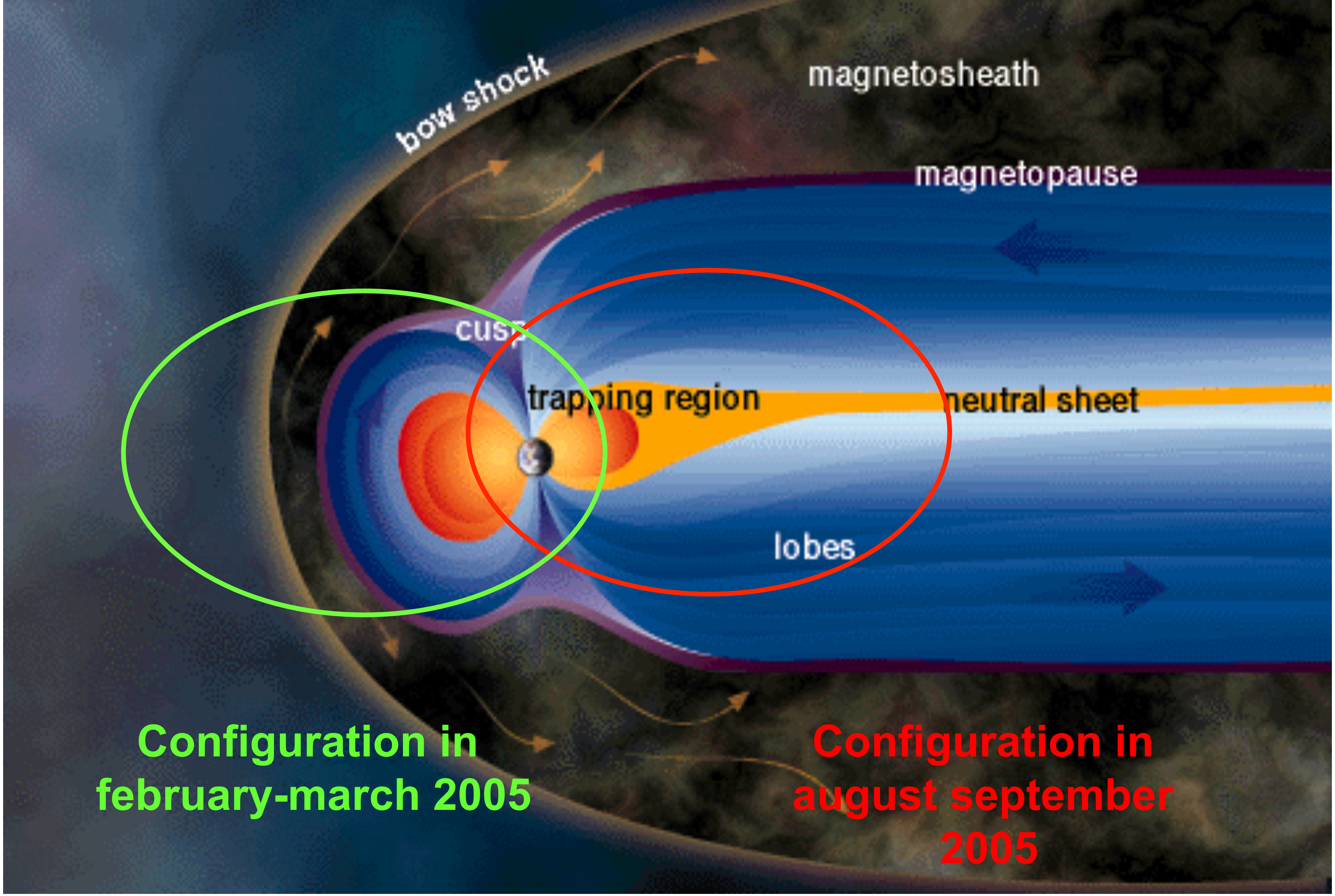

Magnetospheric regions visited by Cluster satellites

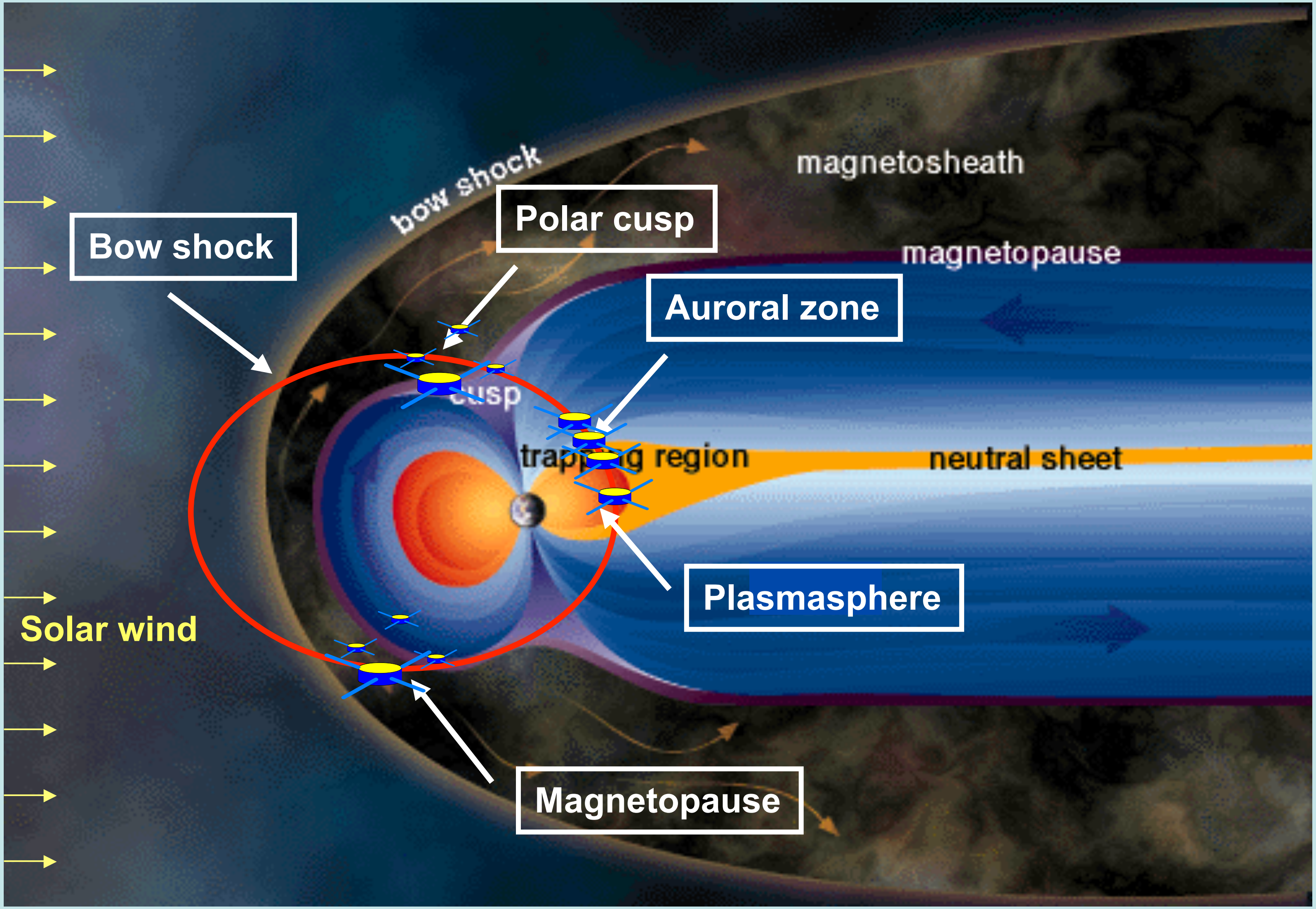

CLUSTER 2 : wave instruments

1 **STAFF** (N. Cornilleau-Wehrlin, F)
Magnetic and electric fluctuations
CNRS – CETP / **LPCE**/ LESIA

2 **EFW** (G. Gustafsson, S)
Electric fields and waves
KTH - Stockholm

3 **DWP** (H. Alleyne, UK)
Digital Wave Processor –
University of Sheffield

4 WHISPER (P. Décréau, F)
Electron density and plasma waves, CNRS – LPCE

5 **WBD** (D. Gurnett, USA)
Electric field wave-forms
University of Iowa

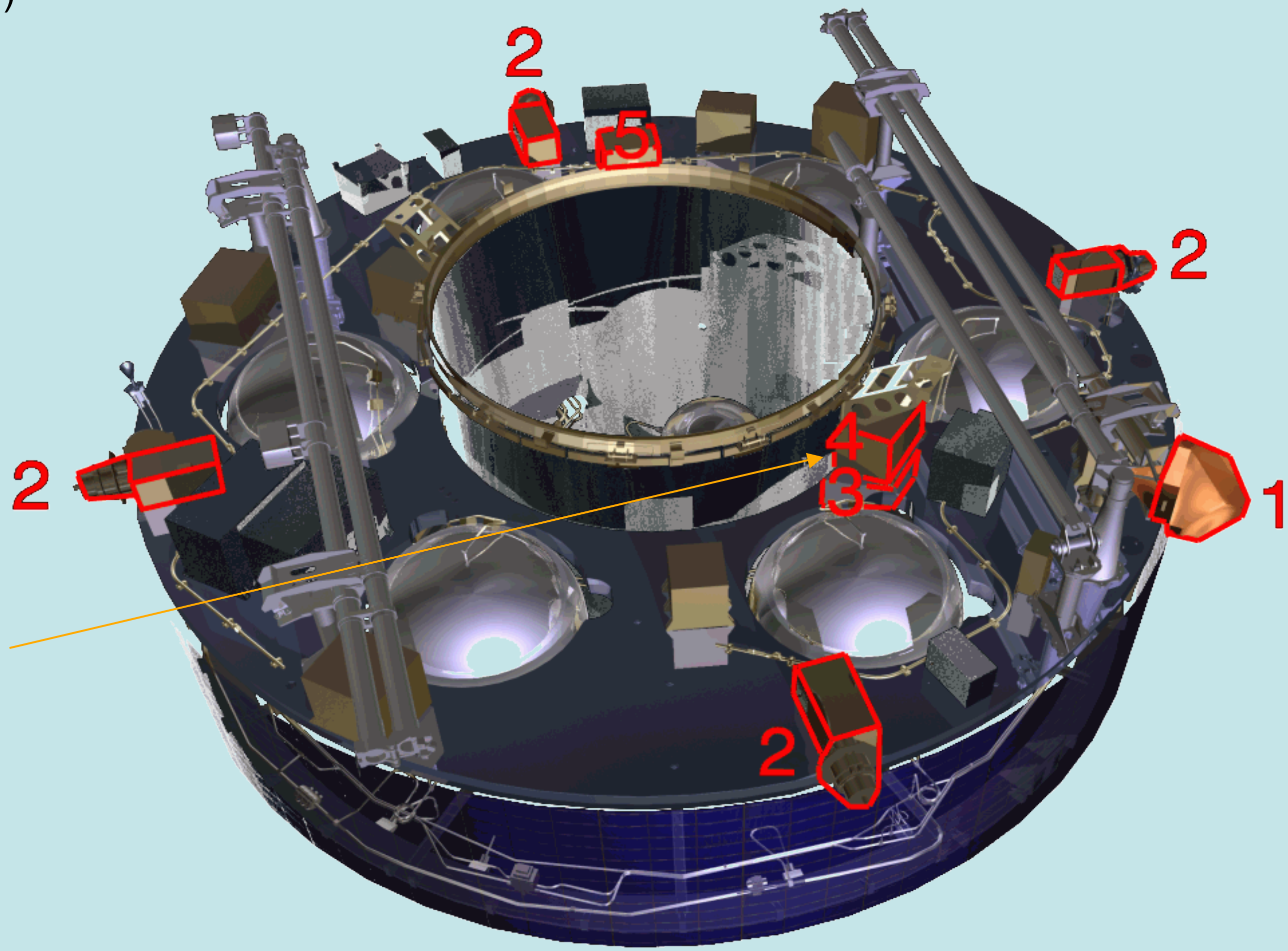

Direct and reflected chorus emission

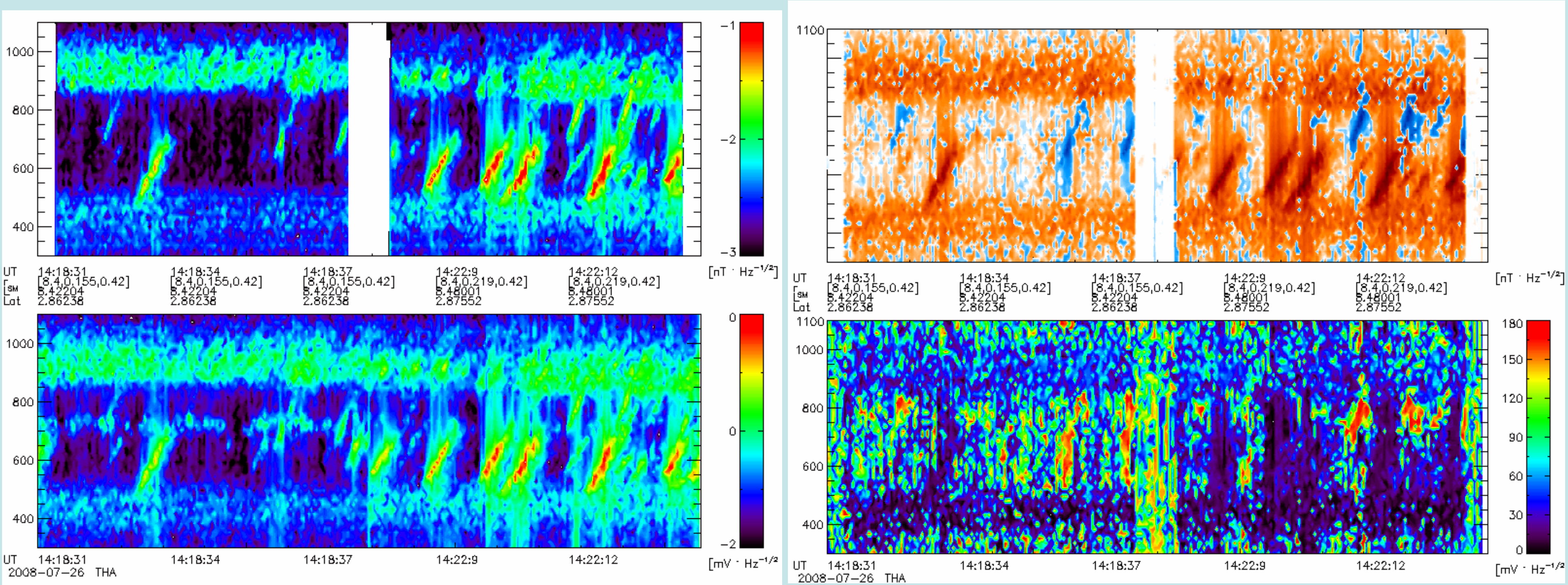

Detailed time-frequency power spectrograms of magnetic (top) and electric (bottom) field fluctuations near the source region recorded by the SCM and EFI instruments onboard the THEMIS spacecraft on July 28, 2008. b) and c) The direction of the Poynting flux is shown for chosen time intervals with direct and reflected chorus elements. The Poynting vector direction is shown (red – from the equator, blue – to the equator). The angle between the Poynting vector and background magnetic field vector (bottom).

Divergence of ray paths

$0.1\omega_{Be}$ to $0.6\omega_{Be}$.

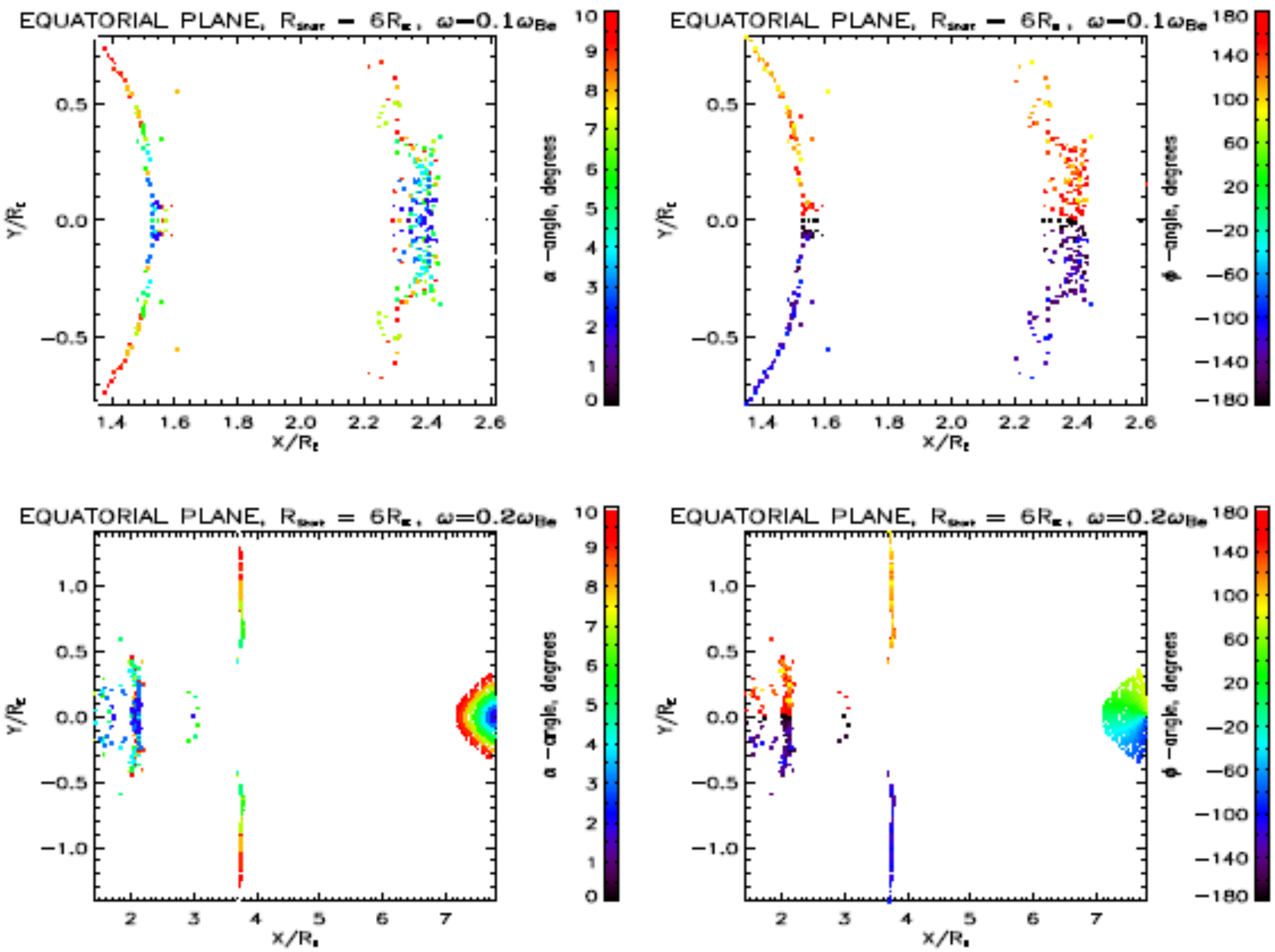

Estimates of characteristic perpendicular scales of sources and refractive index fluctuations (poster by Agapitov et al. for more details)

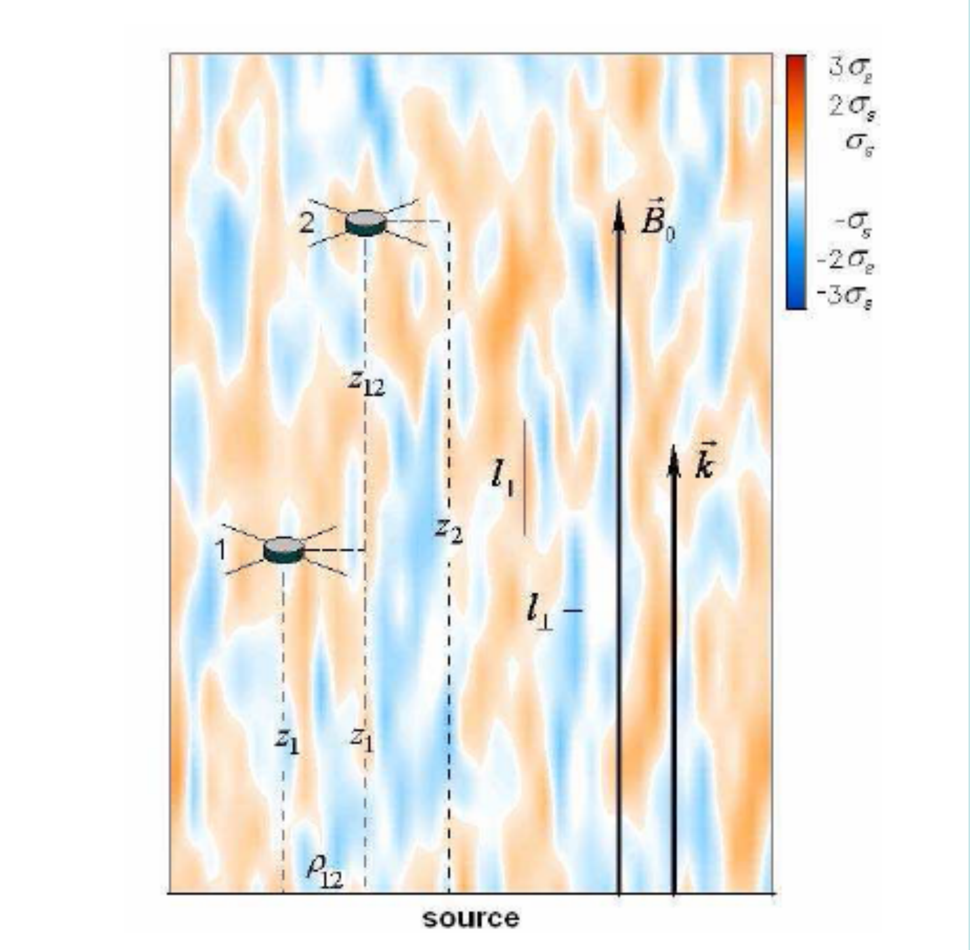

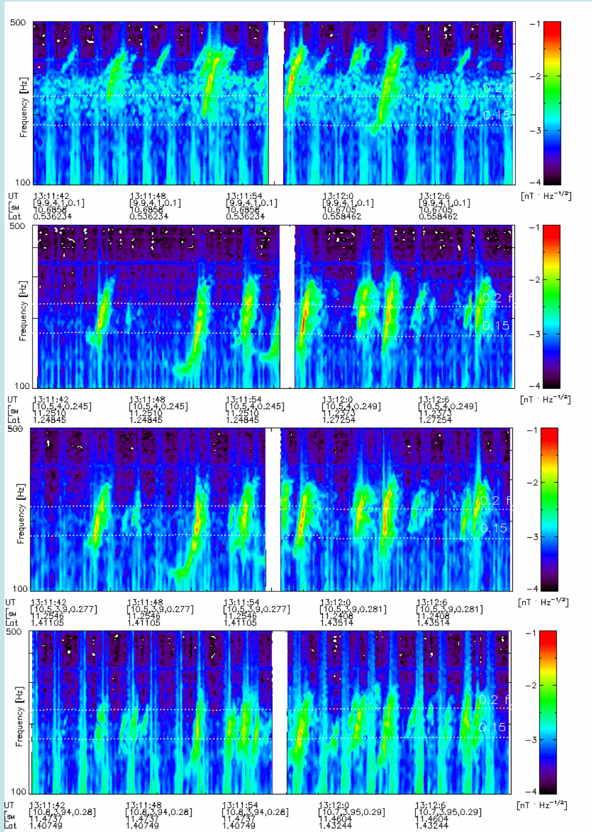

Time-frequency power spectrograms of magnetic and electric field fluctuations near the source region recorded by the search coil magnetometer (SCM**)** aboard the four THEMIS spacecraft on July 17, 2007. Panels show data from THB, THC, THD, and THE respectively (from Agapitov et al., 2010).

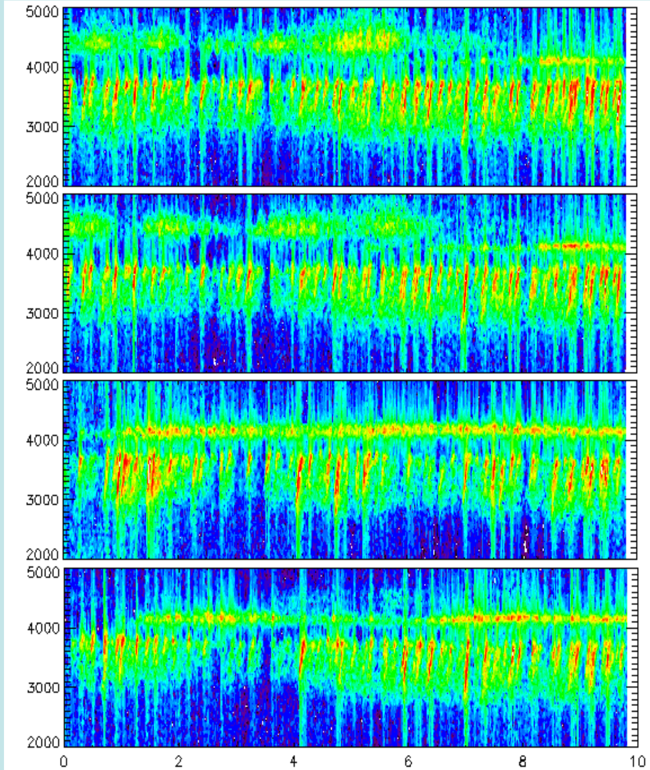

Time-frequency power spectrograms of electric field fluctuations captured by WBD instruments on board the four Cluster spacecraft on April 18, 2002. Panels from top to bottom show data from C1, C2, C3, and C4 respectively. The wave vector direction based on STAFF-SA spectral matrices data shows propagation along the background magnetic field (from Santolik and Gurnett, 2003 and Agapitov et al., 2011).

Chorus waves transverse coherence scales

Two spatial scales define the chorus waves transverse coherence scale:

(1) the transverse source scale in the vicinity of the generation region and

(2) the transverse scale of the plasma parameters fluctuations during the wave propagation. During the propagation signal detected aboard different spacecraft (in a case if the cross-spacecraft distance is larger than the fluctuation scale) has the similar amplitude structure but the phase coherence is lost

In [*Agapitov et al*., 2010, 2011] the technique which allows to distinguish the properties of the source and the wave propagation effects is proposed. The **source scale is found to be about 3000 km** and the **fluctuation scale is found to be about 300 km** (about ion Larmor radius) **in the outer magnetosphere (L>7).** The same estimation of the source scale was obtained in [*Nishimura et al.,* 2010, 2011] on the basis of the pulsating aurora region study. **In the inner magnetosphere** the source region scale is estimated to be about 60-150 km in [Santolik and Gurnett, 2003]. In [Agapitov et al., 2011] the **transversal fluctuation scale is found to be from 50 to 120 km** (about ion Larmor radius) and **estimation of the source scale gives the value about 600 km.**

Cross-correlation analysis of the phase and the averaged amplitude level

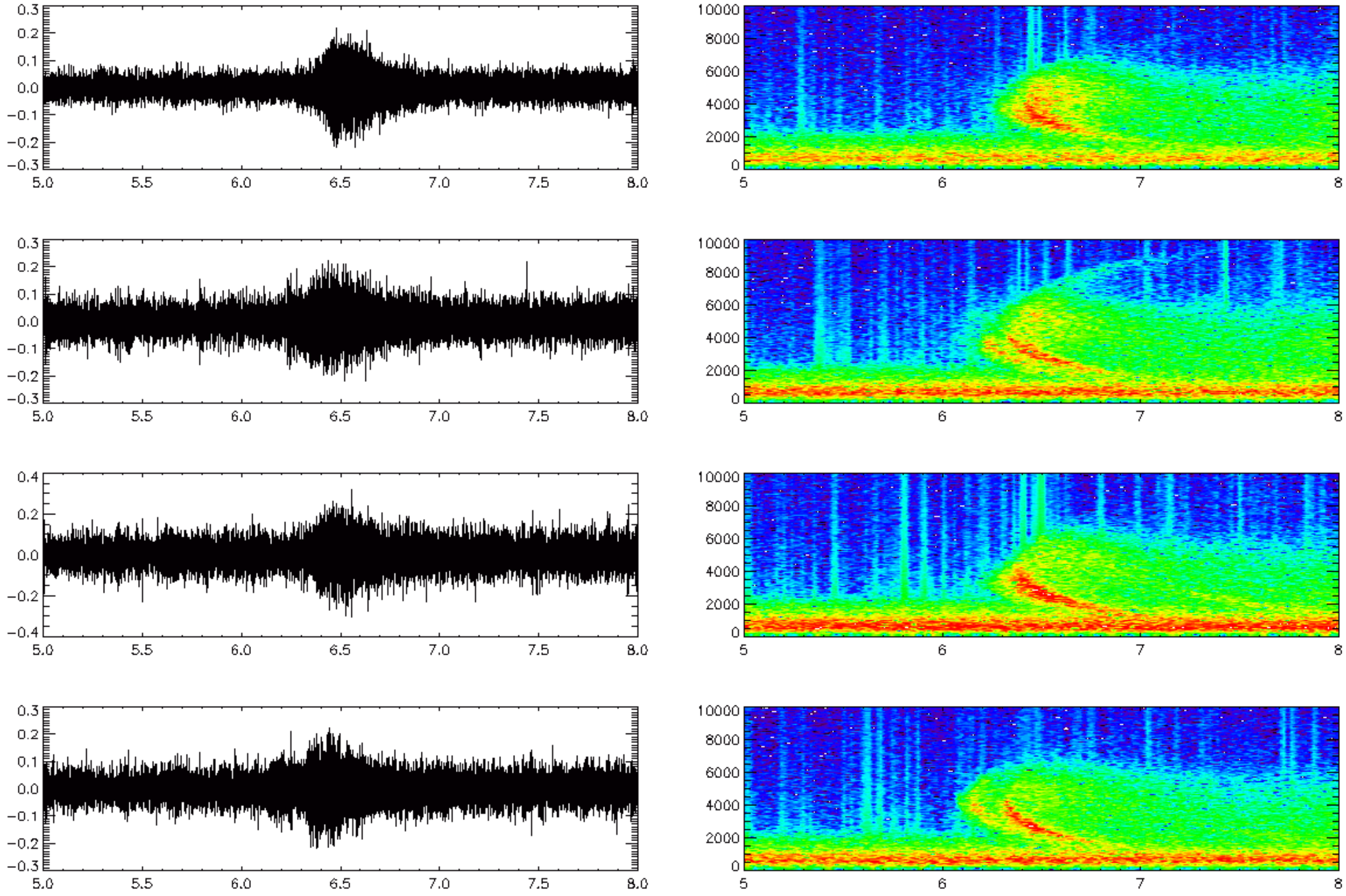

The waveform and dynamic spectrum of the WBD electric field measurements 2001-02-04 13:49:35 - 13:49:38. he The averaged amplitude level correlation analysis shows the common properties of the signal but the phase coherence is lost.

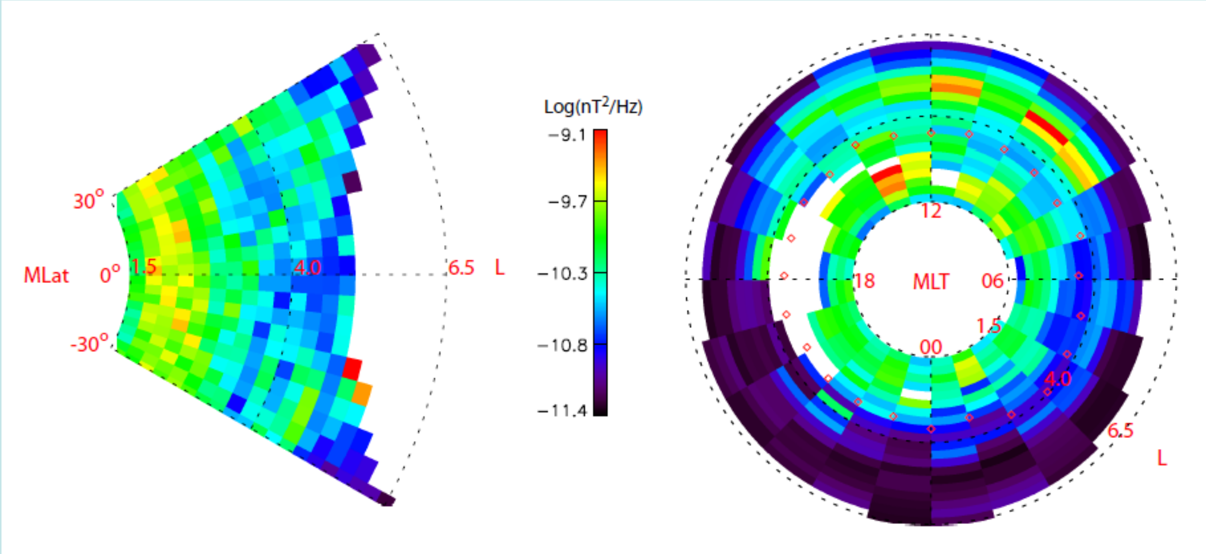

The averaged intensity of the low band chorus waves based on PWI data from the first DE-1 for the period from April 1981 to June 1984 (from *Pokhotelov*, 2006)

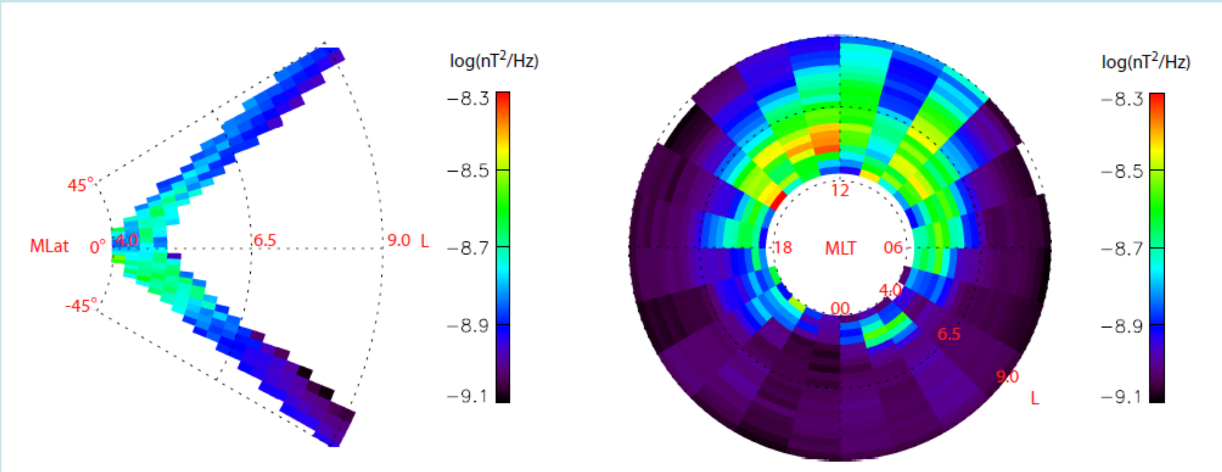

The averaged intensity of the low band chorus waves based on STAFF-SA data from the first Cluster spacecraft (Rumba) for the period from March 2001 to February 2005 [Pokhotelov et al., 2008]

Cluster coverage 2001-2009

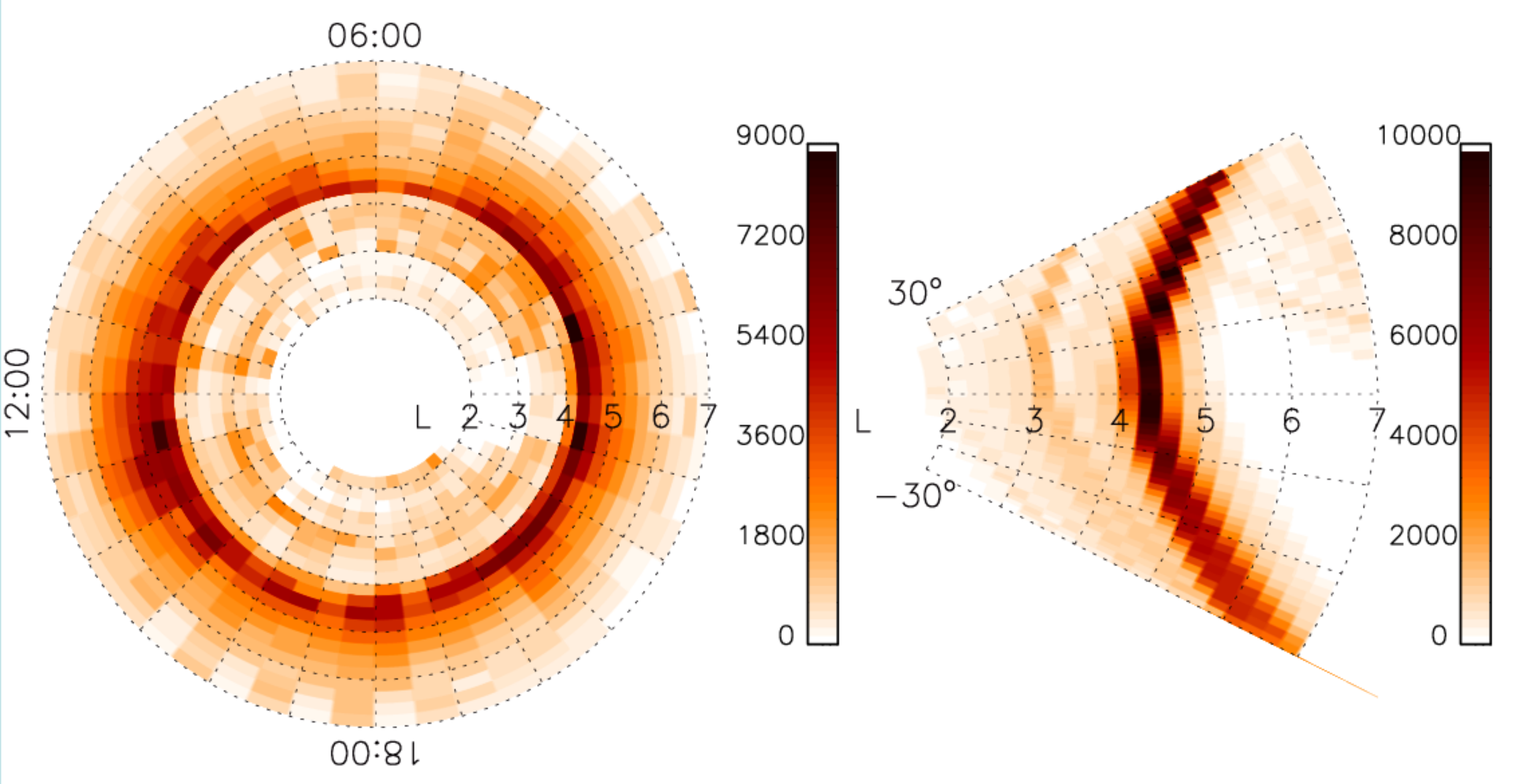

The distribution of the CLUSTER STAFF-SA spectral matrices measurements during 2001–2009 years

The distribution of the probability to detect the large amplitude chorus events during 2001–2009

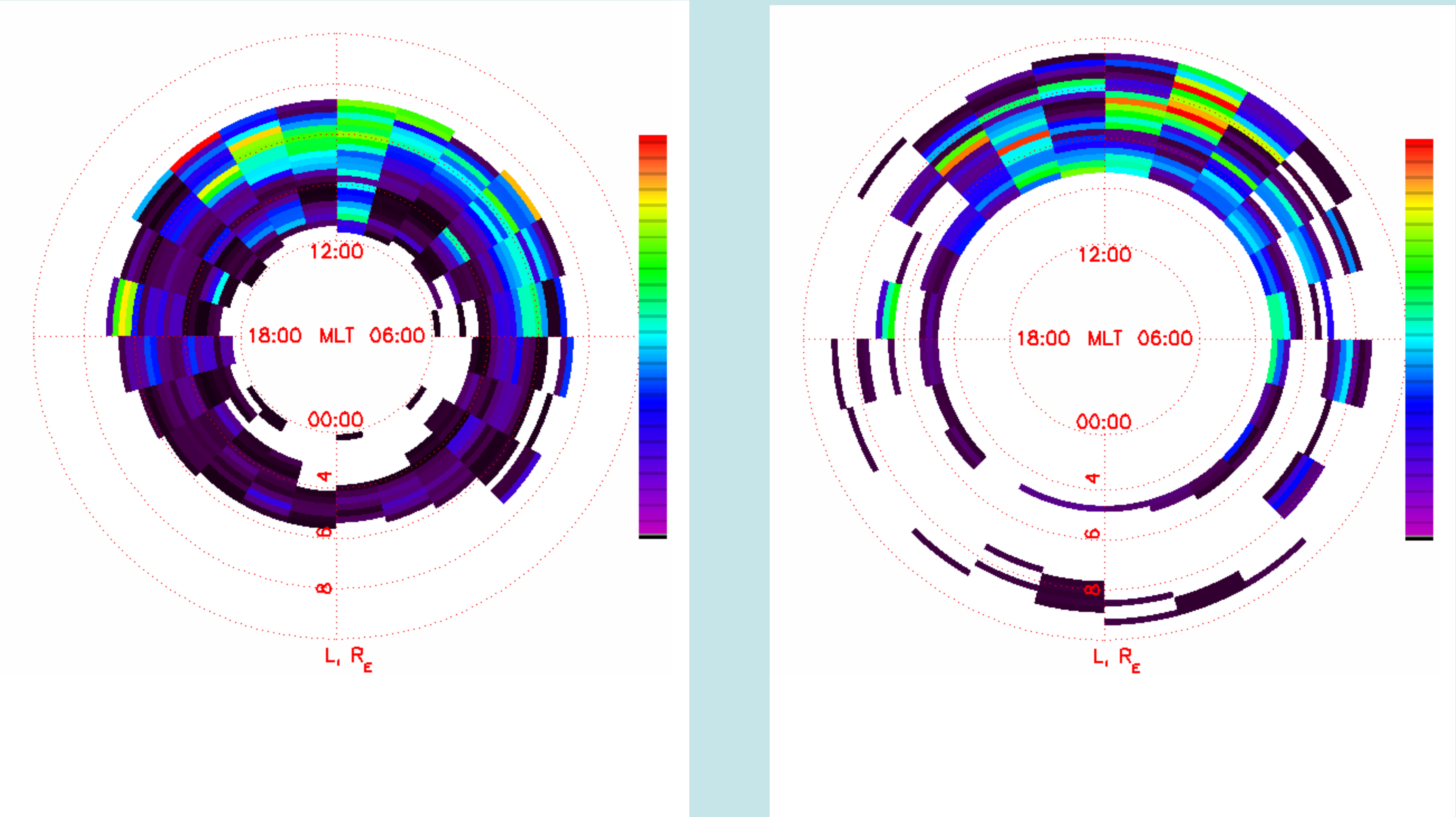

0.1 *fce*< *f* <0.5 *fce*   0.5 *fce*< *f* <1.0 *fce*

Cluster coverage: hiss frequency range

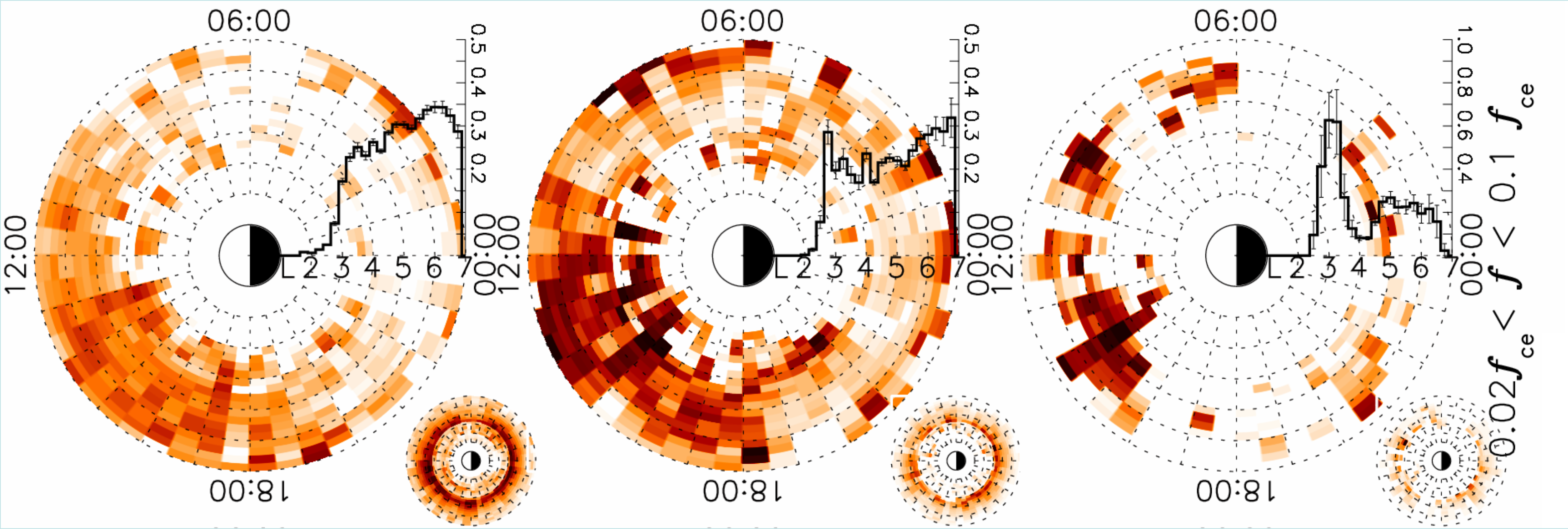

The distribution of the hiss waves with amplitudes of the magnetic field perturbations greater then 0.01 nT during the periods of low (K_p < 3), intermediate (3 < K_p < 5) and high geomagnetic activity (K_p > 5) -- lower panel. The distribution of the CLUSTER STAFF-SA spectral matrices measurements for each frequency and activity range is shown in small panel

Cluster coverage: chorus frequency range

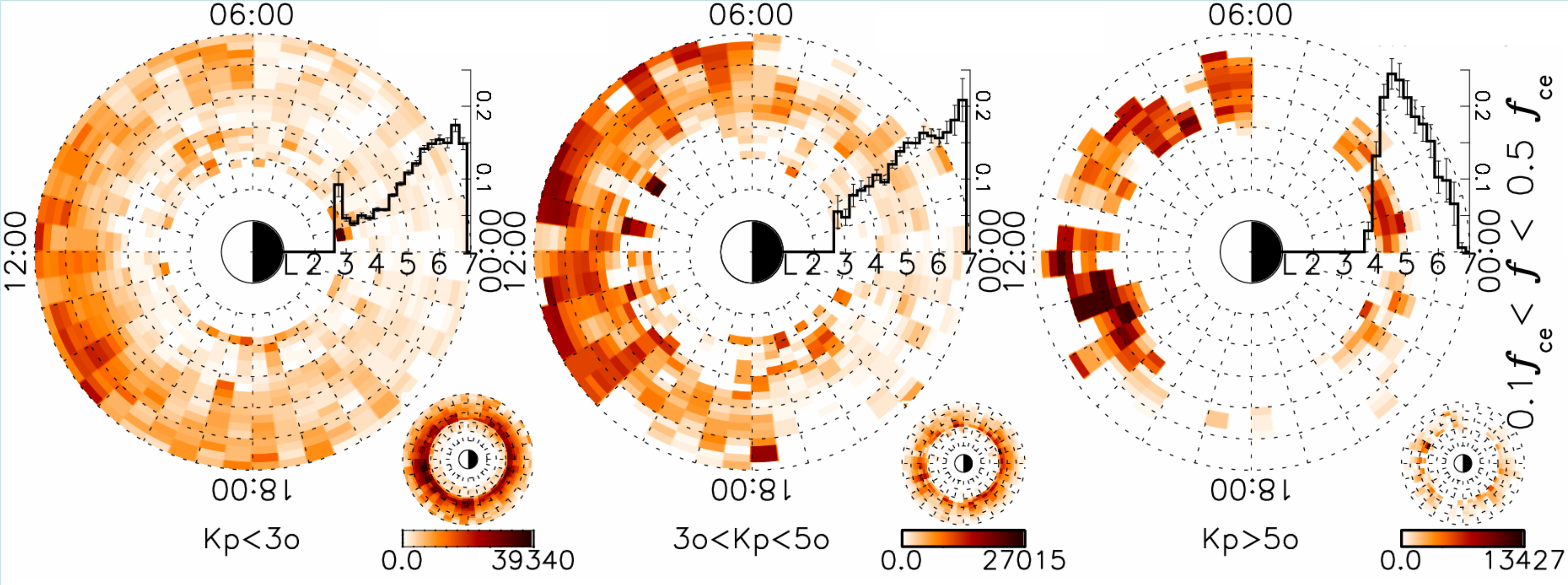

The distribution of the chorus waves with amplitude of the magnetic field perturbation greater then 0.01 nT during the periods of low (K_p < 3), intermediate (3 < K_p < 5) and high geomagnetic activity (K_p > 5) -- lower panel. The distribution of the CLUSTER STAFF-SA spectral matrices measurements for each frequency and activity range is shown in small panel

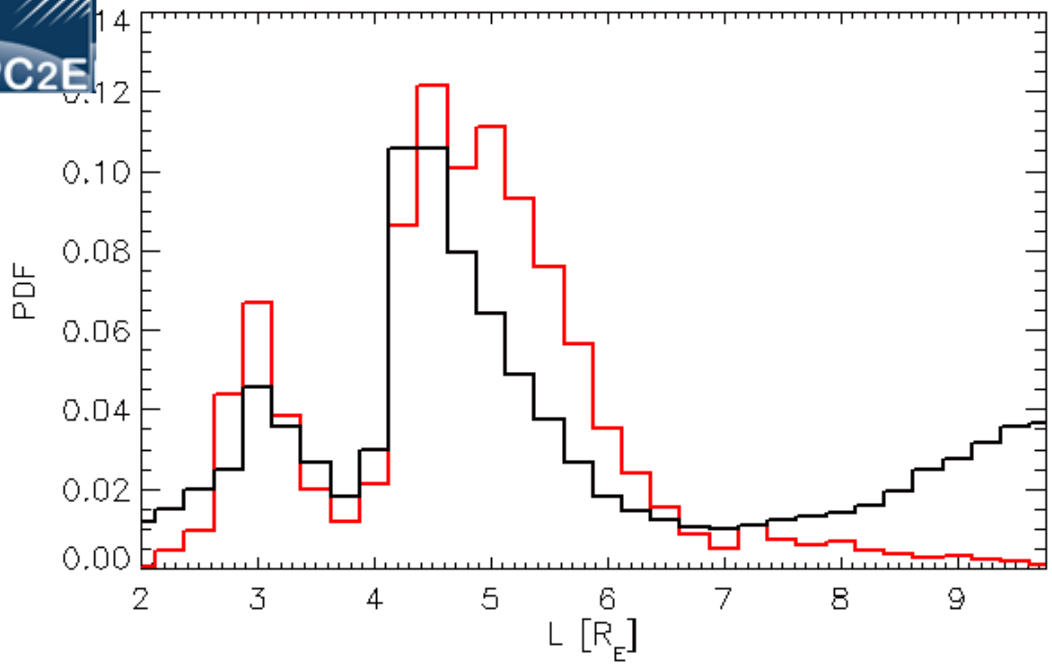

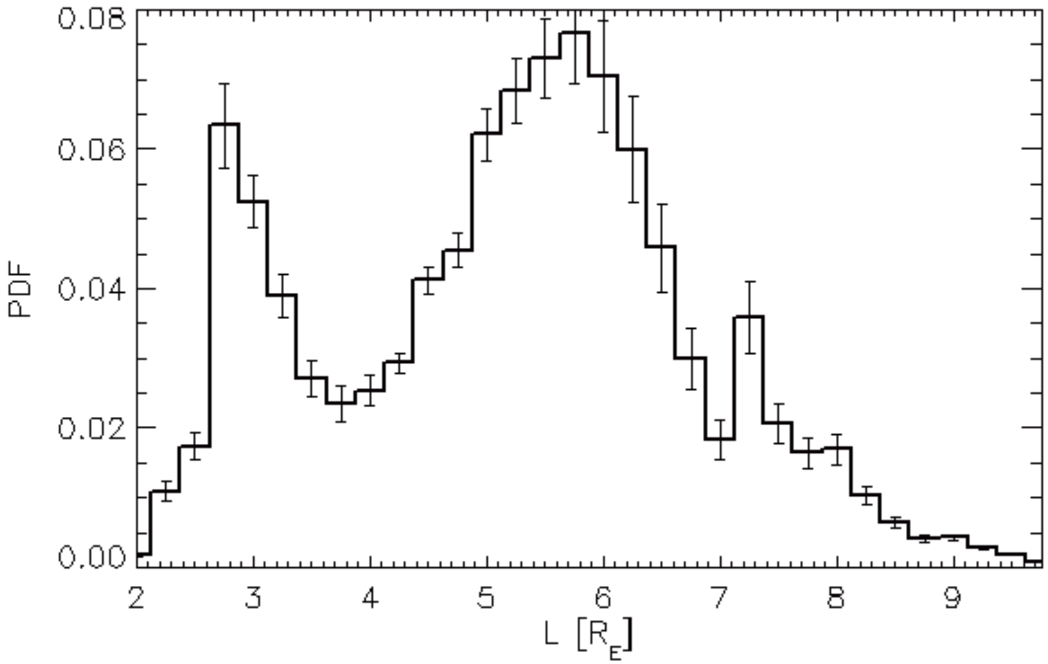

The Probability distribution function (PDF) of the spectral matrices (SM) measurements and PDF of large amplitude chorus emissions colored in red (dependence upon the L-shell)

The probability to detect large amplitude chorus emissions (dependence on the L-shell).

There are three different regions that show up clearly identifiable peaks L<3.5, 3.5 <L<7, L>7

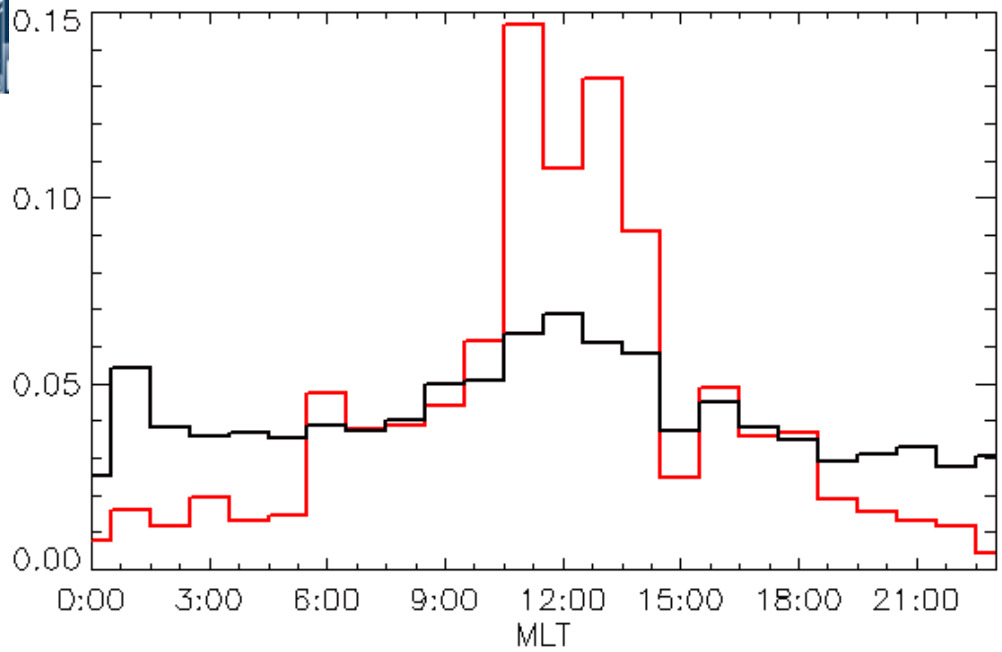

The PDF of the SM measurements and PDF of large amplitude chorus emissions (red color) (dependence on the MLT)

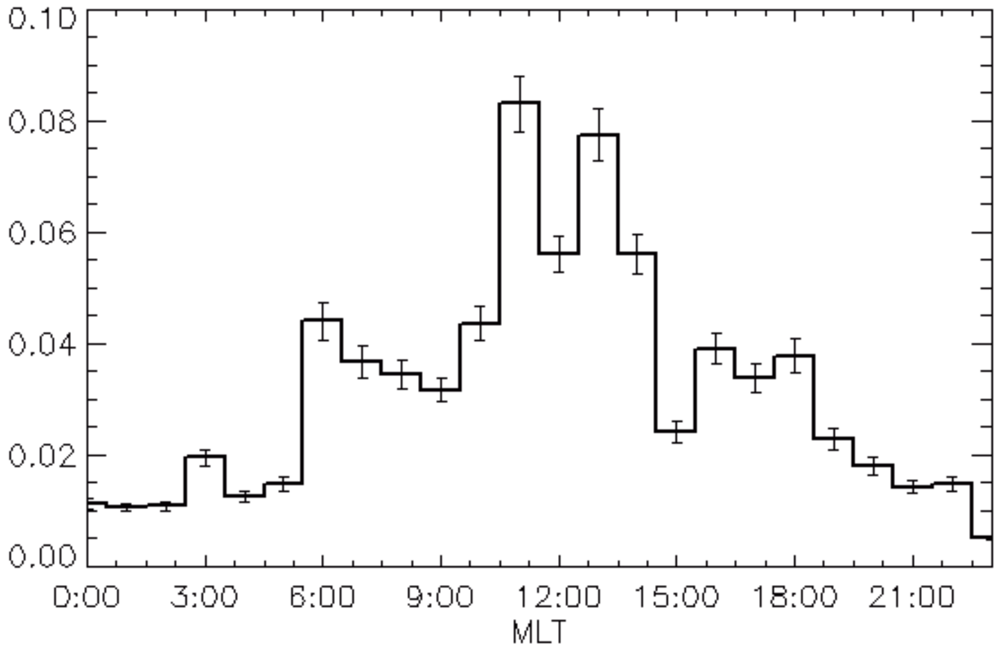

The probability to detect large amplitude chorus emission (dependence on the MLT)

K-vector determination

- **Technical issues:**
- **Two methods used**
- **1. Means method (Means, 1972)**
- **2. SVD (Santolik et al., 2003)**

K-vector determination

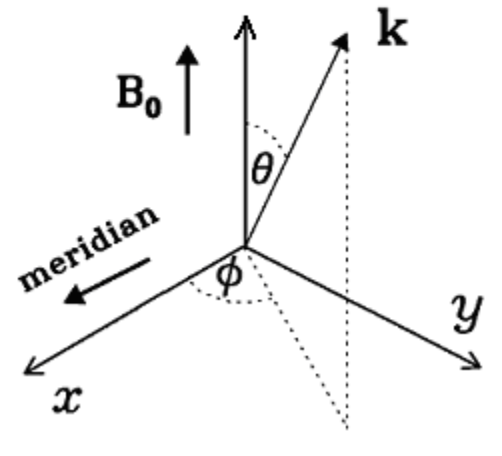

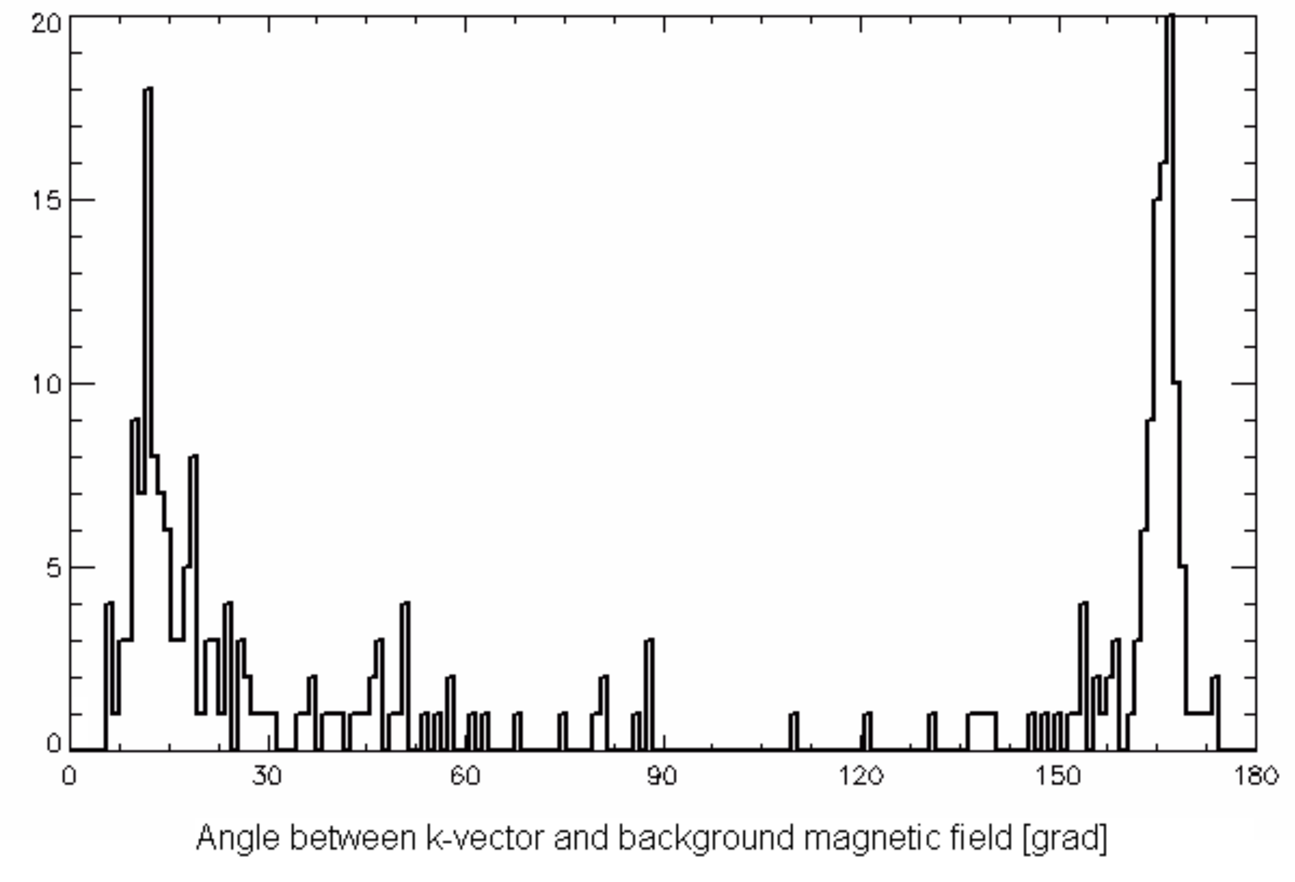

The histogram of the angle between the wave-vector and the magnetic field vector of the chorus waves during the magnetic equator crossing 8:45-9:15 18.04.2002.

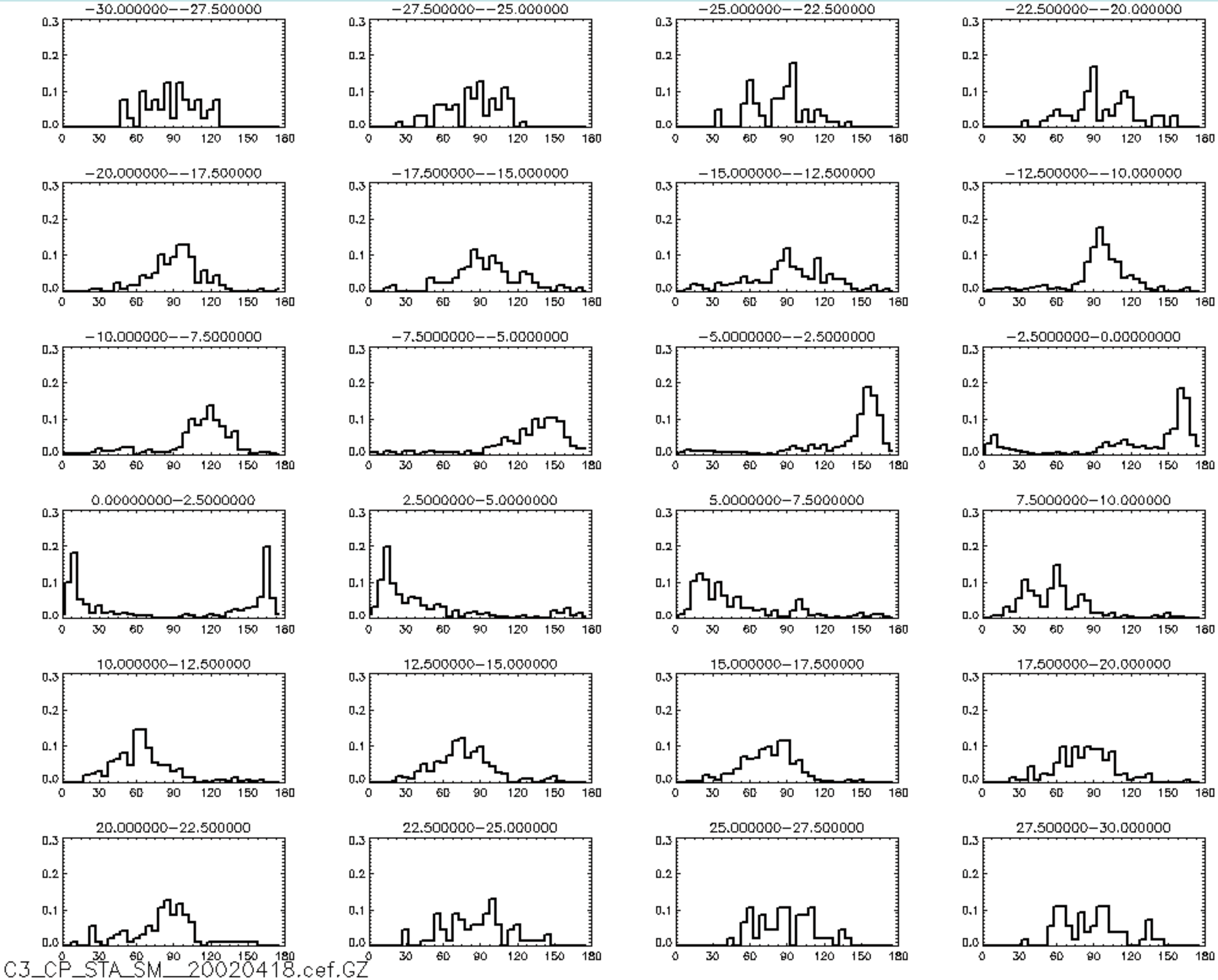

The histogram of the angle between the wave-vector and the magnetic field vector of the chorus waves during 18.04.2002.

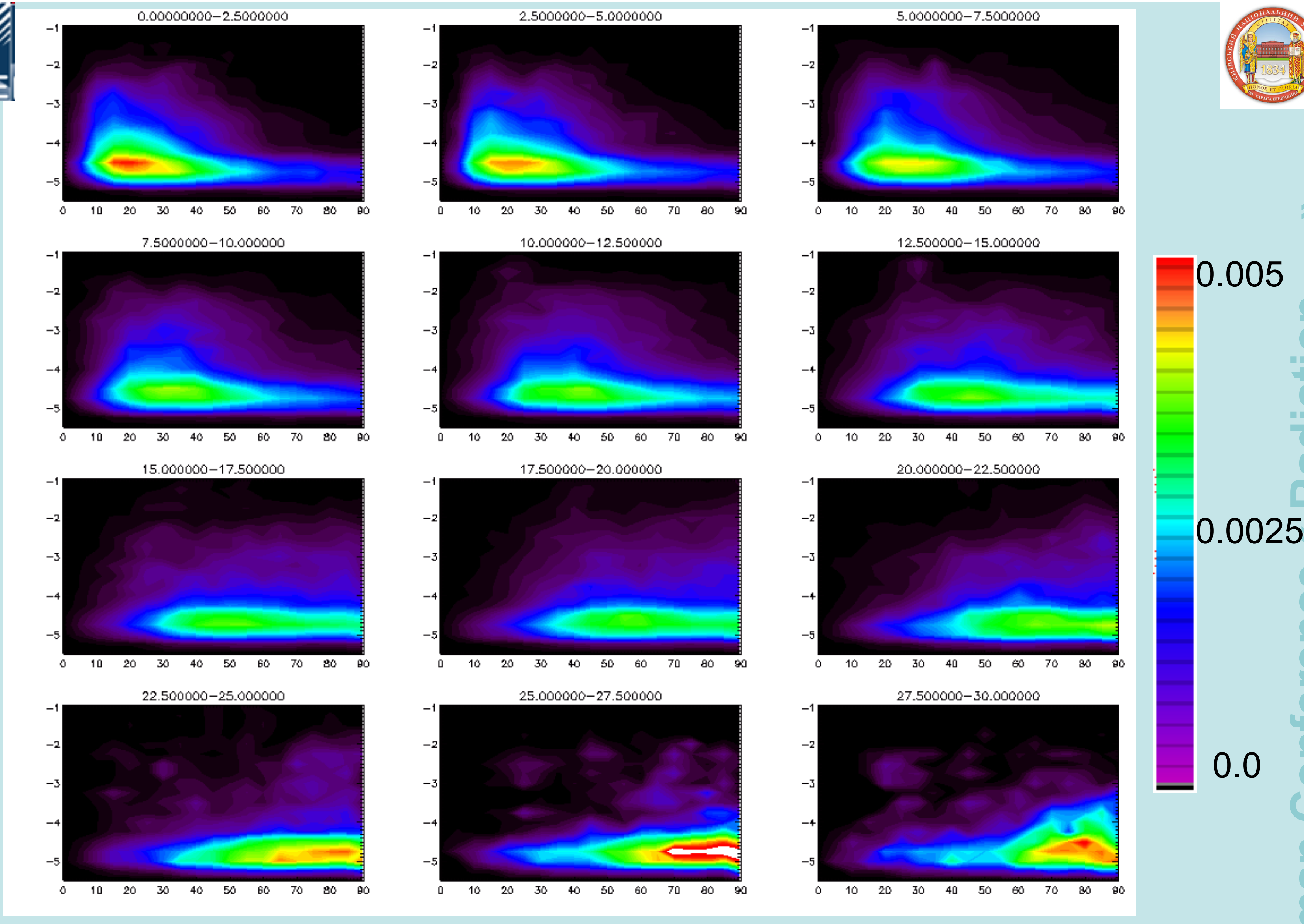

The histogram of distribution of angles between the wave-vector and the magnetic field vector of the chorus waves based on STAFF-SA CLUSTER measurements during 2001-2009 .

Statistics of angular distributions for low band and upper band chorus (the last is based on much smaller data set)

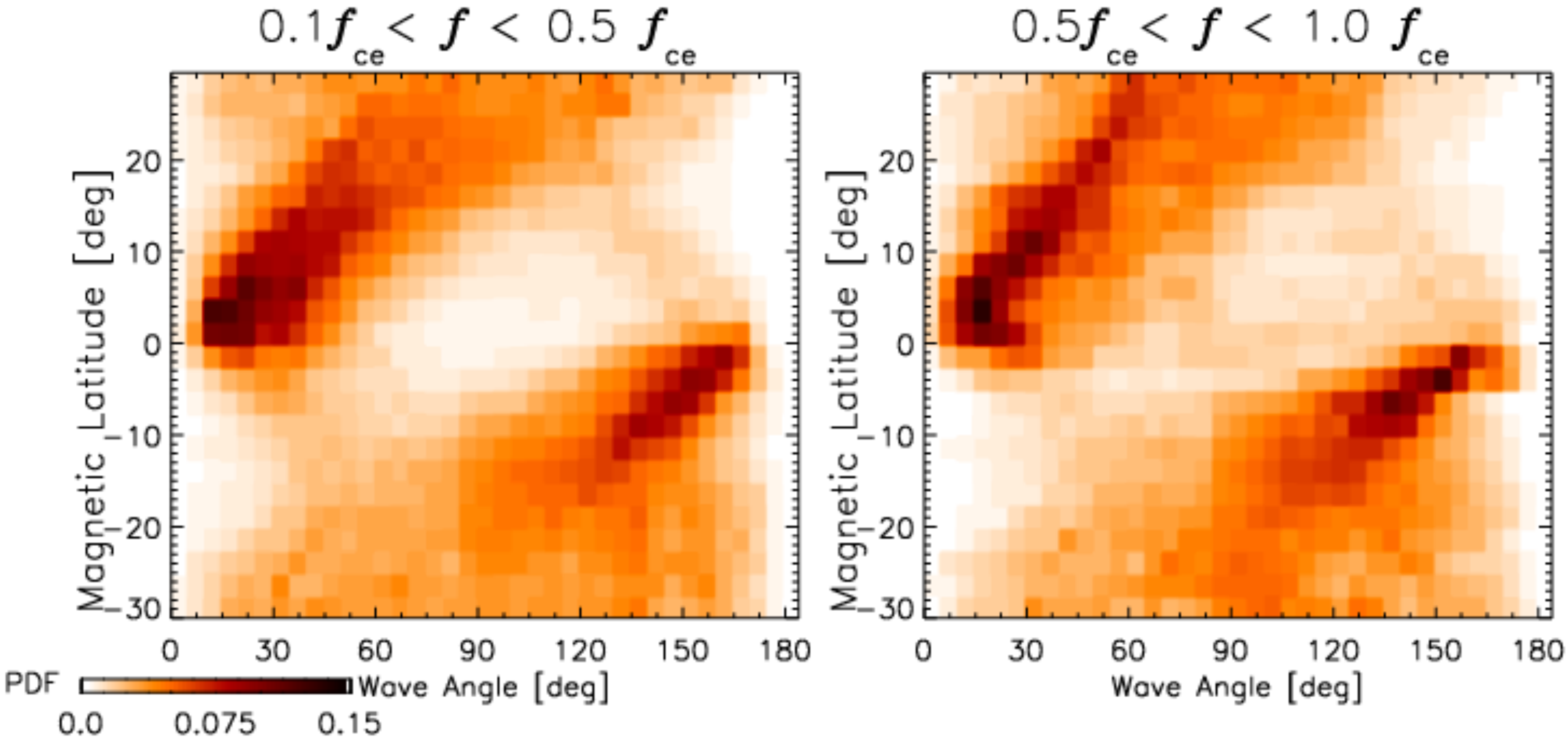

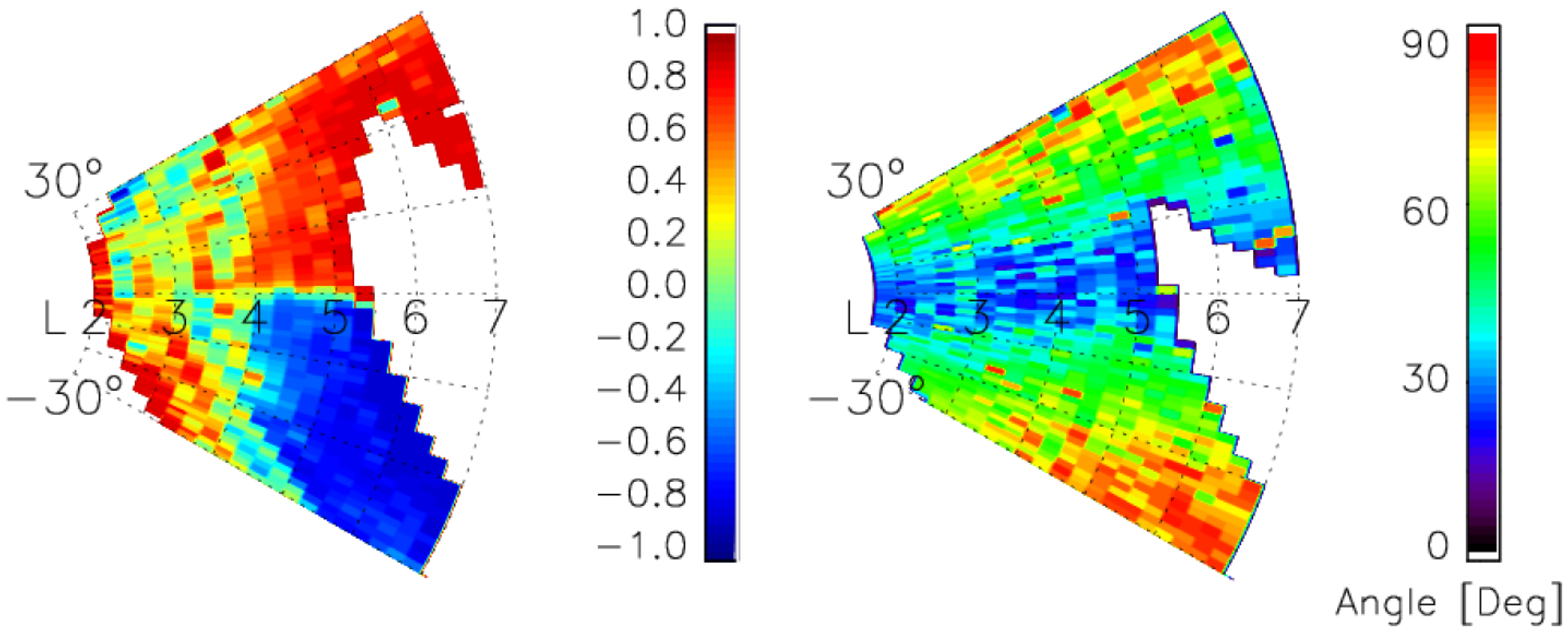

The dominant direction of the Poynting flux. It is characterized by the normalized parameter (N_a - N_o)/(N_a + N_o) , where N_a and N_o are the number of spectra having Poynting flux direction along and opposite to the background magnetic field respectively (left panel). The most probable value of the angle between wave-vector and the local magnetic field direction (right panel)

Conclusions

The statistical database of wave measurements aboard Cluster sc during 2001–2009 covers the regions of L-shells from 2 to 10, at different times and on different magnetic latitudes for quiet, moderate and active conditions in the magnetosphere. We performed an analysis of distribution of wave vectors in the frequency range from 8.8 Hz up to 3.56 kHz making use of the STAFF-SA instrument. The results can be summarized as follows:

The most intensive chorus waves are observed in the range from 23 to 13 hours MLT and at L-shells from 2 to 3 and from 4 to 6. Statistical characteristics of distributions are different for Kp < 5 and Kp > 5. There are two well distinguishable regions where statistical characteristics of wave amplitudes and normal vector distributions exhibit different dependences under low and moderate magnetic activity conditions

1) L = 2 – 4 (up to plasmapause) where lightning generated and magnetospheric chorus generated whistlers dominate;

2) the region where the chorus type whistlers dominate, L = 4-6.5.

Conclusions

- The magnetic latitudinal dependence of the wave normal vectors distribution clearly shows the increase of the maximum of the distribution from about 20° at equator up to 80° and even more at about 30° magnetic latitude. The probability distribution of wave activity parameters are usually non-symmetric and have significant non-Gaussian tails thus one can suggest that they can not be well-described by long-term time averages.

Ray tracing modelling

<u>Magnetic field model :</u>

is assumed to have an internal tilt (10°) dependent dipolar structure This empirical model (OGO) includes the contribution by only sources external to the Earth (magnetopause, tail and ring currents). Valid troughout inner magnetosphere (2 to 15 Re) and for quiet magnetic conditions. Any other model can be implemented. See Ref.[1] for details.

Density model

Based on the GCPM (2.2) which provides empirically derived core plasma density and ion composition (H+, He+, and O+) as a function of geomagnetic and solar conditions throughout the inner magnetosphere. The model is based on the data from DE/RIMS, DE/PWI, and ISEE/PWI and merges with the International Reference Ionosphere (IRI) at low altitudes. It is composed of separate models for the plasmasphere, plasmapause, trough, and polar cap. This model is described in detail in Ref.[2]

Density profile from GCPM 2.2

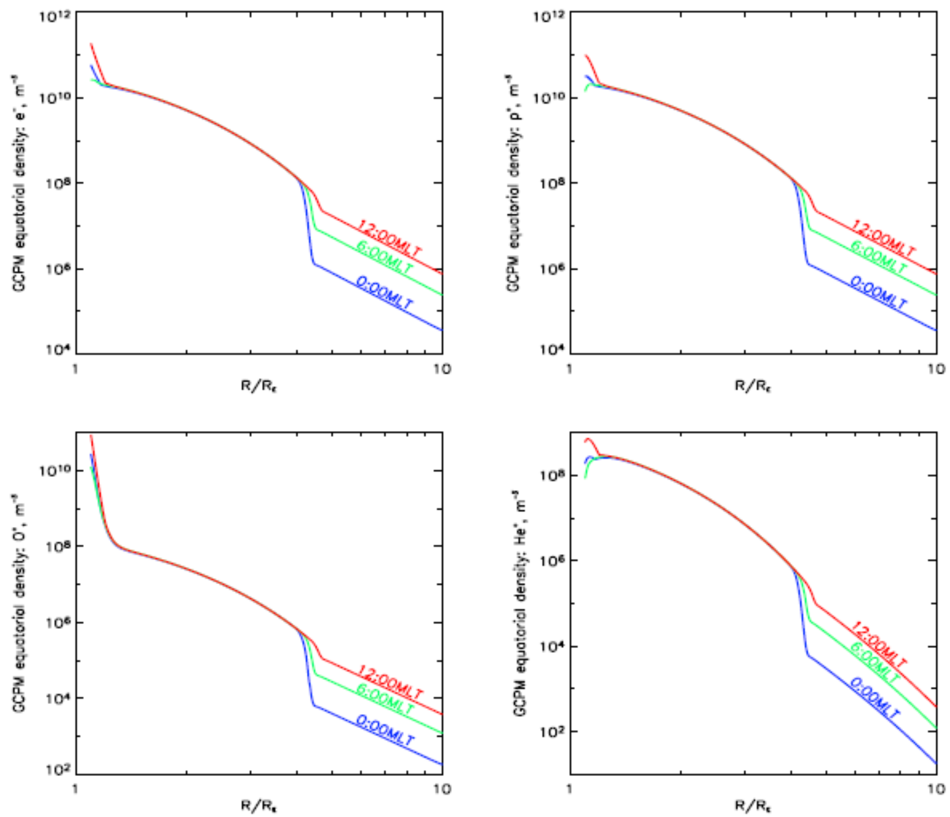

Figure 2: One-dimensional equatorial profiles of plasma species densities for different values of magnetic local time.

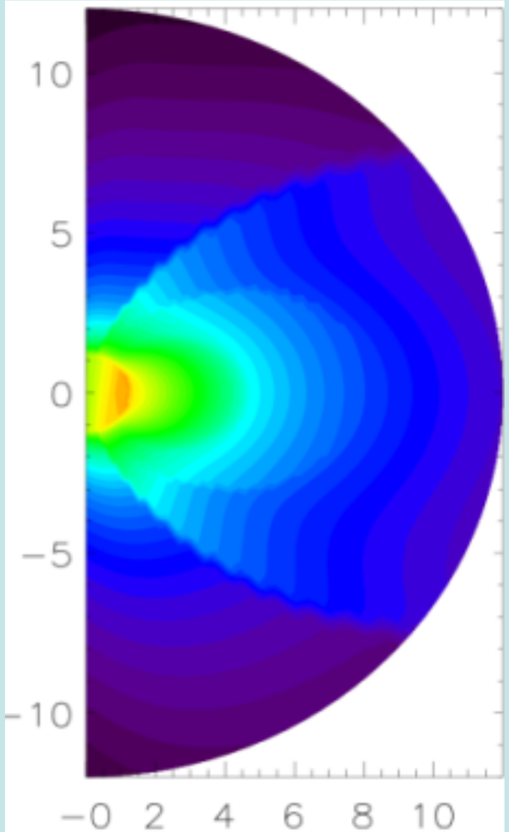

Sample 2D precomputed density slice (noon-midnight X-Z plane) used in the code, longitudinal variations are omitted. Distances are in Earth radii. Parameters are : Date=07SEP2002, Time= 00h30 UT, Kp= 4.0, MLT= 9.0

Ray tracing modelling

- <u>Initial K-vectors distribution :</u>
- Using improved version of WHAMP [3] program which calculates the hot plasma dispersion function in a magnetized plasma described by up to 6 maxwellian distribution functions, given previous density distributions. To make the plasma model completely resolved, characteristics of particle distribution functions are to be defined. We assume here that all plasma species obeys Maxwell's distributions with temperatures of 0.5 eV, which approximately corresponds to the Akebono data based temperature model.

Ray tracing modelling

Trajectory of the signal :
Having plasma and magnetic field parameters completely resolved in any point of modeled volume, one is able to define the wave dispersion function. And by using improved version of program Ratrace [4] (based on WHAMP code), which allow to « trace » the ray's path in the magnetosphere, one is able to calculate all the characteristics of this propagating whistler wave along its trajectory, namely, the points r of its trajectory, as well as the wavenumber k, complex frequency f and the amplitude A of the wave in all trajectory points.

Typical whistler trajectory

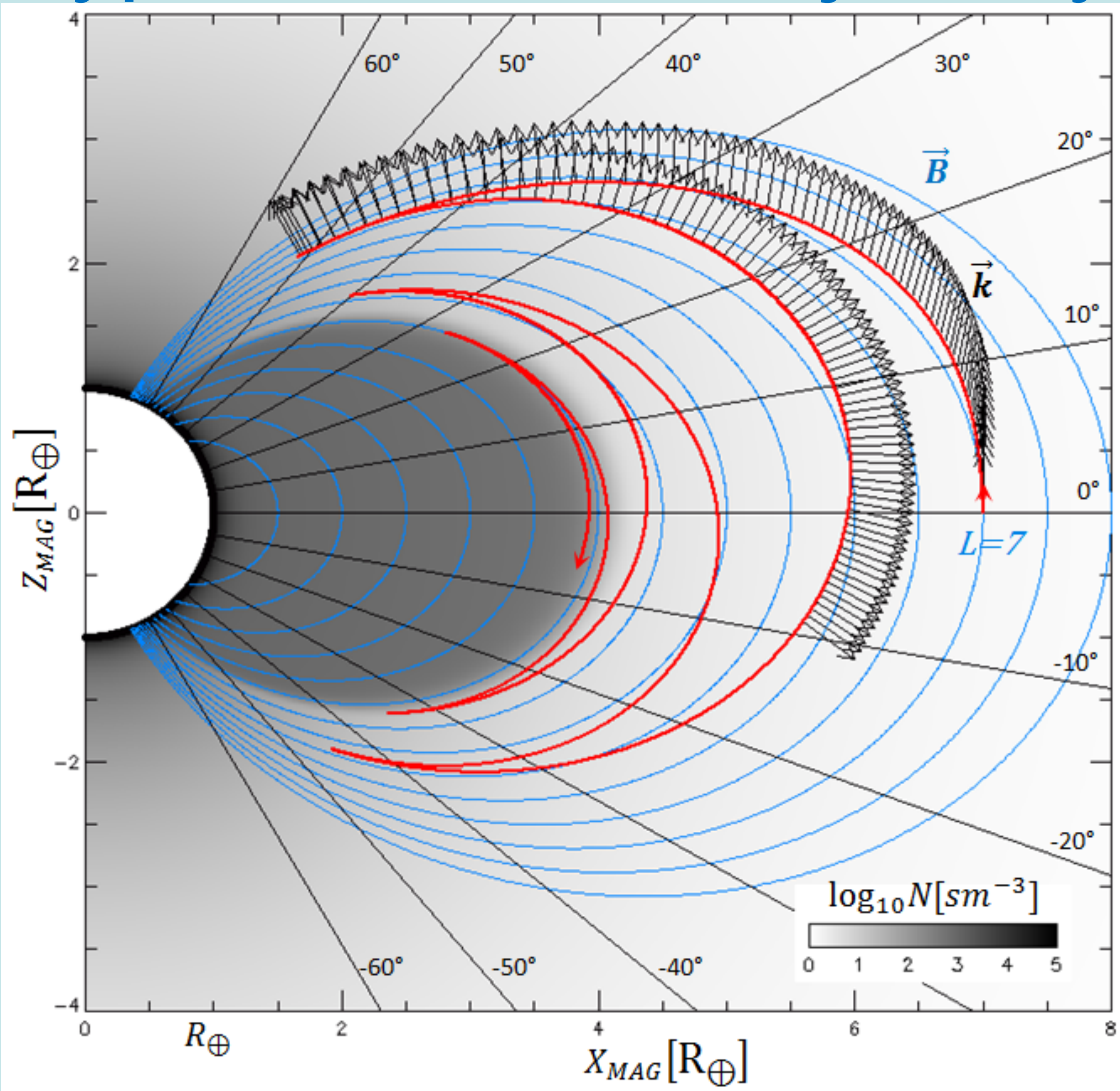

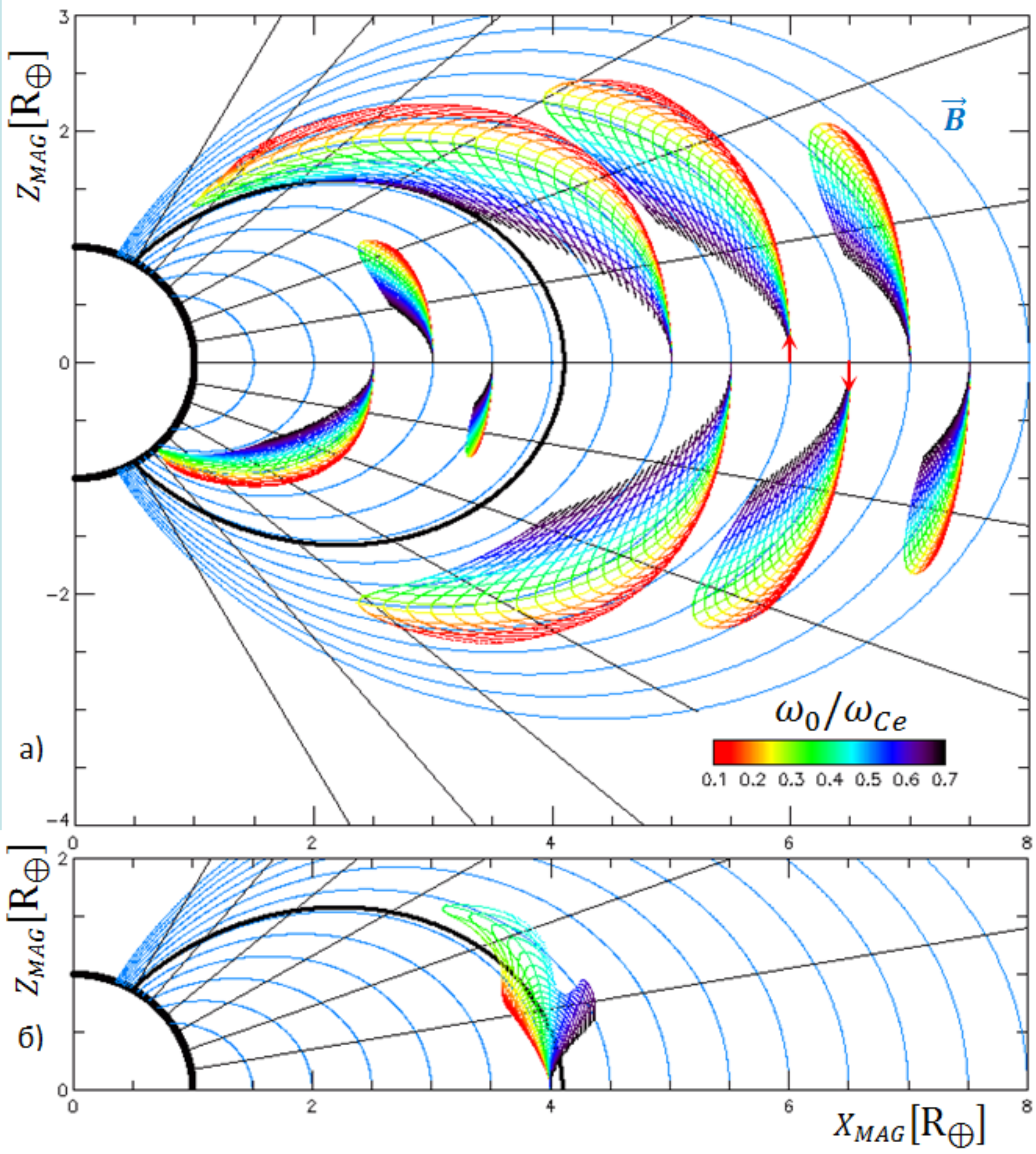

$\vec{B}$
ω_0/ω_{Ce}
0.1 0.2 0.3 0.4 0.5 0.6 0.7
а)
б)
$Z_{MAG}[R_\oplus]$
$X_{MAG}[R_\oplus]$

Observations versus simulations

PDF of the angle between the wave vector and the magnetic field vector for the set of magnetic latitudes. Red – Chorus waves with amplitude >0.01 nT. The energy fluxes originate mainly from the equator region.

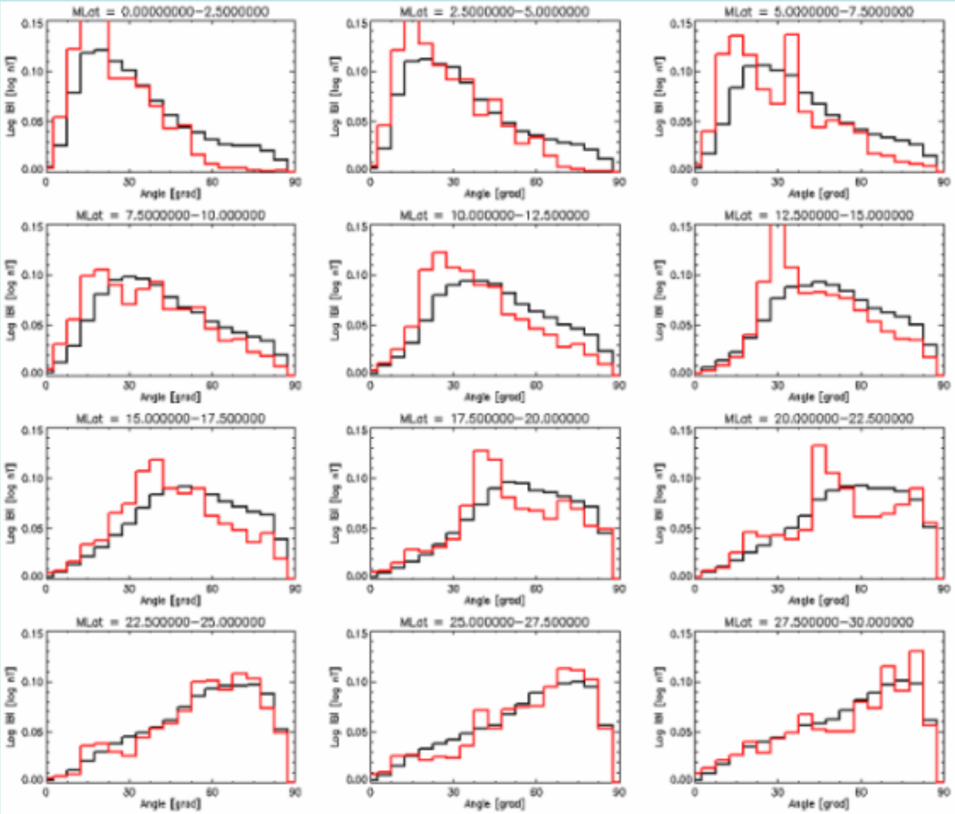

PDF of the angle (0-90°) between wave vector and background magnetic field vector for the set of magnetic latitudes with an initial distribution fitted to the experimental chorus wave dataset.

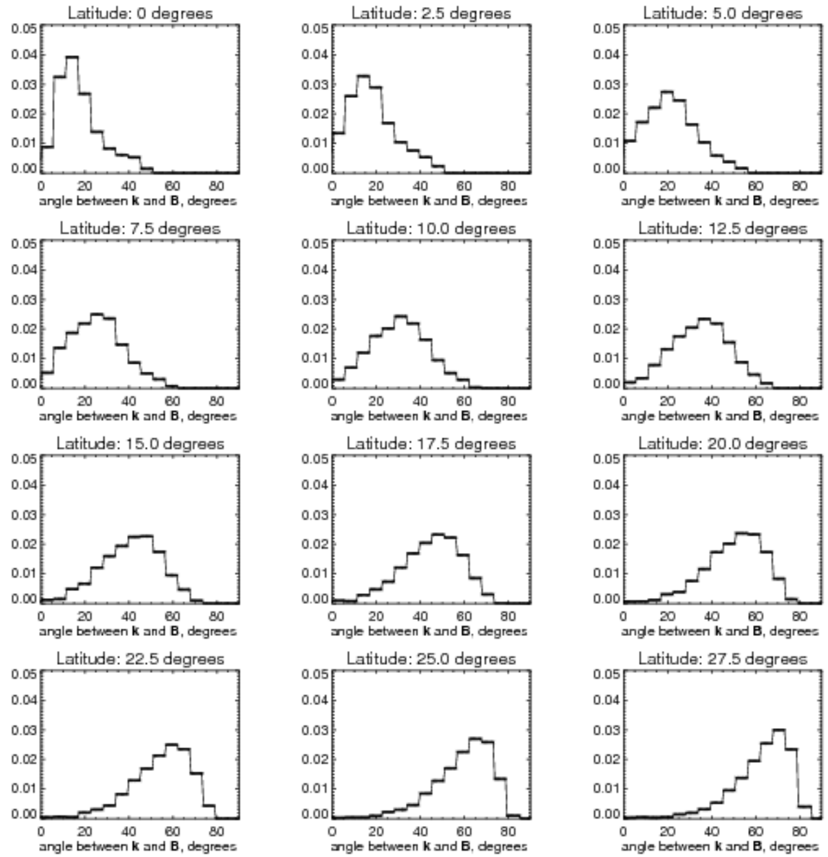

Conclusions

- The statistical properties of chorus wave vector distributions as modelled reproduce surprisingly well those observed.
- An important final remark:

- What is the impact of these effects on diffusion coefficients
- How to estimate the averaged diffusion coefficients including them in a simple but efficient way